

RECEIVED: May 12, 2023

ACCEPTED: July 26, 2023

PUBLISHED: August 9, 2023

Measurements of inclusive and differential cross sections for the Higgs boson production and decay to four-leptons in proton-proton collisions at $\sqrt{s} = 13 \text{ TeV}$



The CMS collaboration

E-mail: cms-publication-committee-chair@cern.ch

ABSTRACT: Measurements of the inclusive and differential fiducial cross sections for the Higgs boson production in the $H \rightarrow ZZ \rightarrow 4\ell$ ($\ell = e, \mu$) decay channel are presented. The results are obtained from the analysis of proton-proton collision data recorded by the CMS experiment at the CERN LHC at a center-of-mass energy of 13 TeV, corresponding to an integrated luminosity of 138 fb^{-1} . The measured inclusive fiducial cross section is $2.73 \pm 0.26 \text{ fb}$, in agreement with the standard model expectation of $2.86 \pm 0.1 \text{ fb}$. Differential cross sections are measured as a function of several kinematic observables sensitive to the Higgs boson production and decay to four leptons. A set of double-differential measurements is also performed, yielding a comprehensive characterization of the four leptons final state. Constraints on the Higgs boson trilinear coupling and on the bottom and charm quark coupling modifiers are derived from its transverse momentum distribution. All results are consistent with theoretical predictions from the standard model.

KEYWORDS: Hadron-Hadron Scattering, Higgs Physics

ARXIV EPRINT: [2305.07532](https://arxiv.org/abs/2305.07532)

Contents

1	Introduction	1
2	The CMS detector	3
3	Data and simulated samples	4
4	Event reconstruction and selection	6
5	Fiducial phase space definition	9
6	Observables	9
6.1	Matrix element discriminants	12
7	Background estimation	14
7.1	Irreducible backgrounds	14
7.2	Reducible background	15
8	Measurement methodology	16
9	Systematic uncertainties	18
10	Results	19
10.1	Inclusive cross section	21
10.2	Differential cross sections: production	21
10.3	Differential cross sections: decay	28
10.4	Double-differential cross sections	42
11	Interpretations	44
11.1	Constraints on the H boson self-coupling	44
11.2	Constraints on the charm and bottom quark couplings	46
12	Summary	47
The CMS collaboration		58

1 Introduction

The discovery of the Higgs (H) boson in 2012 by the ATLAS and CMS Collaborations [1–3] is a major confirmation of the correctness of the theoretical approach involving the electroweak (EW) symmetry breaking mechanism [4–9]. Subsequent measurements of the

properties of this particle [10–13], including its mass, quantum numbers, and couplings, further confirmed the consistency of these measurements with the standard model (SM) predictions.

The H boson decay into four charged leptons ($H \rightarrow ZZ \rightarrow 4\ell$, $\ell = e, \mu$), with its fully reconstructible final state and large signal-to-background ratio, has been one of the pillars for the characterization of this particle since its discovery. Several properties of the H boson were measured in this decay channel at the CERN LHC, based on the Run 1 data set at center-of-mass energies of 7 and 8 TeV and on the Run 2 data set at 13 TeV. These include the determination of its mass, spin and parity [14–19], width [20–23], inclusive and differential fiducial cross sections [18, 24–28], and tensor structure for interactions with a pair of gauge bosons [17, 19, 21, 29–31]. The most precise value of the H boson mass to date, measured by the CMS Collaboration, is $m_H = 125.38 \pm 0.14$ GeV, obtained from the combination of the $H \rightarrow ZZ \rightarrow 4\ell$ and $H \rightarrow \gamma\gamma$ decay channels from the analysis of the Run 1 and 2016 Run 2 data sets [32]. From the analysis of the full Run 2 data set, the CMS Collaboration reported the first evidence for the off-shell H boson production in events with a final state of two Z bosons decaying into either four charged leptons, or two charged leptons and two neutrinos, with a measured value of the H boson width of $\Gamma_H = 3.2^{+2.4}_{-1.7}$ MeV [33].

The H boson production is often experimentally characterized via the so called simplified template cross section (STXS) framework, which defines mutually exclusive phase space regions designed to maximize the experimental sensitivity to physics beyond the SM (BSM) effects and reduce, at the same time, the theoretical model dependence in the measurements [34]. The ATLAS and CMS Collaborations published results of cross section measurements in the STXS framework using the full Run 2 data set in the $H \rightarrow ZZ \rightarrow 4\ell$ [27, 35] and other decay channels [36–42]. The ATLAS and CMS Collaborations recently published results obtained from the combination of all the decay channels focusing on measurements of simplified template cross sections (STXS) [43] and H boson couplings [44], respectively.

Fiducial cross section measurements constitute a complementary approach for the characterization of the H boson production and decay that provide a set of less model-dependent results by unfolding detector effects from the data, thus allowing a direct comparison with state-of-the-art theoretical predictions. The ATLAS and CMS Collaborations published fiducial cross section measurements in the $H \rightarrow \gamma\gamma$ [45, 46], $H \rightarrow WW$ [47–49], and $H \rightarrow ZZ \rightarrow 4\ell$ [28, 35] decay channels using the full Run 2 data set. The CMS Collaboration also published results in the $H \rightarrow \tau\tau$ [50] decay channel, while the ATLAS Collaboration presented results from the combination of the $H \rightarrow \gamma\gamma$ and $H \rightarrow ZZ \rightarrow 4\ell$ decay channels [51].

This paper presents measurements of inclusive and differential cross sections for the H boson production in the $H \rightarrow ZZ \rightarrow 4\ell$ decay channel using data from proton-proton (pp) collisions recorded with the CMS detector at the LHC in 2016–2018 and corresponding to an integrated luminosity of 138 fb^{-1} . To reduce the model dependence, all the measurements are performed within a fiducial phase space region defined to closely reproduce the experimental acceptance and reconstruction-level selection criteria.

Differential cross sections are measured for several kinematic observables sensitive to the H boson production and its decay into four leptons, providing a complete characterization of this channel and coverage of the entire fiducial phase space. This includes

the measurement of six double-differential cross sections. Fiducial cross sections are also measured in bins of matrix element kinematic discriminants sensitive to possible anomalous couplings of the H boson to vector bosons. This provides a valuable test of the SM predictions and may reveal possible BSM physics.

The analysis builds upon the methods used in previous measurements of H boson properties in the four-lepton decay channel [25, 35], featuring the latest CMS Run 2 calibrations and a reduction by $\sim 40\%$ for the leading systematic uncertainty in lepton reconstruction and selection efficiencies.

The measurement of the fiducial cross section in bins of transverse momentum p_T of the H boson (p_T^H) is also used to set constraints on the H boson trilinear self-coupling and on the coupling modifiers of the H boson to b and c quarks. The CMS Collaboration recently reported constraints on the H boson self-coupling from the combination of several decay channels using the full Run 2 data set [44]. These constraints are obtained from the interpretation of the STXS results, while in this paper an alternative and complementary approach using differential cross section measurements is explored. The ATLAS Collaboration set limits on the coupling modifiers of the H to b and c quarks from the combination of the $H \rightarrow ZZ \rightarrow 4\ell$ and $H \rightarrow \gamma\gamma$ decay channels using the 2016–2018 Run 2 data set [51]. The CMS Collaboration reported similar results using the 2016 Run 2 data set and combining the $H \rightarrow ZZ \rightarrow 4\ell$ and $H \rightarrow \gamma\gamma$ decay channels [52]. The constraints derived from the analysis presented in this paper supersede the ones reported for the $H \rightarrow ZZ \rightarrow 4\ell$ channel in ref. [52].

This paper is organized as follows. The CMS detector is briefly described in section 2. The data set used is presented in section 3, along with a description of the simulated signal and background samples. The event reconstruction techniques and the selection criteria used to identify H boson candidates are outlined in section 4. The definition of the restricted phase space region where the differential cross sections are measured is given in section 5. A complete description of all the kinematic observables, with a particular emphasis on matrix element discriminants, is presented in section 6. The background modeling is presented in section 7. The signal modeling and the statistical procedure adopted in the extraction of the inclusive and differential cross sections are presented in section 8. The systematic uncertainties that affect the measurement are described in section 9. The results of the analysis and their comparison to the SM expectations are outlined in section 10. In section 11 the measurement of the fiducial cross section in differential bins of p_T^H are used to set constraints to the trilinear self-coupling of the H boson and to its couplings with charm and bottom quarks. A summary highlighting the main findings of the analysis is given in section 12.

2 The CMS detector

The central feature of the CMS apparatus is a superconducting solenoid of 6 m internal diameter, providing a magnetic field of 3.8 T. Within the solenoid volume are a silicon pixel and strip tracker, a lead tungstate crystal electromagnetic calorimeter (ECAL), and a brass and scintillator hadron calorimeter (HCAL), each composed of a barrel and two endcap sections. Forward calorimeters extend the pseudorapidity (η) coverage provided by

the barrel and endcap detectors. Muons are detected in gas-ionization chambers embedded in the steel flux-return yoke outside the solenoid. The electromagnetic calorimeter consists of 75 848 lead tungstate crystals, which provide coverage in pseudorapidity $|\eta| < 1.48$ in a barrel region (EB) and $1.48 < |\eta| < 3.0$ in two endcap regions (EE). Preshower detectors consisting of two planes of silicon sensors interleaved with a total of three radiation lengths of lead are located in front of each EE detector. The hadron forward (HF) calorimeter uses steel as an absorber and quartz fibers as the sensitive material. The two halves of the HF are located 11.2 m from the interaction region, one on each end, and together they provide coverage in the range $3.0 < |\eta| < 5.2$. They also serve as luminosity monitors.

Events of interest are selected using a two-tiered trigger system. The first level (L1), composed of custom hardware processors, uses information from the calorimeters and muon detectors to select events at a rate of approximately 100 kHz within a fixed latency of $4\ \mu\text{s}$ [53]. The second level, known as the high-level trigger (HLT), consists of a farm of processors running a version of the full event reconstruction software optimized for fast processing, and reduces the event rate to around 1 kHz before data storage [54].

The primary vertex (PV) is taken to be the vertex corresponding to the hardest scattering in the event, evaluated using tracking information alone, as described in section 9.4.1 of ref. [55].

The electron momentum is estimated by combining the energy measurement in the ECAL with the momentum measurement in the tracker. The momentum resolution for electrons with transverse momentum $p_{\text{T}} \approx 45\ \text{GeV}$ from $Z \rightarrow ee$ decays ranges 1.6–5%. It is generally better in the EB than in EE, and also depends on the bremsstrahlung energy emitted by the electron as it traverses the material in front of the ECAL [56, 57].

Muons are reconstructed with detection planes made using three technologies: drift tubes, cathode strip chambers, and resistive-plate chambers. Matching muons to tracks measured in the silicon tracker results in a relative p_{T} resolution, for muons with p_{T} up to 100 GeV, of 1% in the barrel and 3% in the endcaps. The p_{T} resolution in the barrel is better than 7% for muons with p_{T} up to 1 TeV [58].

A more detailed description of the CMS detector, together with the definition of the coordinate system used and the relevant kinematic variables, can be found in ref. [59].

3 Data and simulated samples

This analysis is based on proton-proton collisions recorded by the CMS experiment at the LHC in 2016, 2017, and 2018, corresponding to integrated luminosities of 36.3, 41.5, and $59.8\ \text{fb}^{-1}$, respectively [60–62].

Candidate events are selected offline from leptons passing loose identification and isolation requirements [56, 58], following the online selection based on dielectron, dimuon, and electron-muon HLT algorithms. The various lepton p_{T} thresholds used in the online selection for each data-taking period are reported in table 1. Additional triggers that require three leptons with lower p_{T} thresholds and no isolation criteria, as well as single-electron and single-muon triggers, are used to increase the efficiency. Events selected with the single-lepton triggers are used to measure the trigger efficiency by means of the “tag-and-

	e/e (GeV)	μ/μ (GeV)	e/ μ , μ/e (GeV)
2016	17/12	17/8	17/8, 8/23
2017	23/12	17/8	23/8, 12/23
2018	23/12	17/8	23/8, 12/23

Table 1. Thresholds applied on the p_T of the leading/subleading leptons in each data-taking period for the main dielectron (e/e), dimuon (μ/μ), and electron-muon (e/ μ , μ/e) HLT algorithms.

probe” technique [63], following the strategy of ref. [35]. A “tag” lepton is defined as a lepton that matches geometrically a candidate from the single-lepton triggers, whereas the other leptons are used as “probes” and are combined together to form any of the triggers. The overall trigger efficiency measured in data is larger than 99% and is in agreement with that estimated from simulated samples.

Signal samples are simulated at next-to-leading order (NLO) in perturbative quantum chromodynamics (pQCD) using the POWHEG 2.0 [64–66] generator for the five main production mechanisms of the SM H boson: gluon fusion (ggH) [67], vector boson fusion (VBF) [68], associated production with a vector boson (VH, where V = W, Z) [69], and associated production with a pair of top quarks (t \bar{t} H) [70]. Events produced via the ggH mechanism are simulated at NLO with POWHEG 2.0 and reweighted to match the predictions at next-to-next-to-leading order in the strong coupling, including matching to a parton shower (NNLOPS) [71] as a function of the p_T^H and of the number of jets in the event. The gg \rightarrow ZH contribution to the ZH production mode is simulated at leading order (LO) using JHUGEN 7.3.0 [72–76]. The ggH production mechanism is simulated at NLO also with MADGRAPH5_amc@NLO using the HC_NLO_X0_UFO-HEFT model in the 5 flavor scheme [77]. The H boson is produced in association with 0, 1, or 2 jets in the final states, merged with the FxFx scheme. The top quark mass is set to 173.0 GeV in the simulation, but finite top mass effects in loops are filtered out. The H boson production in association with b quarks is not considered in this analysis as its impact on the unfolded distributions is expected to be negligible with respect to all the other production modes. The decay of the H boson to four leptons is modeled with JHUGEN 7.0.2. The simulation of the various production and decay modes is based on the theoretical predictions from refs. [78–100], which are summarized in ref. [34].

The main background processes originate from ZZ production from quark-antiquark annihilation and gluon fusion. The former is simulated at NLO in pQCD with POWHEG 2.0 [101], while the latter is generated at LO with MCFM 7.0.1 [102–105]. The reducible background contribution arising from the production of Z bosons with associated jets (Z+jets) is estimated with the data-driven technique already used in ref. [35] and described in section 7.2.

An additional sample of Drell-Yan plus jets (DY+jets) events is produced with MADGRAPH5_amc@NLO 2.4.2 for validation studies and for the training of the boosted decision tree (BDT) used for the identification and isolation requirements on electrons, as described in section 4. All other simulated samples are used to model the signal shape,

estimate backgrounds, optimize the analysis strategy, and evaluate the systematic uncertainties.

All Monte Carlo (MC) generators are interfaced with PYTHIA to simulate the parton showering and hadronization effects. Version 8.230 [106] is used for the three data-taking years with the CUETP8M1 tune [107] for 2016 and the CP5 tune [108] for 2017 and 2018. Parton distribution functions (PDFs) are taken from the NNPDF3.0 set [109] for the three data taking periods.

The response of the CMS detector is modeled using the GEANT4 [110, 111] package. The simulated events are reconstructed with the same algorithms used for data and the distribution of the number of pileup events per bunch crossing is reweighted to match that observed in the data.

4 Event reconstruction and selection

The particle-flow (PF) algorithm [112] aims to reconstruct and identify each individual particle in an event, with an optimized combination of information from the various elements of the CMS detector. The energy of photons is obtained from the ECAL measurement. The energy of electrons is determined from a combination of the electron momentum at the PV, as determined by the tracker, the energy of the corresponding ECAL cluster, and the energy sum of all bremsstrahlung photons spatially compatible with originating from the electron track. The momentum of muons is obtained from the combined information of the tracker and the muon chambers. The energy of charged hadrons is determined from a combination of their momentum measured in the tracker and the matching ECAL and HCAL energy deposits, corrected for the response of the calorimeters to hadronic showers. Finally, the energy of neutral hadrons is obtained from the corresponding corrected ECAL and HCAL energy deposits.

The information from the ECAL and the tracker is combined to reconstruct electrons [56] with $p_T^e > 7 \text{ GeV}$ within the geometrical acceptance of the detector, defined by the pseudorapidity region $|\eta^e| < 2.5$. The identification of electrons is performed with a BDT algorithm sensitive to the presence of bremsstrahlung along the electron trajectory, the geometrical and momentum-energy matching with the corresponding cluster in the ECAL, the features of the electromagnetic shower in the ECAL, and observables that discriminate against electrons originating from photon conversions. The isolation sums for electrons, defined similarly as for muons, are included in the BDT discriminant. This choice is proven to enhance the suppression of nonprompt electrons originating from hadron decays and from overlap of neutral and charged hadrons within jets [56] and has a better performance than a cutoff-based approach using the relative isolation. The BDT for the electron identification and isolation is implemented using the XGBOOST library [113]. The training is performed on a dedicated sample of DY+jets simulated events. Electron samples are divided into six mutually exclusive categories defined by two p_T ranges ($7 < p_T^e < 10 \text{ GeV}$ and $p_T^e > 10 \text{ GeV}$) and three η selections corresponding to the central barrel ($|\eta^e| < 0.8$), outer barrel ($0.8 < |\eta^e| < 1.479$), and endcaps ($1.479 < |\eta^e| < 2.5$). The BDT is trained separately for the three data-taking periods and the selection requirements are defined to

achieve the same signal efficiency for the three data taking periods (97% for $p_T^e > 10 \text{ GeV}$; 80% for $p_T^e < 10 \text{ GeV}$ in the barrel; 74% for $p_T^e < 10 \text{ GeV}$ in the endcap).

The information from the silicon tracker and the muon system [58] is combined to reconstruct muons with $p_T^\mu > 5 \text{ GeV}$ and $|\eta^\mu| < 2.4$. The matching between inner and outer tracks is performed starting either from the tracks in the silicon trackers or from those reconstructed in the muon system. Cases where inner tracks are matched to segments in only one or two muon detector layers are also considered, to cope with very-low- p_T muons that do not traverse the entire detector. Muon objects are selected from the muon track candidates by applying loose requirements on the track in the muon system and the inner tracker, taking into account also their compatibility with small energy deposits in the ECAL and HCAL.

A requirement on the relative isolation, $\mathcal{I}^\mu < 0.35$, is introduced to discriminate between muons from Z boson decays and those originating from hadron decays within jets, where \mathcal{I}^μ is defined as:

$$\mathcal{I}^\mu \equiv \left(\sum p_T^{\text{charged}} + \max [0, \sum p_T^{\text{neutral}} + \sum p_T^\gamma - p_T^{\mu,\text{PU}}] \right) / p_T^\mu, \quad (4.1)$$

and where $\sum p_T^{\text{charged}}$ is the scalar sum of the transverse momenta of charged hadrons originating from the PV, whereas $\sum p_T^{\text{neutral}}$ and $\sum p_T^\gamma$ are the scalar sums for neutral hadrons and photons, respectively. The isolation requirement is defined using a cone of radius $\Delta R = 0.3$ around the muon direction at the PV, with the angular distance between two particles i and j defined as $\Delta R(i, j) = \sqrt{(\Delta\eta_{i,j})^2 + (\Delta\phi_{i,j})^2}$. The quantity $p_T^{\mu,\text{PU}}$ in eq. (4.1) is defined from the p_T sum of all the charged hadrons i not originating from the PV as $p_T^{\mu,\text{PU}} \equiv 0.5 \sum_i p_{T,i}^{\mu,\text{PU}}$, where the factor of 0.5 corrects for using only the charged particles in the isolation cone [114]. The $p_T^{\mu,\text{PU}}$ contribution is subtracted in the definition of \mathcal{I}^μ to correct for energy deposits arising from pileup interactions.

Final-state radiation (FSR) photons arising from Z boson decays are recovered as follows. The PF photon candidates with $|\eta^\gamma| < 2.4$ are considered as FSR objects if they have $p_T^\gamma > 2 \text{ GeV}$ and a relative isolation $\mathcal{I}^\gamma < 1.8$, where \mathcal{I}^γ is defined similarly as for muons in eq. (4.1). These FSR candidates are associated with the closest lepton in the event and are not retained if $\Delta R(\gamma, \ell)/(p_T^\gamma)^2 > 0.012 \text{ GeV}^{-2}$ and $\Delta R(\gamma, \ell) > 0.5$. For each lepton, the FSR candidate with the lowest value of $\Delta R(\gamma, \ell)/(p_T^\gamma)^2$, if any, is selected. The photon candidates identified from the FSR recovery algorithm are excluded from the computation of the muon isolation.

Nonprompt leptons from decays of hadrons or photon conversions are suppressed based on the impact parameter significance. This variable is defined as the ratio of the 3-dimensional impact parameter, computed with respect to the position of the PV, to its uncertainty, and leptons are rejected if the value of this quantity is greater than 4.

The leptonic decays of known dilepton resonances are used to calibrate the momentum scale and resolution of electrons and muons in bins of p_T^ℓ and η^ℓ , as described in refs. [56, 58]. Efficiencies for the lepton reconstruction and selection are measured in several bins of p_T^ℓ and η^ℓ by means of the tag-and-probe technique using samples of Z boson events both in data and simulation. Simulated yields are corrected by the measured efficiency ratio between data and simulation.

For each event, hadronic jets are clustered from reconstructed particles using the infrared- and collinear-safe anti- k_T algorithm [115] with a distance parameter of 0.4 [116]. The jet momentum is computed from the vectorial sum of all particle momenta in the jet, and is found in simulation to be, on average, within 5 to 10% from the true momentum over the whole p_T spectrum and detector acceptance. Additional pp interactions within the same or nearby bunch crossings can contribute with additional tracks and calorimetric energy deposits, increasing the apparent jet momentum. To mitigate this effect, tracks identified as originating from pileup vertices are discarded and an offset correction is applied to correct for remaining contributions. Jet energy corrections are derived from simulation studies so that the average measured energy of jets becomes identical to that of particle-level jets. In situ measurements of the momentum balance in dijet, photon + jet, Z + jet, and multijet events are used to account for any residual differences in the jet energy scale between data and simulation [117]. Additional selection criteria are applied to remove jets potentially dominated by instrumental effects or reconstruction failures. Only jets with $p_T^{\text{jet}} > 30 \text{ GeV}$, $|\eta^{\text{jet}}| < 4.7$, and a distance parameter of $\Delta R(\ell/\gamma, \text{jet}) > 0.4$ from all selected leptons and FSR photons, are considered. Jets not satisfying the tight identification criteria and the criteria corresponding to the tight working point of the pileup jet identification algorithm described in ref. [114] are also discarded.

The PF objects mentioned above serve as input to the event selection, which targets events containing at least four well-identified and isolated leptons originating from the PV and possibly accompanied by a FSR photon. The FSR photons are included in the invariant mass computations. The event selection, which closely follows that employed in ref. [35], is detailed below.

The Z boson candidates are formed from pairs of same-flavor and opposite-charge leptons (e^+e^- , $\mu^+\mu^-$) with an invariant mass within $12 < m_{\ell^+\ell^-} < 120 \text{ GeV}$. Two such pairs are required to create ZZ candidates, where the Z boson candidate with invariant mass closest to the world-average Z boson mass [118] is referred to as Z_1 , whereas Z_2 denotes the other Z boson candidate. Three mutually exclusive subchannels are defined from the flavors of the four leptons in the event: 4e, 4μ, and 2e2μ.

The ZZ candidates must fulfill additional requirements designed to improve the sensitivity to H boson decays. The Z_1 candidates are required to have an invariant mass larger than 40 GeV. All lepton pairs (ℓ_i, ℓ_j) must be separated by an angular distance of $\Delta R(\ell_i, \ell_j) > 0.02$. Events must contain two leptons with $p_T > 10 \text{ GeV}$ and at least one with $p_T > 20 \text{ GeV}$. In the 4e and 4μ channels, where the same four leptons can be used to build an alternative Z_aZ_b candidate, candidates with $m_{Z_b} < 12 \text{ GeV}$ are not considered if Z_a is closer to the world-average Z boson mass than Z_1 and the event is rejected. This suppresses events with an on-shell Z accompanied by a low-mass dilepton resonance (e.g., J/ψ or Υ). The invariant mass of the four possible opposite-charge lepton pairs (irrespective of flavor), computed without FSR photons, must satisfy $m_{\ell^+\ell'^-} > 4 \text{ GeV}$ in order to further suppress events with leptons originating from hadron decays in jet fragmentation or from leptonic decays of low-mass resonances. The ZZ candidates are retained if the invariant mass of the four-lepton system $m_{4\ell}$ is larger than 70 GeV.

In events where more than one ZZ candidate satisfies the selection requirements above, the one with the largest scalar sum of transverse momenta of the two leptons defining the Z_2 is retained.

Finally, only events with $105 < m_{4\ell} < 160 \text{ GeV}$ are considered for the statistical analysis.

5 Fiducial phase space definition

Cross sections are measured in a fiducial phase space defined to match closely the experimental acceptance of the reconstruction-level selections. The fiducial phase space is defined at generator-level, following the strategy adopted in previous $H \rightarrow ZZ \rightarrow 4\ell$ analyses [18, 35]. It relies on requirements on the lepton kinematics and isolation, and on the event topology, in order to minimize the model dependence of the results.

The definition of the fiducial phase space is summarized in table 2. The events are retained if the leading (subleading) lepton has $p_T > 20(10) \text{ GeV}$. Additional electrons (muons) that may be present in the event are required to have $p_T > 7(5) \text{ GeV}$ and $|\eta| < 2.5(2.4)$. Lepton isolation is ensured by requiring the scalar sum of the p_T of all stable particles, i.e., those particles not decaying in the detector volume, within a cone of radius $\Delta R = 0.3$ to be less than 0.35 times the p_T of the lepton. Neutrinos, FSR photons, and leptons (electrons and muons) are not included in the computation of the isolation sum to enhance the model independence of the measurements, following the findings of ref. [25]. Events passing these requirements are retained if they have at least two same-flavor, opposite-sign lepton pairs. The pair with invariant mass closest to the world-average Z boson mass [118] is labeled as Z_1 and it must have $40 < m_{Z_1} < 120 \text{ GeV}$. The second Z boson candidate is referred to as Z_2 and it must have $12 < m_{Z_2} < 120 \text{ GeV}$. Each lepton pair ℓ_i, ℓ_j must be separated by $\Delta R(\ell_i, \ell_j) > 0.02$, while any opposite-sign lepton pair must satisfy $m_{\ell^+\ell'^-} > 4 \text{ GeV}$, reflecting the selection criteria used at reconstruction level.

Leptons at the fiducial level are considered as *dressed*, i.e., FSR photons are collected within a cone of radius 0.3. Jets do not enter in the definition of the fiducial phase space, but they are used when dealing with jet observables. Jets at the fiducial level are built with the anti- k_T clustering algorithm with a distance parameter of 0.4 out of stable particles, excluding neutrinos. Jets are retained if they satisfy $p_T^{\text{jet}} > 30 \text{ GeV}$ and $|\eta^{\text{jet}}| < 4.7$, similarly to the condition used at reconstruction level. Only jets with no leptons inside a cone of radius 0.4 are kept.

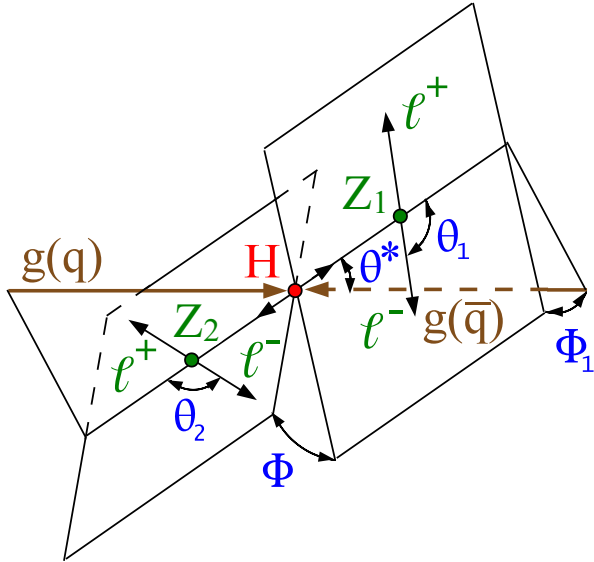
6 Observables

Fiducial cross sections are measured in bins of several kinematic observables sensitive to the H boson production and decay $\text{pp} \rightarrow H \rightarrow ZZ \rightarrow 4\ell$, of which a schematic representation is given in figure 1.

The decay of the H boson to four leptons is fully described by the invariant mass of the two Z boson candidates, three angles describing the Z boson decays (Φ, θ_1, θ_2), and two angles connecting production to decay (Φ_1, θ^*). The angle θ^* is defined in the H rest frame

Requirements for the $H \rightarrow ZZ \rightarrow 4\ell$ fiducial phase space

Lepton kinematics and isolation	
Leading lepton p_T	$p_T > 20 \text{ GeV}$
Sub-leading lepton p_T	$p_T > 10 \text{ GeV}$
Additional electrons (muons) p_T	$p_T > 7(5) \text{ GeV}$
Pseudorapidity of electrons (muons)	$ \eta < 2.5 \text{ (2.4)}$
Sum of scalar p_T of all stable particles within $\Delta R < 0.3$ from lepton	$< 0.35 p_T$
Event topology	
Existence of at least two same-flavor OS lepton pairs, where leptons satisfy criteria above	
Inv. mass of the Z_1 candidate	$40 < m_{Z_1} < 120 \text{ GeV}$
Inv. mass of the Z_2 candidate	$12 < m_{Z_2} < 120 \text{ GeV}$
Distance between selected four leptons	$\Delta R(\ell_i, \ell_j) > 0.02 \text{ for any } i \neq j$
Inv. mass of any opposite sign lepton pair	$m_{\ell^+ \ell^-} > 4 \text{ GeV}$
Inv. mass of the selected four leptons	$105 < m_{4\ell} < 160 \text{ GeV}$

Table 2. Summary of the requirements used in the definition of the fiducial phase space for the $H \rightarrow ZZ \rightarrow 4\ell$ cross section measurements.**Figure 1.** Schematic representation of the $gg/q\bar{q} \rightarrow H \rightarrow ZZ \rightarrow 4\ell$ process. The five angles depicted in blue are considered in the differential analysis, as detailed in the text.

as the angle between the beam axis and the direction of the Z_1 candidate. Φ and Φ_1 are the azimuthal angles between the three planes constructed from the H decay products and the decay products of the two Z bosons in the H rest frame. The θ_1 and θ_2 angles are defined in the Z_1 and Z_2 rest frames, respectively, as the angles between the Z boson direction in the H boson rest frame and the direction of the negative decay lepton. The set comprising these seven observables is hereafter referred to as $\tilde{\Omega}^{H \rightarrow ZZ \rightarrow 4\ell}(\theta^*, \theta_1, \theta_2, \Phi, \Phi_1, m_{Z1}, m_{Z2} | m_{4\ell})$ and can be used to build matrix element discriminants sensitive to the 4ℓ decay, as detailed in section 6.1. Fiducial cross sections are measured in differential bins of these observables, except for the θ angles for which their cosine is used. The distributions as a function of p_T^H and pseudorapidity of the reconstructed H boson are also measured.

Fiducial cross sections are also measured in differential bins of the number of associated jets (N_{jets}) and p_T of the leading ($p_T^{j_1}$) and subleading ($p_T^{j_2}$) jet in the event. For events with two or more jets the properties of the dijet system constituted by the two leading jets are assessed by measuring differential cross sections in bins of its invariant mass (m_{jj}), of the difference in pseudorapidity ($\Delta\eta_{jj}$), and of the difference in azimuthal angle ($\Delta\phi_{jj}$) between the two jets. The angle $\Delta\phi_{jj}$ is defined to be invariant under the exchange of the two jets as follow:

$$\Delta\phi_{jj} = \frac{(\hat{j}_{T1} \times \hat{j}_{T2}) \cdot \hat{z}}{|(\hat{j}_{T1} \times \hat{j}_{T2}) \cdot \hat{z}|} \cdot \frac{(\vec{j}_1 - \vec{j}_2) \cdot \hat{z}}{|(\vec{j}_1 - \vec{j}_2) \cdot \hat{z}|} \cdot \cos^{-1}(\hat{j}_{T1} \cdot \hat{j}_{T2}) \quad (6.1)$$

where the vectors $\vec{j}_{1,2}$ represent the direction of the leading and subleading jet in the laboratory frame, and the unit vectors $\hat{j}_{T1,2}$ the corresponding transverse component. This definition is also independent of the choice of the positive z axis direction, \hat{z} .

The rapidity-weighted jet vetoes \mathcal{T}_C^{\max} and \mathcal{T}_B^{\max} are also studied. These are defined, following ref. [119], as:

$$\mathcal{T}_C^{\max} = \max_j \left(\frac{\sqrt{E_j^2 - p_{z,j}^2}}{2 \cosh(y_j - y_H)} \right), \quad (6.2)$$

$$\mathcal{T}_B^{\max} = \max_j \left(m_T^j e^{-|y_j - y_H|} \right), \quad (6.3)$$

where y_j and m_T^j are the rapidity and transverse mass of the jet, defined from its mass m and momentum p as $m_T^j = \sqrt{m^2 + p_x^2 + p_y^2}$, while y_H is the rapidity of the H boson. The value of each observable is computed for each jet in the event and its maximum value is taken for each event. Since their resummation structure is different from the canonical p_T^j , they give complementary information on the properties of jets in an event and can be used as a test of quantum chromodynamics (QCD) resummation. The 0-jet phase space can be redefined using these observables. The events with no jets are defined as the ones with $\mathcal{T}_C^{\max} < 15 \text{ GeV}$ and $\mathcal{T}_B^{\max} < 30 \text{ GeV}$, where the values of these cuts are chosen accordingly to the findings of ref. [119]. In the following, these events will be defined as 0-jet| \mathcal{T}_C^{\max} and 0-jet| \mathcal{T}_B^{\max} , respectively.

The properties of the H +jet(s) system are also studied by measuring differential cross sections in bins of the transverse momentum and invariant mass of the H plus leading jet

system for events with at least one jet, or of the H plus leading and subleading jet system for events with at least two jets. The observables characteristic of the $H + j(j)$ system can be defined only in events with at least one (two) jets. In all other cases, an underflow bin is introduced to consider all events for which the observable is undefined.

6.1 Matrix element discriminants

The JHUGEN and MCFM generators are used to compute the matrix element probability \mathcal{P}_i for an event to arise from a physical process i , given the value of the reconstructed invariant mass of the four-lepton system $m_{4\ell}$. These probabilities are defined as a function of $\vec{\Omega}^{H \rightarrow ZZ \rightarrow 4\ell}$ and retain the maximal information on the underlying physics content of each event. Hence, the $\mathcal{P}_i(\vec{\Omega}^{H \rightarrow ZZ \rightarrow 4\ell})$ probabilities are used to construct likelihood-ratio-like matrix element discriminants sensitive to the difference between two physical processes a and b , when considering two production mechanisms, or to be used to test a BSM hypothesis against the SM scenario. These matrix element discriminants have been widely used in the context of $H \rightarrow ZZ \rightarrow 4\ell$ analyses, from the measurement of the H boson properties [35] to the constraints on possible anomalous couplings [31]. The general structure of these discriminants is an adaptation of the more classic likelihood ratio, properly rescaled to ensure that the discriminants are always bounded between 0 and 1. Two types of kinematic discriminants can be built to test the compatibility between signal (“sig”) and alternative (“alt”) hypotheses and their interference (“int”):

$$\mathcal{D}_{\text{alt}}(\vec{\Omega}) = \frac{\mathcal{P}_{\text{sig}}(\vec{\Omega})}{\mathcal{P}_{\text{sig}}(\vec{\Omega}) + \mathcal{P}_{\text{alt}}(\vec{\Omega})}, \quad \mathcal{D}_{\text{int}}(\vec{\Omega}) = \frac{\mathcal{P}_{\text{int}}(\vec{\Omega})}{2 \sqrt{\mathcal{P}_{\text{sig}}(\vec{\Omega}) \mathcal{P}_{\text{alt}}(\vec{\Omega})}}, \quad (6.4)$$

where \mathcal{P}_{sig} and \mathcal{P}_{alt} are the probabilities of an event under the two considered hypotheses, given their kinematic properties $\vec{\Omega}$, and \mathcal{P}_{int} is the probability for the interference between the two model contributions (“sig” and “alt”). This definition of \mathcal{D}_{int} is bounded between -1 and 1 for any value of \mathcal{D}_{alt} .

A total of six matrix element discriminants sensitive to different values of possible anomalous couplings of the H boson to vector bosons are considered. The general scattering amplitude describing the interaction between a spin-zero H boson and two spin-one gauge bosons V_1 and V_2 can be written, following the conventions of ref. [31], as:

$$A(HV_1V_2) = \frac{1}{v} \left[a_1^{\text{VV}} + \frac{\kappa_1^{\text{VV}} q_{V1}^2 + \kappa_2^{\text{VV}} q_{V2}^2}{(\Lambda_1^{\text{VV}})^2} + \frac{\kappa_3^{\text{VV}} (q_{V1} + q_{V2})^2}{(\Lambda_Q^{\text{VV}})^2} \right] m_{V1}^2 \epsilon_{V1}^* \epsilon_{V2}^* + \frac{1}{v} a_2^{\text{VV}} f_{\mu\nu}^{*(1)} f^{*(2),\mu\nu} + \frac{1}{v} a_3^{\text{VV}} f_{\mu\nu}^{*(1)} \tilde{f}^{*(2),\mu\nu}, \quad (6.5)$$

where v is the vacuum expectation value of the H potential, $f^{(i)\mu\nu} = \epsilon_{Vi}^\mu q_{Vi}^\nu - \epsilon_{Vi}^\nu q_{Vi}^\mu$, $\tilde{f}_{\mu\nu}^{(i)} = \frac{1}{2} \epsilon_{\mu\nu\rho\sigma} f^{(i),\rho\sigma}$, and ϵ_{Vi} , q_{Vi} , and m_{Vi} are the polarization vector, four-momentum, and pole mass of a gauge boson, respectively. The constants Λ_1 and Λ_Q are the scales of BSM physics. In the above equation, the only leading tree-level contributions are $a_1^{\text{ZZ}} \neq 0$

	\mathcal{D}_{alt}				\mathcal{D}_{int}	
	Coupling					
	a_3	a_2	Λ_1	$\Lambda_1^{Z\gamma}$	a_3	a_2
Discriminant	$\mathcal{D}_{0^-}^{\text{dec}}$	$\mathcal{D}_{0h+}^{\text{dec}}$	$\mathcal{D}_{\Lambda 1}^{\text{dec}}$	$\mathcal{D}_{\Lambda 1}^{Z\gamma,\text{dec}}$	$\mathcal{D}_{\text{CP}}^{\text{dec}}$	$\mathcal{D}_{\text{int}}^{\text{dec}}$

Table 3. Matrix element kinematic discriminants considered in the analysis. Some discriminants have a special label to identify the targeted Higgs boson property rather than the name of the coupling. $\mathcal{D}_{0^-}^{\text{dec}}$ is sensitive to a CP-odd Higgs boson, $\mathcal{D}_{\text{CP}}^{\text{dec}}$ is the observable sensitive to the CP-mixing, and $\mathcal{D}_{0h+}^{\text{dec}}$ is sensitive to heavy CP-even Higgs boson.

and $a_1^{\text{WW}} \neq 0$. The rest of the ZZ and WW couplings are considered as anomalous contributions, which are either small contributions arising in the SM due to loop corrections or new BSM contributions. The SM value of those are not yet distinguishable from zero experimentally with the available data.

The a_i and κ_i terms correspond to the strengths of vector boson couplings, following the notation adopted in ref. [31]. In particular, the a_3 CP-odd term is expected to be null in the SM and is sensitive to possible BSM effects that would result in CP violation. The a_2 term corresponds to the CP-even contribution to the HVV coupling and is sensitive to possible BSM contributions from heavy H bosons. The $\kappa_{1,2}/(\Lambda_1)^2$ and $\kappa_3/(\Lambda_Q)^2$ terms are sensitive to possible physics at a new energy scale represented by the denominator. The $\kappa_3/(\Lambda_Q)^2$ coupling allows for scenarios that violate the gauge symmetries of the SM but is not considered in this analysis. Symmetries and gauge invariance force $\kappa_1^{ZZ} = \kappa_2^{ZZ}$, leading to the single coupling $\kappa_1^{ZZ}/(\Lambda_1^{ZZ})^2$ to investigate and denoted Λ_1 in what follows. Gauge invariance imposes $\kappa_1^{Z\gamma} = 0$, making it impossible to measure the $\Lambda_1^{Z\gamma}$ coupling in any process involving an on-shell photon. However, the $H \rightarrow 4\ell$ channel contains events featuring an off-shell photon, i.e., $H \rightarrow Z\gamma^* \rightarrow 4\ell$, that can be used to study the $\Lambda_1^{Z\gamma}$ coupling. Table 3 details the set of kinematic discriminants considered and the couplings to which they are sensitive. The index “dec” indicates that only decay information is used to build these discriminants.

Differential cross sections are measured in bins of these six matrix element discriminants under the SM hypothesis. The compatibility of the measurements with the SM predictions is assessed by comparing the results with the discriminants built for alternative BSM scenarios, where HVV anomalous couplings are introduced by modifying the a_i and κ_i values in eq. (6.5) with respect to their SM values.

Tables 4 and 5 summarize the bin boundaries for all the observables considered in this analysis that target the H boson production and the $H \rightarrow ZZ \rightarrow 4\ell$ decay, respectively.

To ensure a complete characterization of the $H \rightarrow ZZ \rightarrow 4\ell$ decay channel and to maximize the coverage of different phase space regions, a set of double-differential measurements is also performed. Cross sections are measured in bins of m_{Z_1} vs. m_{Z_2} , $|y_H|$ vs. p_T^H , number of associated jets vs. p_T^H , p_T of the leading vs. subleading jet, p_T^{Hj} vs. p_T^H , and \mathcal{T}_C^{\max} vs. p_T^H . The corresponding bin boundaries are listed in table 6.

Observable	Definition	Bin boundaries
p_T^H	Transverse momentum of the 4ℓ system	$[0, 10, 20, 30, 45, 60, 80, 120, 200, \infty[$ GeV
$ y_H $	Rapidity of the 4ℓ system	$[0, 0.15, 0.3, 0.45, 0.6, 0.75, 0.9, 1.2, 1.6, 2.5]$
N_{jets}	Number of associated jets in the event	$=0, =1, =2, =3, \geq 4$
$p_T^{j_1}$	Transverse momentum of the leading jet	$[0\text{-jet}, 30, 55, 95, 200, \infty[$ GeV
$p_T^{j_2}$	Transverse momentum of the subleading jet	$[0/1\text{-jet}, 30, 40, 65, 90, \infty[$ GeV
\mathcal{T}_C^{\max}	Rapidity-weighted jet veto	$[0\text{-jet} \mathcal{T}_C^{\max}, 15, 20, 30, 50, 80, \infty[$ GeV
\mathcal{T}_B^{\max}	Rapidity-weighted jet veto	$[0\text{-jet} \mathcal{T}_B^{\max}, 30, 45, 75, 150, \infty[$ GeV
m_{jj}	Invariant mass of the leading and subleading jets system	$[0/1\text{-jet}, 0, 120, 300, \infty[$ GeV
$ \Delta\eta_{jj} $	Difference in pseudorapidities of the leading and subleading jets	$[0/1\text{-jet}, 0.0, 1.6, 3.0, 10.0]$
$\Delta\phi_{jj}$	Azimuthal angle difference between the leading and subleading jets	$[0/1\text{-jet}, -\pi, -\pi/2, 0, \pi/2, \pi]$
p_T^{Hj}	Transverse momentum of the 4ℓ and leading jet system	$[0\text{-jet}, 0, 30, 50, 110, \infty[$ GeV
m_{Hj}	Invariant mass of the 4ℓ and leading jet system	$[0\text{-jet}, 110, 180, 220, 300, 400, 600, \infty[$ GeV
p_T^{Hjj}	Transverse momentum of the 4ℓ , leading and subleading jets system	$[0/1\text{-jet}, 0, 20, 60, \infty[$ GeV

Table 4. Bin boundaries for one-dimensional observables targeting the H boson production. The bin boundaries denoted with ∞ correspond to no upper limit applied on the observable value.

Observable	Definition	Bin boundaries
$\cos\theta^*$	Cosine of the decay angle of the leading lepton pair in the 4ℓ rest frame	$[-1.0, -0.75, -0.50, -0.25, 0.0, 0.25, 0.50, 0.75, 1.0]$
$\cos\theta_1, \cos\theta_2$	Cosine of the production angle, relative to the Z vector, of the antileptons from the two Z bosons	$[-1.0, -0.75, -0.50, -0.25, 0.0, 0.25, 0.50, 0.75, 1.0]$
Φ, Φ_1	Azimuthal angles between the decay planes	$[-\pi, -3\pi/4, -\pi/2, -\pi/4, 0, \pi/4, \pi/2, 3\pi/4, \pi]$
m_{Z_1}	Invariant mass of the two leading leptons	$[40, 65, 75, 85, 92, 120]$ GeV
m_{Z_2}	Invariant mass of the two subleading leptons	$[12, 20, 25, 28, 32, 40, 50, 65]$ GeV
$\mathcal{D}_{0-}^{\text{dec}}$	Matrix element discriminant targeting a_3 coupling	$[0.0, 0.4, 0.5, 0.6, 0.7, 0.8, 0.9, 1.0]$
$\mathcal{D}_{0h+}^{\text{dec}}$	Matrix element discriminant targeting a_2 coupling	$[0.0, 0.35, 0.4, 0.45, 0.55, 0.65, 0.75, 1.0]$
$\mathcal{D}_{A1}^{\text{dec}}$	Matrix element discriminant targeting k_1 coupling	$[0.0, 0.45, 0.5, 0.6, 0.7, 1.0]$
$\mathcal{D}_{A1}^{\text{Z}\gamma, \text{dec}}$	Matrix element discriminant targeting $k_2^{\text{Z}\gamma}$ coupling	$[0.0, 0.35, 0.45, 0.5, 0.55, 0.65, 1.0]$
$\mathcal{D}_{CP}^{\text{dec}}$	Interference matrix element discriminant targeting a_3 coupling	$[-0.75, -0.25, -0.1, 0.0, 0.1, 0.25, 0.75]$
$\mathcal{D}_{\text{int}}^{\text{dec}}$	Interference matrix element discriminant targeting a_2 coupling	$[0.0, 0.7, 0.8, 0.9, 0.95, 1.0]$

Table 5. Bin boundaries for one-dimensional observables targeting the $H \rightarrow ZZ \rightarrow 4\ell$ decay.

7 Background estimation

7.1 Irreducible backgrounds

Irreducible ZZ background contributions arising from $q\bar{q}$ annihilation or gluon fusion are estimated from simulation. The former is simulated at NLO in pQCD with `POWHEG 2.0` and reweighted to NNLO using a K factor computed as a function of m_{ZZ} exploiting the NNLO computation of the $q\bar{q} \rightarrow ZZ$ fully differential cross section [120]. The K factor ranges 1.0–1.2 and is 1.1 at $m_{ZZ} = 125$ GeV. The NLO EW corrections are applied as a function of m_{ZZ} according to the computation presented in ref. [121].

Observable	Bin 1	Bin 2	Bin 3	Bin 4	Bin 5	Bin 6	Bin 7	Bin 8	Bin 9	Bin 10	Bin 11	Bin 12
m_{Z_1} (GeV)	[40,85]	[40,70]	[70,120]	[85,120]	[85,120]	[85,120]						
m_{Z_2} (GeV)	[12,35]	[35,65]	[35,65]	[30,35]	[24,30]	[12,24]						
$ y_H $	[0,0.5]	[0,0.5]	[0,0.5]	[0,0.5]	[0.5,1.0]	[0.5,1.0]	[0.5,1.0]	[1.0,2.5]	[1.0,2.5]	[1.0,2.5]		
p_T^H (GeV)	[0,40]	[40,80]	[80,150]	[150, ∞ [[0,45]	[45,120]	[120, ∞ [[0,45]	[45,120]	[120, ∞ [
N_{jets}	0	0	0		1	1	1	$>= 2$	$>= 2$	$>= 2$	$>= 2$	
p_T^H (GeV)	[0,15]	[15,30]	[30, ∞ [[0,60]	[60,80]	[80,120]	[120, ∞ [[0,100]	[100,170]	[170,250]	[250, ∞ [
$p_T^{j_1}$ (GeV)	$N_{\text{jets}} < 2$	[30,60]	[60,350]	[60,350]								
$p_T^{j_2}$ (GeV)		[30,60]	[30,60]	[60,350]								
p_T^{Hj} (GeV)	$N_{\text{jets}} < 1$	[0,30]	[0,45]	[30,350]	[45,350]							
p_T^H (GeV)		[0,85]	[85,350]	[0,85]	[85,350]							
\mathcal{T}_C^{\max} (GeV)	0-jet \mathcal{T}_C^{\max}	[15,25]	[15,25]	[25,40]	[25,40]	[40, ∞ [
p_T^H (GeV)	[0,15]	[15,30]	[30,45]	[45,70]	[70,120]	[120, ∞ [[0,120]	[120, ∞ [[0,120]	[120, ∞ [[0,200]	[200, ∞ [

Table 6. Double-differential observables with their corresponding bin boundaries. The bin boundaries denoted with ∞ correspond to no upper limit applied on the observable value.

The soft collinear approximation has been shown to describe accurately the cross section and the interference term for the gluon fusion ZZ production at NNLO in pQCD [122]. Additional calculations demonstrate that the K factors are very similar at NLO for signal and background [123] and at NNLO for the signal and interference terms [124]. Hence, the same K factor is used for the signal and the background [125]. The HNNLO v2 program [126–128] is used to obtain the signal NNLO K factor as a function of m_{ZZ} from the ratio of the NNLO and LO $gg \rightarrow H \rightarrow 2\ell 2\ell'$ cross sections for the predicted SM H boson decay width of 4.07 MeV [118]. The NNLO/LO K factor for $gg \rightarrow ZZ$ varies from ≈ 2.0 to 2.6 and is 2.27 at $m_{ZZ} = 125$ GeV, and a 10% systematic uncertainty is used when it is applied to the background.

The irreducible background contributions are included as binned templates in the likelihood function separately for the three considered final states (4e, 4 μ , and 2e2 μ). The templates are normalized to the most accurate theoretical calculations for the $q\bar{q} \rightarrow ZZ \rightarrow 4\ell$ and $gg \rightarrow ZZ \rightarrow 4\ell$ cross sections [120–125]. A second method for the measurement of the inclusive fiducial cross section is presented in section 10, where the normalization of these processes is treated as an unconstrained parameter in the fit to assess the constraint that can be derived from sidebands in data.

7.2 Reducible background

The reducible background contribution to the H boson signal in the 4ℓ channel mainly comes from the Z+jets, t \bar{t} +jets, Z γ +jets, WW+jets, and WZ+jets production, hereafter collectively referred to as “Z+X” since the Z+jets contribution is the dominant one.

The contribution from the reducible background is estimated with the technique explained in ref. [35]. The method is based on lepton misidentification rates, which are defined as the fraction of non-signal leptons that satisfy the selection criteria, computed in a control region in data that includes a Z boson and exactly one additional “loose” lepton ($Z + \ell$),

i.e., leptons with p_T , η , and PV cuts but without identification nor isolation cuts applied. The lepton misidentification rates are then applied to another control region, comprised of a Z boson candidate and two opposite-sign or same-sign “loose” leptons ($Z + \ell\ell$), to reweigh the number of events to the signal region.

The distributions as functions of $m_{4\ell}$ of the $Z + \text{jets}$ reducible background are derived for the three final states (4μ , $4e$, and $2e2\mu$) separately and are included as binned templates in the likelihood function.

8 Measurement methodology

The $\text{pp} \rightarrow H \rightarrow ZZ \rightarrow 4\ell$ fiducial cross sections are extracted from a maximum likelihood fit of the signal and background expected distributions to the observed 4ℓ mass distribution, $N_{\text{obs}}(m_{4\ell})$, parametrized for each final state f , in each kinematic bin i of a given observable, and year of data taking y as:

$$\begin{aligned} N_{\text{obs}}^{f,i,y}(m_{4\ell}) &= N_{\text{fid}}^{f,i,y}(m_{4\ell}) + N_{\text{nonfid}}^{f,i,y}(m_{4\ell}) + N_{\text{nonres}}^{f,i,y}(m_{4\ell}) + N_{\text{bkg}}^{f,i,y}(m_{4\ell}) \\ &= \sum_j^{\text{genBin}} \epsilon_{i,j}^{f,y} (1 + f_{\text{nonfid}}^{f,i,y}) \sigma_{\text{fid}}^{f,i,y} \mathcal{L} \mathcal{P}_{\text{res}}^{f,y}(m_{4\ell}) \\ &\quad + N_{\text{nonres}}^{f,i,y} \mathcal{P}_{\text{nonres}}^{f,y}(m_{4\ell}) + N_{\text{bkg}}^{f,i,y} \mathcal{P}_{\text{bkg}}^{f,i,y}(m_{4\ell}). \end{aligned} \quad (8.1)$$

The $N_{\text{fid}}^{f,i,y}(m_{4\ell})$ and $N_{\text{nonfid}}^{f,i,y}(m_{4\ell})$ terms represent the distributions of resonant events originating from within and outside the fiducial volume, respectively. The $N_{\text{nonres}}^{f,i,y}(m_{4\ell})$ and $N_{\text{bkg}}^{f,i,y}(m_{4\ell})$ terms represent the distributions of nonresonant and background events.

The H resonant signal distribution is parametrized with a double-sided Crystal Ball (DCB) function [129] around $m_H = 125 \text{ GeV}$. The corresponding probability density function, $\mathcal{P}_{\text{res}}(m_{4\ell})$, is scaled by the fiducial cross section, σ_{fid} , and the integrated luminosity \mathcal{L} . The DCB function parameters are obtained from a simultaneous fit of the $m_{4\ell}$ distributions corresponding to the various mass points in the m_H range of $105\text{--}160 \text{ GeV}$, which allows to express the dependency of the fitted parameters in m_H directly in the fit, following the same strategy of ref. [35].

A Landau distribution is introduced to empirically model the shape of the nonresonant signal contribution, $\mathcal{P}_{\text{nonres}}(m_{4\ell})$, for the WH , ZH , and $t\bar{t}H$ processes where one of the leptons from the H boson decay is either not selected or falls outside the acceptance. The fraction of such events in the mass range considered is about 5, 22, and 17% for WH , ZH , and $t\bar{t}H$, respectively. These nonresonant events are treated as a background in the measurements. The reducible and irreducible backgrounds are included in the fit as normalized binned templates, \mathcal{P}_{bkg} , of the mass distribution of these processes.

An additional contribution (f_{nonfid}) is introduced to take into account the presence of events not originating from the fiducial volume but satisfying the selections and is treated as background in the measurements. This contribution is referred to as the “nonfiducial signal” and is estimated from simulation for each signal model. The values of f_{nonfid} are found to be consistent across the different observables considered, for the same production mechanism. Dedicated simulations have shown that the $m_{4\ell}$ distribution of these events is

Signal process	\mathcal{A}_{fid}	ϵ	f_{nonfid}	$(1 + f_{\text{nonfid}})\epsilon$
ggH (POWHEG)	0.408 ± 0.001	0.619 ± 0.001	0.053 ± 0.001	0.652 ± 0.001
VBF	0.448 ± 0.001	0.632 ± 0.002	0.043 ± 0.001	0.659 ± 0.002
WH	0.332 ± 0.001	0.616 ± 0.002	0.077 ± 0.001	0.664 ± 0.002
ZH	0.344 ± 0.002	0.626 ± 0.003	0.083 ± 0.002	0.678 ± 0.003
t̄tH	0.320 ± 0.002	0.614 ± 0.003	0.179 ± 0.003	0.725 ± 0.005

Table 7. Summary of the inputs to the maximum likelihood based unfolding. The fraction of signal events within the fiducial phase space (acceptance \mathcal{A}_{fid}), the reconstruction efficiency (ϵ) in the fiducial phase space, and the ratio of the number of reconstructed events outside the fiducial phase space to that of the ones inside the fiducial phase space (f_{nonfid}) are quoted for each production mechanism for $m_H = 125.38 \text{ GeV}$. The last column shows the value of $(1 + f_{\text{nonfid}})\epsilon$, which regulates the signal yield for a given fiducial cross section. All values are shown with their statistical uncertainty. The values for the ggH production mode are obtained using the POWHEG generator.

identical to that of the resonant fiducial signal. To minimize the model dependence of the measurement, the value of f_{nonfid} is fixed to be a fraction of the fiducial signal component. The values of this fraction are reported in table 7 and range between 4% for the VBF production mechanism and up to 18% for the t̄tH mode. The acceptance of the events originating from VH or t̄tH is lower than ggH and VBF events, reflecting the possible presence of leptons in the final states not produced by the H boson decay and resulting in larger values of f_{nonfid} for these production mechanisms.

Generator-level observables used in the definition of the fiducial phase space are smeared by detector effects at reconstruction level. The $\epsilon_{i,j}^f$ response matrix is obtained from simulation, for each final state f , and is used to unfold the number of expected events in bin i at the reconstruction level to the number of expected events of a given observable in bin j at the fiducial level. For the measurement of the inclusive fiducial cross section, $\epsilon_{i,j}^f$ corresponds to a single number, the efficiency, listed in the second column of table 7 for the various production mechanisms. The table also shows the acceptance \mathcal{A}_{fid} , defined as the fraction of signal events that fall within the fiducial phase space.

Systematic uncertainties are included in the form of nuisance parameters and the fiducial cross section measurements are obtained using an asymptotic approach [130] with a test statistic based on the profile likelihood ratio [131]. A maximum likelihood fit is performed simultaneously in all final states and bins of each observable, assuming $m_H = 125.38 \text{ GeV}$. The branching fractions of the H boson to the different final states ($4e, 4\mu, 2e2\mu$) are unconstrained parameters in the fit to increase the model independence of the measurements, following the strategy adopted in ref. [35]. A likelihood-based unfolding is performed to resolve the detector effects from the observed distributions to the fiducial phase space. This approach is the same as in refs. [35, 132] and allows to simultaneously unfold detector effects and perform the fit to extract the fiducial cross section. The analysis strategy of ref. [35] is extended by measuring separately the fiducial cross sections in $4e + 4\mu$ and $2e2\mu$ final states for observables targeting the $H \rightarrow ZZ \rightarrow 4\ell$ decay. This choice is driven by

the different physics in the final states containing different- and same-flavor leptons arising from the destructive interference between the two alternative methods of constructing the $H \rightarrow ZZ \rightarrow 4\ell$ diagrams in the same-helicity states in the case of identical leptons.

9 Systematic uncertainties

The integrated luminosities of the 2016, 2017, and 2018 data-taking periods are individually known with uncertainties in the range 1.2–2.5% [60–62], while the 2016–2018 integrated luminosity has an uncertainty of 1.6%. The partial correlation scheme considered for this systematic uncertainty is summarized in table 8.

Experimental systematic uncertainties in trigger and lepton reconstruction and selection efficiencies are estimated from data for different final states. These uncertainties are derived from a tag-and-probe technique using J/ψ and Z decays into a pair of leptons and range 4.3–10.9% in the 4e channel and 0.6–1.9% in the 4 μ channel, depending on the p_T region. In this paper, a new way to estimate the systematic uncertainty in the electron efficiency measurements is introduced. Alternative variations in the tag-and-probe fit used to derive the systematic uncertainty are combined and the RMS of the values is used for the systematic uncertainty evaluation. This makes the evaluation of the systematic uncertainty for the low- p_T bins more solid, and leads to their reduction of a factor approximately 40% in the electron reconstruction and selection efficiency with respect to the values reported in ref. [35].

The systematic uncertainties in the lepton momentum scale and resolution are estimated from dedicated studies of the $Z \rightarrow \ell^+\ell^-$ mass distribution in data and simulation. The momentum scale uncertainty is 0.06% in the 4e channel and 0.01% in the 4 μ channel, while the resolution uncertainty is 10% in the 4e channel and 3% in the 4 μ channel. The effect of these uncertainties is evaluated by allowing the corresponding parameters of the DCB function used to model the resonant signal to remain unconstrained in the fit.

Jet-related observables are affected by systematic uncertainties in the estimation of the jet energy scale. These uncertainties affect the normalization of the processes and are modeled with a set of nuisance parameters representing the various sources and accounting for the partial correlation among the various final states and years. Their values depend on the kinematic bin and range 0.1–33%, with an average value of 3%.

Furthermore, experimental systematic uncertainties in the reducible background estimation are considered. These uncertainties originate from the evaluation of the lepton misidentification rates and vary between 23 and 43%, depending on the final state. The impact of these uncertainties is negligible.

Table 8 summarizes the experimental systematic uncertainties considered in the analysis.

Theoretical uncertainties in the renormalization and factorization scales, and in the choice of the PDF set affect both the signal and background rates. The scale uncertainty is determined by varying renormalization and factorization scales between 0.5 and 2 times their nominal value, while keeping their ratio between 0.5 and 2. The uncertainty in the PDF set is determined following the PDF4LHC recommendations taking the root mean

Common experimental uncertainties			
	2016	2017	2018
Luminosity uncorrelated	1 %	2 %	1.5 %
Luminosity correlated 2016–2018	0.6 %	0.9 %	2 %
Luminosity correlated 2017–2018	—	0.6 %	0.2 %
Lepton id/reco efficiencies	0.7–10 %	0.6–8.5 %	0.6–9.5 %
Jet energy scale	0.1%–27%	0.1%–33%	0.1%–33%
Background related uncertainties			
Reducible background ($Z+X$)	25–43 %	23–36 %	24–36 %
Signal related uncertainties			
Lepton energy scale	0.06% (e)–0.01% (μ)	0.06% (e)–0.01% (μ)	0.06% (e)–0.01% (μ)
Lepton energy resolution	10% (e)–3% (μ)	10% (e)–3% (μ)	10% (e)–3% (μ)

Table 8. Summary of the input values of the experimental systematic uncertainties.

square of the variation of the results when using different replicas of the default NNPDF set [133]. An additional 10% uncertainty in the K factor used for the $gg \rightarrow ZZ$ background prediction is applied. A systematic uncertainty of 2% [34] in the branching fraction of $H \rightarrow ZZ \rightarrow 4\ell$ is considered and only affects the signal yield. The theoretical uncertainties affecting the signal are not included in the fit but evaluated and indicated in figures 4–24.

10 Results

This section reports the measurements of the fiducial cross sections in differential bins of the kinematic observables introduced in section 6. All fiducial cross section measurements are in agreement with the SM predictions within uncertainties. The compatibility of the results with the theoretical predictions is quantified by reporting the p -value for each observable, computed using the negative log-likelihood ratio as test statistic evaluated at the SM point. The p -value is calculated using a χ^2 probability density function with the number of bins used in the measurements taken as the number of degrees of freedom. The observed p -values range from 0.05 to 0.99. The inclusive cross section is measured with an overall precision of 10%, with statistical and systematic contributions of 8% and 6%, respectively. All the differential measurements are limited by the statistical uncertainty. The differential cross sections as functions of p_T^H and $|y_H|$ are measured with an average precision of 35%, while the most precise cross sections are measured with a precision of 20%. The measurements are compared to the theoretical predictions from various generators. The uncertainties in these predictions come from the uncertainty in the fiducial acceptance, the $H \rightarrow ZZ \rightarrow 4\ell$ branching fraction and variations of the PDF replicas, α_s value, and renormalization and factorization scales. Figure 2 depicts the distributions of these two observables comparing data to predictions from simulation. With respect to ref. [35], the data set used in this analysis benefits from an improved object calibration. This leads to a better precision in the final results and permits measurements

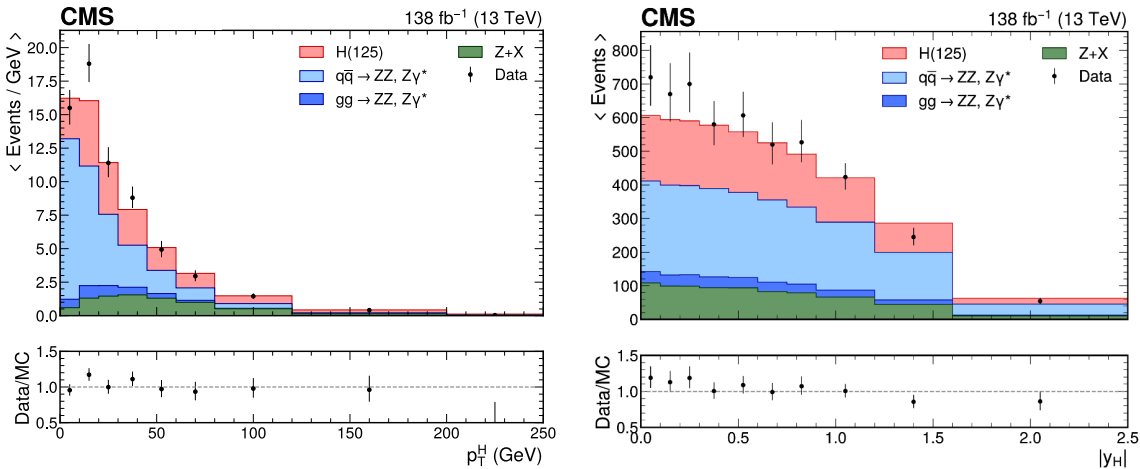


Figure 2. Reconstructed transverse momentum (left) and rapidity (right) of the four-lepton system for events with $105 < m_{4\ell} < 160$ GeV. Points with error bars represent the data, solid histograms the predictions from simulation. The y axes of the top panels have been rescaled to display the number of events per bin, divided by the width of each bin. The lower panels show the ratio of the measured values to the expectations from the simulation.

of jet-related observables in a phase space region that extends up to $|\eta| = 4.7$. The inclusive fiducial result features a reduction of 15% of the uncertainty, particularly evident in the 40% reduction of the systematic component obtained using a root-mean-square approach to compute the uncertainties in the electrons selection efficiency [134], which are the leading source of systematic uncertainty on the measurements performed in this analysis. Tabulated results are provided in the HEPData record for this analysis [135].

The kinematic properties of the four-lepton system are studied by measuring differential cross sections in bins of angular observables sensitive to the HVV decay. These results are reported for the inclusive four-lepton final state and for the same-flavor and different-flavor final states separately to account for interference effects in the case of identical helicity states. In all cases the results agree with the distributions predicted by the SM. The largest deviations with respect to the expected values are observed in the central bins of $\cos \theta_2$ and Φ and are compatible with statistical fluctuations in the observed data. The p -values of these two measurements are found to be 0.23 and 0.24, respectively, thus corroborating the compatibility with the SM predictions. For the first time, differential cross sections are measured in bins of kinematic discriminants sensitive to the presence of possible HVV anomalous couplings. These measurements are compared to the distributions of these discriminants computed under the SM hypothesis and under various anomalous coupling hypotheses. The former is always favored in the comparison with data.

A total of six double-differential measurements are also reported.

10.1 Inclusive cross section

The measured inclusive fiducial cross section for the $H \rightarrow ZZ \rightarrow 4\ell$ process is

$$\begin{aligned}\sigma^{\text{fid}} &= 2.73 \pm 0.22 \text{ (stat)} \pm 0.15 \text{ (syst)} \text{ fb} \\ &= 2.73 \pm 0.22 \text{ (stat)} \pm 0.12 \text{ (electrons)} \pm 0.05 \text{ (lumi)} \pm 0.05 \text{ (bkg)} \pm 0.03 \text{ (muons)} \text{ fb}\end{aligned}\quad (10.1)$$

for a H boson mass of $m_H = 125.38 \text{ GeV}$, in agreement with the SM expectation of $\sigma_{\text{fid}}^{\text{SM}} = 2.86 \pm 0.15 \text{ fb}$. Figure 3 shows the corresponding log-likelihood scan. The systematic component of the uncertainty is dominated by electron-related nuisance parameters (electrons), especially the electron selection efficiency that is the leading nuisance parameter in the four-lepton decay channel. The muon-related nuisance parameters (muons) and the uncertainties on the luminosity measurement (lumi) and on the background predictions (bkg) play a minor role on the overall systematic uncertainty on σ^{fid} . The inclusive fiducial cross section measured in the three final states ($4e$, 4μ , and $2e2\mu$) is shown in the left panel of figure 4, while the right panel depicts the evolution of the $H \rightarrow ZZ \rightarrow 4\ell$ fiducial cross section as a function of the center-of-mass energy. The results are compared with the cross sections predicted by the POWHEG, MADGRAPH5_aMC@NLO, and NNLOPS generators for the H boson production and parton showering, while the decay is always modeled by JHUGEN. The measurement of the inclusive fiducial cross section is repeated treating the normalization of the ZZ irreducible background processes as an unconstrained parameter in the fit. The results are presented in the left panel of figure 5 for the inclusive $H \rightarrow ZZ \rightarrow 4\ell$ measurement and the three final states considered. The correlation coefficient (ρ) between the inclusive fiducial cross section measurement and the ZZ normalization in the 4ℓ final state is found to be $\rho = -0.03$, while the correlations between the ZZ normalization in each final state and the corresponding fiducial cross section measurements are shown in the right panel of figure 5. The positive correlations observed between the ZZ background normalizations and the cross sections measured in the $4e$ and $2e2\mu$ final states are driven by the systematic uncertainties on the electrons reconstruction and identification, which are the leading nuisance parameters in the analysis.

The results are summarized in table 9. The measured cross sections, obtained with the ZZ normalization treated as an unconstrained parameter in the fit, are in agreement with the results obtained when the irreducible background normalization is constrained to the theoretical expectation. The uncertainty in this parameter when extracted from sidebands in data (7.5%) is larger than the theoretical uncertainty in its predictions (6.3%). For these reasons, in the following the ZZ normalization is fixed to the SM prediction.

10.2 Differential cross sections: production

Fiducial cross sections are measured in differential bins of observables sensitive to the H boson production. The results for the p_T^H and $|y_H|$ are shown in figure 6. Figure 7 shows the measurements of the fiducial cross sections in bins of the number of associated jets and of the p_T of the leading and subleading jet in the event. The fiducial cross section is also measured in bins of the invariant mass and difference in pseudorapidity of the dijet system, as shown

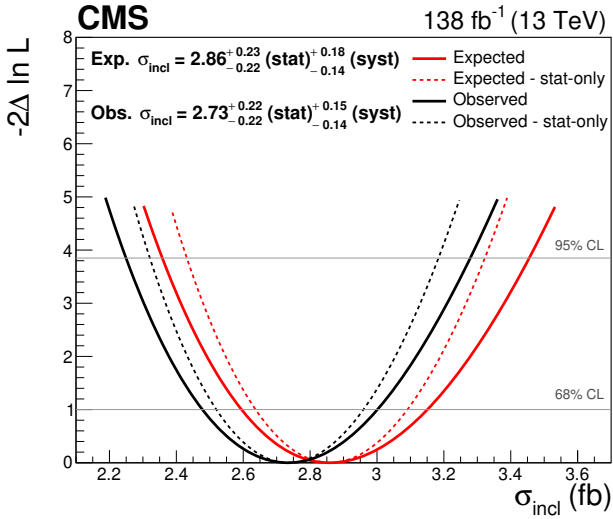


Figure 3. Log-likelihood scan for the measured inclusive fiducial cross section. The scan is shown with (solid line) and without (dashed line) systematic uncertainties profiled in the fit.

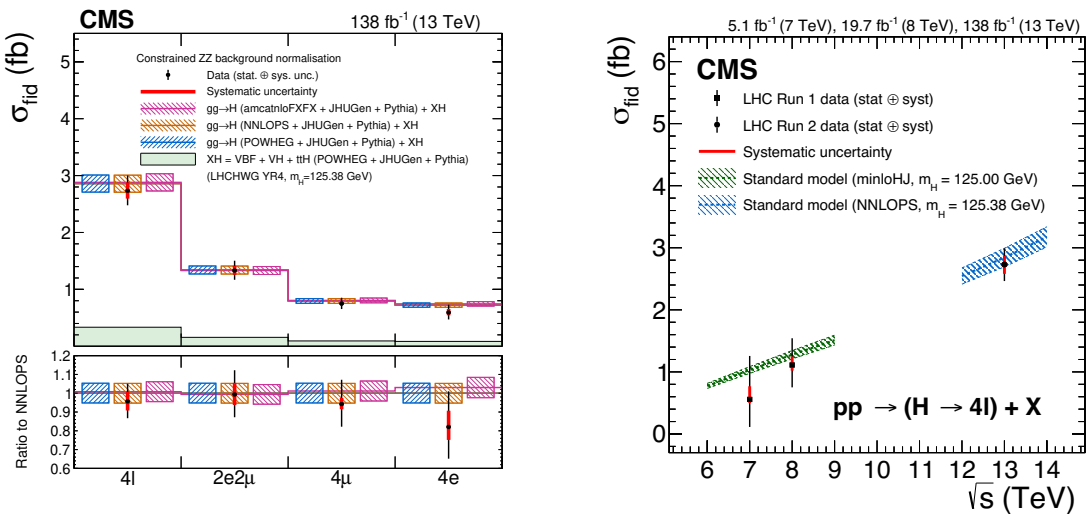


Figure 4. Measured inclusive fiducial cross section for the various final states (left); and as a function of the center-of-mass energy \sqrt{s} (right). In the left panel the acceptance and theoretical uncertainties are calculated using POWHEG (blue), NNLOPS (orange), and MADGRAPH5_aMC@NLO (pink). The subdominant component of the signal ($VBF + VH + t\bar{t}H$) is denoted as XH and is fixed to the SM prediction. In the right panel the acceptance is calculated using MINLOHJ at $\sqrt{s} = 13$ TeV and NNLOPS [128, 136] at $\sqrt{s} = 7$ and 8 TeV.

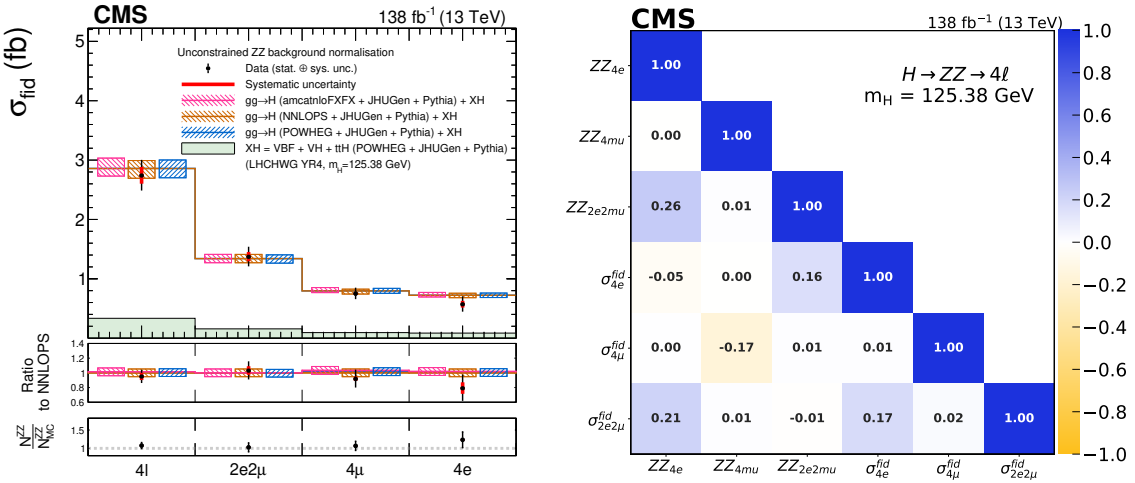


Figure 5. Inclusive fiducial cross section measured for the various final states with the irreducible backgrounds normalization ZZ unconstrained in the fit (left) and the corresponding correlation matrix (right). The acceptance and theoretical uncertainties in the differential bins are calculated using POWHEG (blue), NNLOPS (orange), and MADGRAPH5_amc@NLO (pink). The subdominant component of the signal (VBF + VH + t̄tH) is denoted as XH and it is fixed to the SM prediction. The ratio of the measured cross section to the theoretical prediction obtained from each generator is shown in the central panel, while the lower panel shows the ratio between the values derived from the measured ZZ normalization and the MC prediction.

	4e	4μ	2e2μ	Inclusive
Constrained ZZ background				
σ_{fid}	$0.59^{+0.13}_{-0.12} \text{ fb}$	$0.75^{+0.10}_{-0.09} \text{ fb}$	$1.33^{+0.17}_{-0.16} \text{ fb}$	$2.73^{+0.22}_{-0.22} (\text{stat})^{+0.15}_{-0.14} (\text{syst}) \text{ fb}$
Unconstrained ZZ background				
σ_{fid}	$0.57^{+0.15}_{-0.12} \text{ fb}$	$0.75^{+0.10}_{-0.09} \text{ fb}$	$1.37^{+0.17}_{-0.16} \text{ fb}$	$2.74^{+0.24}_{-0.23} (\text{stat})^{+0.14}_{-0.11} (\text{syst}) \text{ fb}$
N^{ZZ}	92^{+16}_{-13}	162^{+19}_{-18}	193^{+23}_{-21}	$445^{+27}_{-26} (\text{stat})^{+21}_{-19} (\text{syst})$
N^{ZZ}_{MC}	74^{+7}_{-8}	152^{+7}_{-8}	188^{+13}_{-14}	414^{+24}_{-28}

Table 9. Measured inclusive fiducial cross section and ± 1 standard deviation uncertainties for the various final states at $m_H = 125.38 \text{ GeV}$. The upper row summarizes the results obtained when the irreducible background normalization is constrained to the SM expectation and theoretical uncertainty, while the lower section present the results from a fit with the ZZ normalization treated as an unconstrained parameter. The first row presents the fiducial cross section, the middle row the ZZ background normalization extracted from the fit, and the bottom row the ZZ estimation from MC. The uncertainties on N_{MC}^{ZZ} are the pre-fit uncertainties summing the statistical and systematic uncertainty.

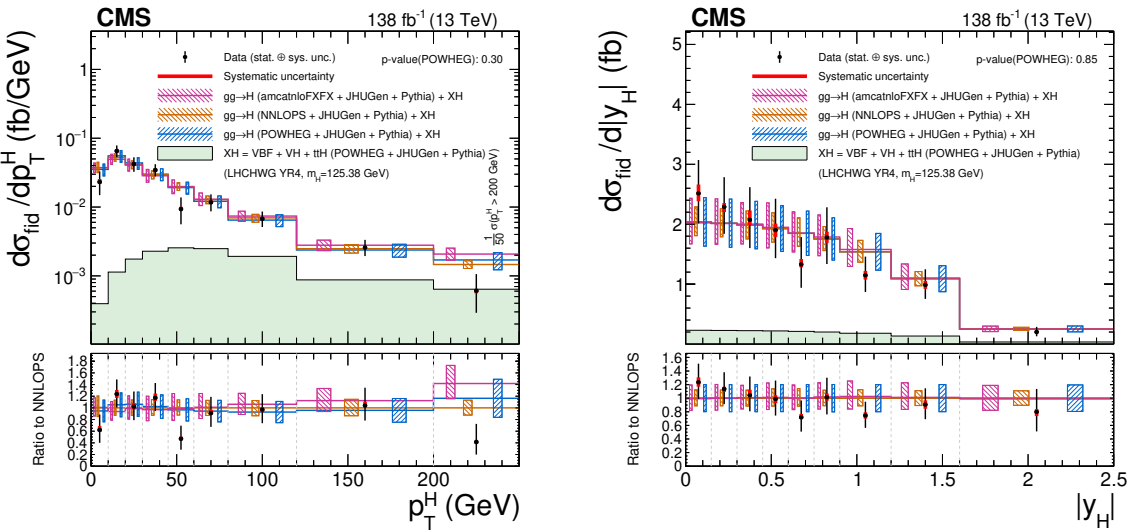


Figure 6. Differential cross sections as functions of the transverse momentum of the Higgs boson p_T^H (left) and of the rapidity of the Higgs boson $|y_H|$ (right). The fiducial cross section in the last bin (left) is measured for events with $p_T^H > 200 \text{ GeV}$ and normalized to a bin width of 50 GeV . The acceptance and theoretical uncertainties in the differential bins are calculated using the ggH predictions from three different generators normalized to next-to-next-to-next-to-leading order ($N^3\text{LO}$) [34]. The subdominant component of the signal ($\text{VBF} + \text{VH} + t\bar{t}\text{H}$) is denoted as XH and is fixed to the SM prediction. The measured cross sections are compared with the ggH predictions from POWHEG (blue), NNLOPS (orange), and MADGRAPH5_amc@NLO (pink). The hatched areas correspond to the systematic uncertainties in the theoretical predictions. Black points represent the measured fiducial cross sections in each bin, black error bars the total uncertainty in each measurement, red boxes the systematic uncertainties. The lower panels display the ratios of the measured cross sections and of the predictions from POWHEG and MADGRAPH5_amc@NLO to the NNLOPS theoretical predictions.

in figure 8. These measurements enhance the sensitivity to phase space regions where VBF and $t\bar{t}\text{H}$ production mechanisms dominate and where a larger jet multiplicity is expected.

Cross sections in bins of observables of the $\text{H} + j$ and $\text{H} + jj$ systems are also measured. The results in differential bins of the invariant mass and p_T of the $\text{H} + j$ system are presented in figure 9 together with the results in differential bins of the p_T of the $\text{H} + jj$ system.

Cross sections are also measured in differential bins of the rapidity-weighted jet vetoes introduced in section 6, to enhance the sensitivity to phase space regions that probe directly the departure from LO kinematics and the QCD emission pattern. Figure 10 presents the results for \mathcal{T}_C^{\max} and \mathcal{T}_B^{\max} .

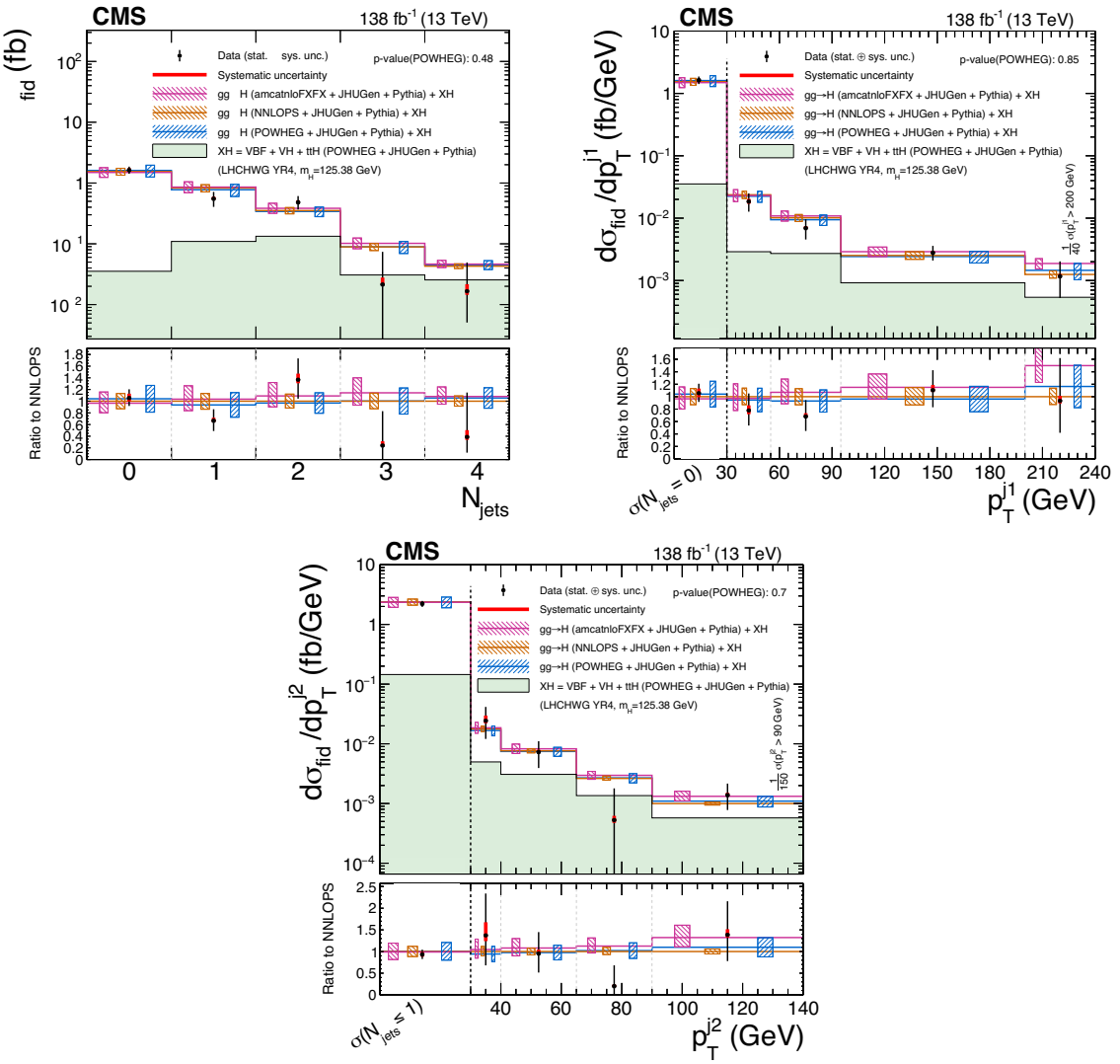


Figure 7. Differential cross sections as functions of the number of jets in the event (upper left) and of the p_T of the leading (upper right) and subleading (lower) jet. Upper right: the fiducial cross section in the last bin is measured for events with $p_T^{j1} > 200$ GeV and normalized to a bin width of 40 GeV. The first bin comprises all events with less than one jet, for which p_T^{j1} is undefined. Lower: the fiducial cross section in the last bin is measured for events with $p_T^{j2} > 90$ GeV and normalized to a bin width of 150 GeV. The first bin comprises all events with less than two jet, for which p_T^{j2} is undefined. The acceptance and theoretical uncertainties in the differential bins are calculated using the ggH predictions from three different generators normalized to next-to-next-to-next-to-leading order ($N^3\text{LO}$) [34]. The subdominant component of the signal ($\text{VBF} + \text{VH} + t\bar{t}\text{H}$) is denoted as XH and is fixed to the SM prediction. The measured cross sections are compared with the ggH predictions from POWHEG (blue), NNLOPS (orange), and MADGRAPH5_amc@NLO (pink). The hatched areas correspond to the systematic uncertainties in the theoretical predictions. Black points represent the measured fiducial cross sections in each bin, black error bars the total uncertainty in each measurement, red boxes the systematic uncertainties. The lower panels display the ratios of the measured cross sections and of the predictions from POWHEG and MADGRAPH5_amc@NLO to the NNLOPS theoretical predictions.

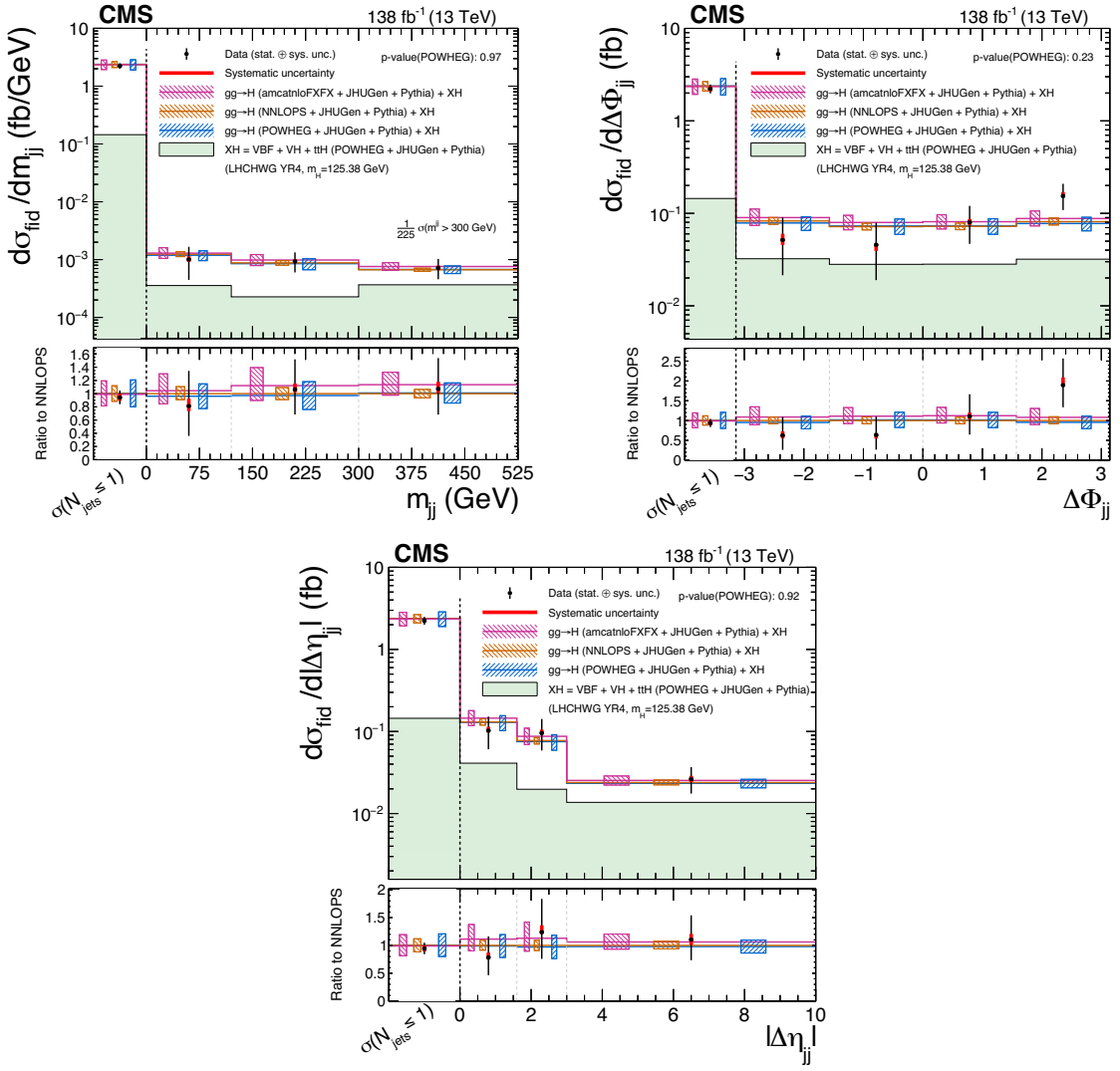


Figure 8. Differential cross sections as functions of the invariant mass m_{jj} (upper left), the difference in azimuthal angle $\Delta\phi_{jj}$ (upper right) the difference in pseudorapidity $|\Delta\eta_{jj}|$ (lower) of the dijet system. Upper Left: the fiducial cross section in the last bin is measured for events with $m_{jj} > 300$ GeV and normalized to a bin width of 225 GeV. The first bin comprises all events with less than two jets, for which m_{jj} is undefined. Upper right: the first bin comprises all events with less than two jet, for which $|\Delta\phi_{jj}|$ is undefined. Lower: the first bin comprises all events with less than two jet, for which $|\Delta\eta_{jj}|$ is undefined. The acceptance and theoretical uncertainties in the differential bins are calculated using the ggH predictions from three different generators normalized to next-to-next-to-next-to-leading order ($N^3\text{LO}$) [34]. The subdominant component of the signal (VBF + VH + $t\bar{t}H$) is denoted as XH and is fixed to the SM prediction. The measured cross sections are compared with the ggH predictions from POWHEG (blue), NNLOPS (orange), and MADGRAPH5_aMC@NLO (pink). The hatched areas correspond to the systematic uncertainties in the theoretical predictions. Black points represent the measured fiducial cross sections in each bin, black error bars the total uncertainty in each measurement, red boxes the systematic uncertainties. The lower panels display the ratios of the measured cross sections and of the predictions from POWHEG and MADGRAPH5_aMC@NLO to the NNLOPS theoretical predictions.

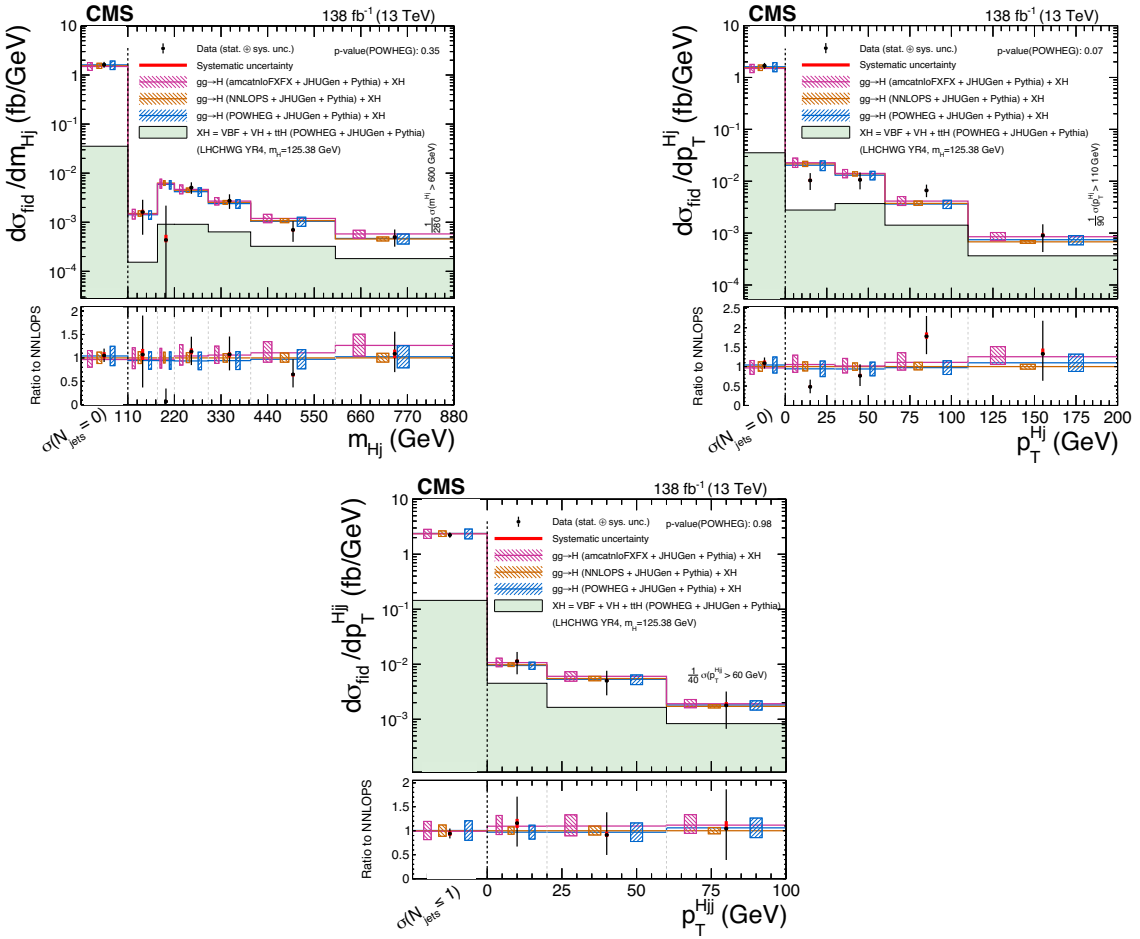


Figure 9. Upper left: differential cross sections as functions of the invariant mass of the $H + j$ system m_{Hj} , where j is the leading jet in the event. The fiducial cross section in the last bin is measured for events with $m_{Hj} > 600$ GeV and normalized to a bin width of 280 GeV. The first bin comprises all events with less than one jet, for which m_{Hj} is undefined. Upper right: differential cross sections as functions of the transverse momentum of the $H + j$ system p_T^{Hj} . The fiducial cross section in the last bin is measured for events with $p_T^{Hj} > 110$ GeV and normalized to a bin width of 90 GeV. The first bin comprises all events with less than one jet, for which p_T^{Hj} is undefined. Lower: differential cross sections as functions of the transverse momentum of the $H + jj$ system p_T^{Hjj} . The fiducial cross section in the last bin is measured for events with $p_T^{Hjj} > 60$ GeV and normalized to a bin width of 40 GeV. The first bin comprises all events with less than two jets, for which p_T^{Hjj} is undefined. The acceptance and theoretical uncertainties in the differential bins are calculated using the ggH predictions from three different generators normalized to next-to-next-to-next-to-leading order (N^3LO) [34]. The subdominant component of the signal (VBF + VH + $t\bar{t}H$) is denoted as XH and is fixed to the SM prediction. The measured cross sections are compared with the ggH predictions from POWHEG (blue), NNLOPS (orange), and MADGRAPH5_aMC@NLO (pink). The hatched areas correspond to the systematic uncertainties in the theoretical predictions. Black points represent the measured fiducial cross sections in each bin, black error bars the total uncertainty in each measurement, red boxes the systematic uncertainties. The lower panels display the ratios of the measured cross sections and of the predictions from POWHEG and MADGRAPH5_aMC@NLO to the NNLOPS theoretical predictions.

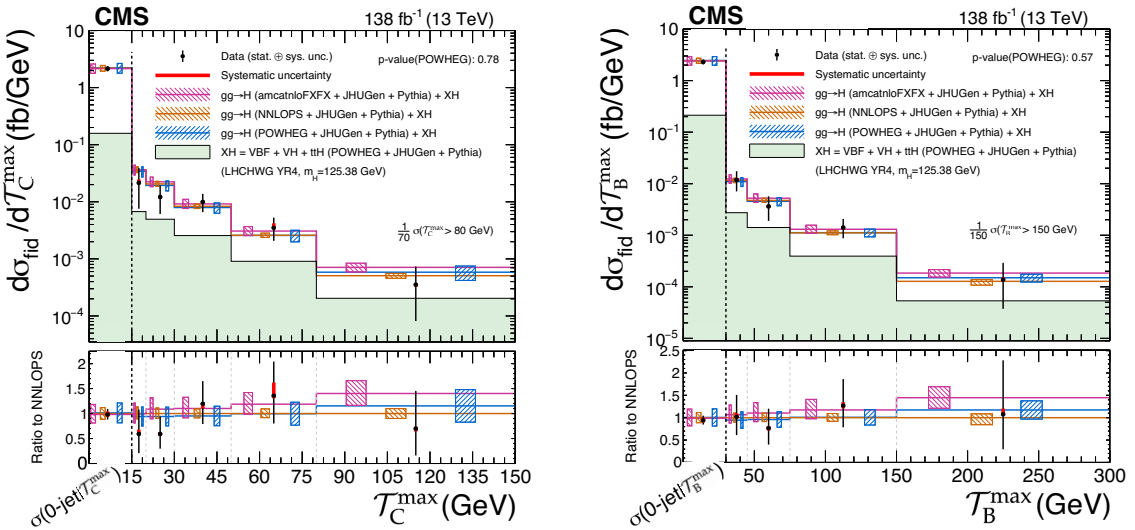


Figure 10. Left: differential cross sections as functions of the rapidity-weighed jet veto T_C^{\max} . The fiducial cross section in the last bin is measured for events with $T_C^{\max} > 80$ GeV and normalized to a bin width of 70 GeV. The first bin comprises all events in the 0-jet phase space region redefined as a function of T_C^{\max} , i.e., events with less than one jet, for which T_C^{\max} is undefined, and events with $T_C^{\max} < 15$ GeV. Right: differential cross sections as functions of the rapidity-weighed jet veto T_B^{\max} . The fiducial cross section in the last bin is measured for events with $T_B^{\max} > 150$ GeV and normalized to a bin width of 150 GeV. The first bin comprises all events in the 0-jet phase space region redefined as a function of T_B^{\max} , i.e., events with less than one jet, for which T_B^{\max} is undefined, and events with $T_B^{\max} < 30$ GeV. The acceptance and theoretical uncertainties in the differential bins are calculated using the ggH predictions from three different generators normalized to next-to-next-to-next-to-leading order ($N^3\text{LO}$) [34]. The subdominant component of the signal (VBF + VH + $t\bar{t}\text{H}$) is denoted as XH and is fixed to the SM prediction. The measured cross sections are compared with the ggH predictions from POWHEG (blue), NNLOPS (orange), and MADGRAPH5_aMC@NLO (pink). The hatched areas correspond to the systematic uncertainties in the theoretical predictions. Black points represent the measured fiducial cross sections in each bin, black error bars the total uncertainty in each measurement, red boxes the systematic uncertainties. The lower panels display the ratios of the measured cross sections and of the predictions from POWHEG and MADGRAPH5_aMC@NLO to the NNLOPS theoretical predictions.

10.3 Differential cross sections: decay

In this section the measurements of fiducial cross sections in differential bins of observables sensitive to the $H \rightarrow ZZ \rightarrow 4\ell$ decay are presented. Since the final state is sensitive to interference effects in the case of identical particles, the results for decay observables are also presented separately for same- and different-flavor final states. This ensures a complete coverage of the whole phase space and a more model-independent set of results.

The cross sections measured in bins of the invariant mass of the two Z boson candidates are shown in figures 11 and 12. The additional degrees of freedom that characterize the $H \rightarrow ZZ \rightarrow 4\ell$ decay are the five angles introduced in section 6. The cross sections in differential bins of the cosine of the θ angles are presented in figures 13, 14, and 15, respectively. Figures 16 and 17 show the results for the measurements in bins of the Φ and Φ_1 angles.

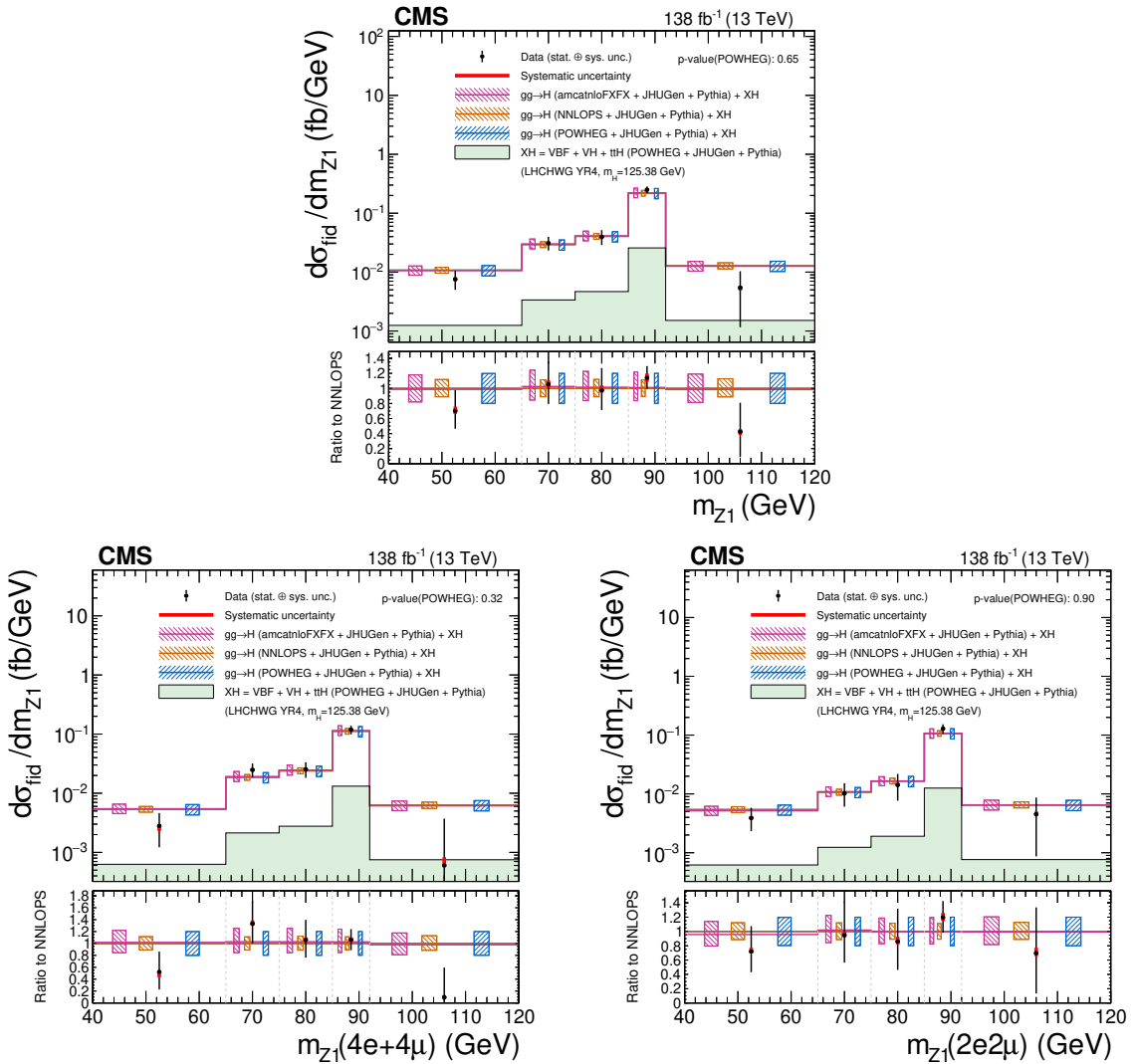


Figure 11. Differential cross sections as functions of the invariant mass of the leading dilepton pair m_{Z_1} in the 4ℓ (upper) and in the same-flavor (lower left) and different-flavor (lower right) final states. The acceptance and theoretical uncertainties in the differential bins are calculated using the ggH predictions from three different generators normalized to next-to-next-to-next-to-leading order (N^3LO) [34]. The subdominant component of the signal ($VBF + VH + t\bar{t}H$) is denoted as XH and is fixed to the SM prediction. The measured cross sections are compared with the ggH predictions from POWHEG (blue), NNLOPS (orange), and MADGRAPH5_amc@NLO (pink). The hatched areas correspond to the systematic uncertainties in the theoretical predictions. Black points represent the measured fiducial cross sections in each bin, black error bars the total uncertainty in each measurement, red boxes the systematic uncertainties. The lower panels display the ratios of the measured cross sections and of the predictions from POWHEG and MADGRAPH5_amc@NLO to the NNLOPS theoretical predictions.

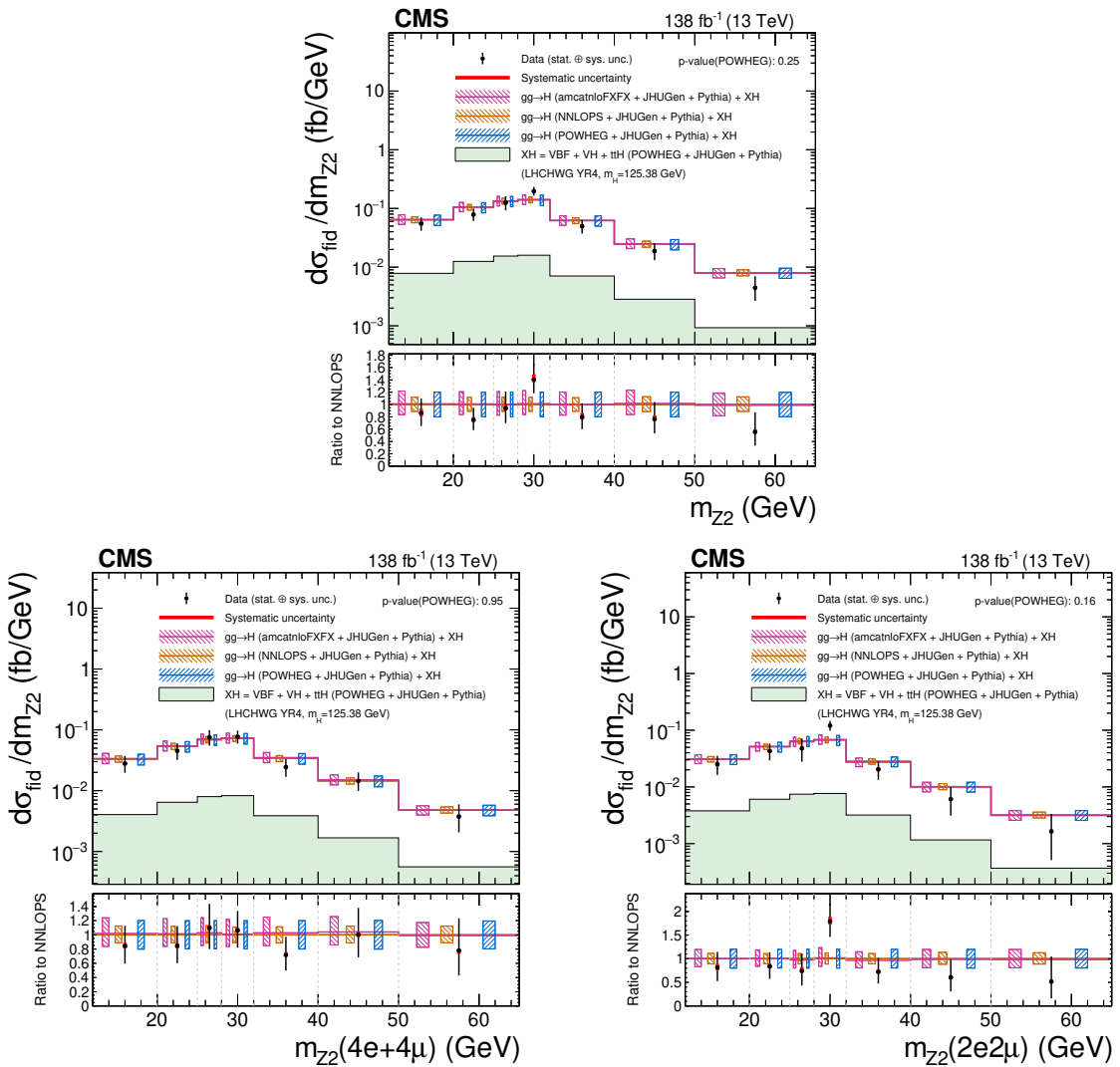


Figure 12. Differential cross sections as functions of the invariant mass of the subleading dilepton pair m_{Z_2} in the 4ℓ (upper) and in the same-flavor (lower left) and different-flavor (lower right) final states. The acceptance and theoretical uncertainties in the differential bins are calculated using the ggH predictions from three different generators normalized to next-to-next-to-next-to-leading order (N^3LO) [34]. The subdominant component of the signal ($VBF + VH + t\bar{t}H$) is denoted as XH and is fixed to the SM prediction. The measured cross sections are compared with the ggH predictions from POWHEG (blue), NNLOPS (orange), and MADGRAPH5_amc@NLO (pink). The hatched areas correspond to the systematic uncertainties in the theoretical predictions. Black points represent the measured fiducial cross sections in each bin, black error bars the total uncertainty in each measurement, red boxes the systematic uncertainties. The lower panels display the ratios of the measured cross sections and of the predictions from POWHEG and MADGRAPH5_amc@NLO to the NNLOPS theoretical predictions.

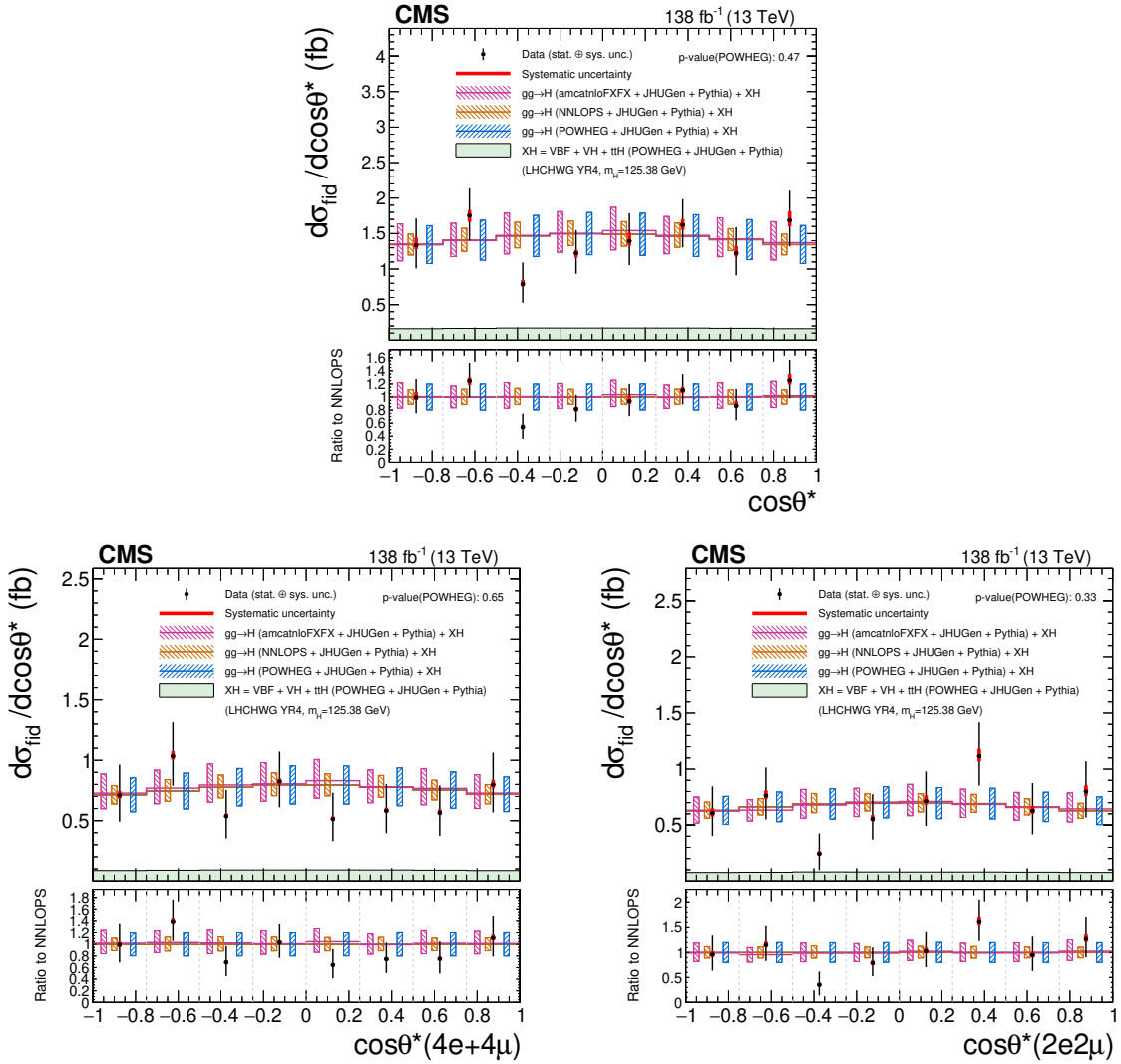


Figure 13. Differential cross sections as functions of $\cos\theta^*$ in the 4ℓ (upper) and in the same-flavor (lower left) and different-flavor (lower right) final states. The acceptance and theoretical uncertainties in the differential bins are calculated using the ggH predictions from three different generators normalized to next-to-next-to-next-to-leading order ($N^3\text{LO}$) [34]. The subdominant component of the signal (VBF + VH + t \bar{t} H) is denoted as XH and is fixed to the SM prediction. The measured cross sections are compared with the ggH predictions from POWHEG (blue), NNLOPS (orange), and MADGRAPH5_aMC@NLO (pink). The hatched areas correspond to the systematic uncertainties in the theoretical predictions. Black points represent the measured fiducial cross sections in each bin, black error bars the total uncertainty in each measurement, red boxes the systematic uncertainties. The lower panels display the ratios of the measured cross sections and of the predictions from POWHEG and MADGRAPH5_aMC@NLO to the NNLOPS theoretical predictions.

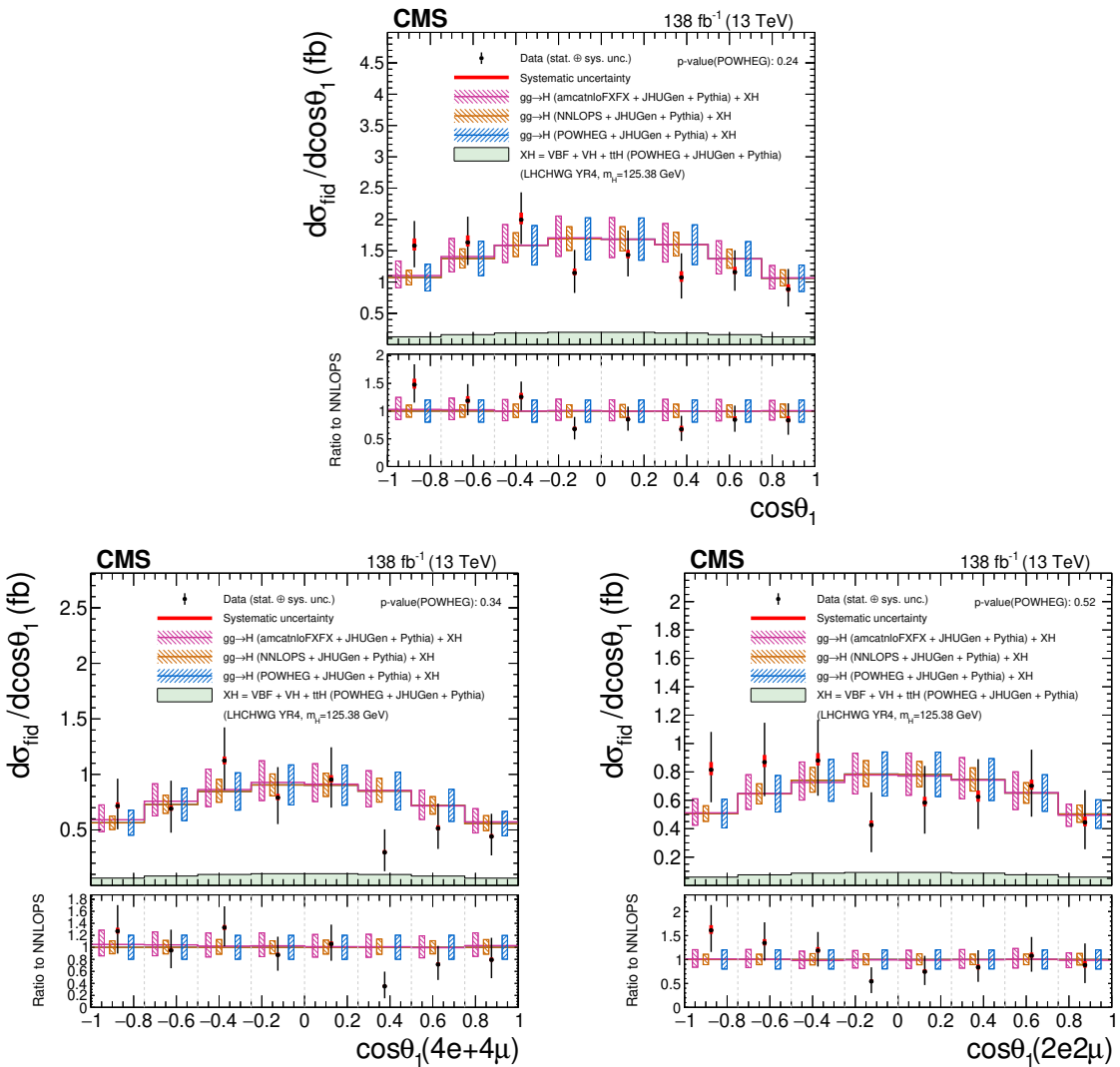


Figure 14. Differential cross sections as functions of $\cos \theta_1$ in the 4ℓ (upper) and in the same-flavor (lower left) and different-flavor (lower right) final states. The acceptance and theoretical uncertainties in the differential bins are calculated using the ggH predictions from three different generators normalized to next-to-next-to-next-to-leading order (N^3LO) [34]. The subdominant component of the signal ($VBF + VH + t\bar{t}H$) is denoted as XH and is fixed to the SM prediction. The measured cross sections are compared with the ggH predictions from POWHEG (blue), NNLOPS (orange), and MADGRAPH5_aMC@NLO (pink). The hatched areas correspond to the systematic uncertainties in the theoretical predictions. Black points represent the measured fiducial cross sections in each bin, black error bars the total uncertainty in each measurement, red boxes the systematic uncertainties. The lower panels display the ratios of the measured cross sections and of the predictions from POWHEG and MADGRAPH5_aMC@NLO to the NNLOPS theoretical predictions.

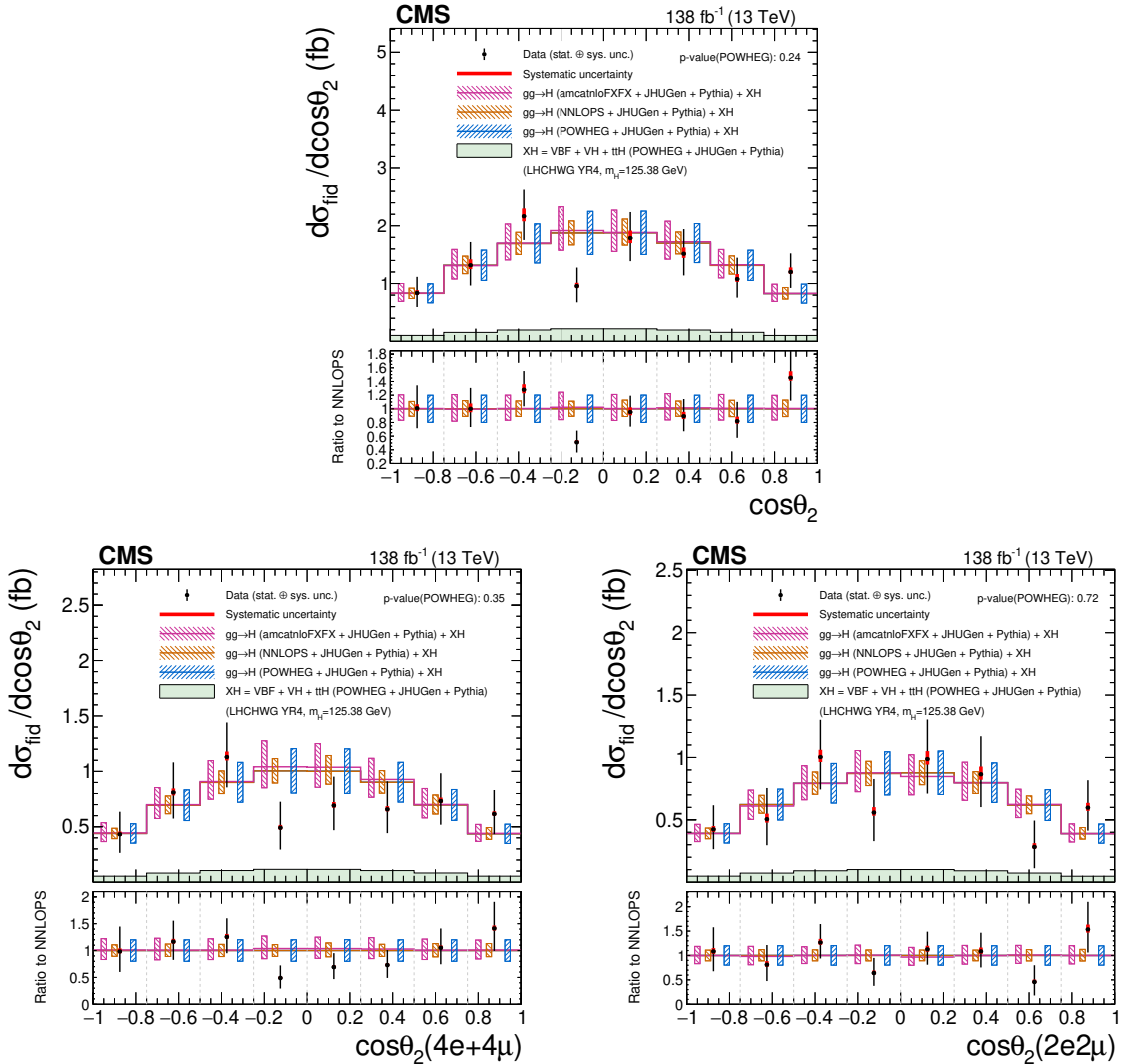


Figure 15. Differential cross sections as functions of $\cos\theta_2$ in the 4ℓ (upper) and in the same-flavor (lower left) and different-flavor (lower right) final states. The acceptance and theoretical uncertainties in the differential bins are calculated using the ggH predictions from three different generators normalized to next-to-next-to-next-to-leading order ($N^3\text{LO}$) [34]. The subdominant component of the signal (VBF + VH + $t\bar{t}H$) is denoted as XH and is fixed to the SM prediction. The measured cross sections are compared with the ggH predictions from POWHEG (blue), NNLOPS (orange), and MADGRAPH5_aMC@NLO (pink). The hatched areas correspond to the systematic uncertainties in the theoretical predictions. Black points represent the measured fiducial cross sections in each bin, black error bars the total uncertainty in each measurement, red boxes the systematic uncertainties. The lower panels display the ratios of the measured cross sections and of the predictions from POWHEG and MADGRAPH5_aMC@NLO to the NNLOPS theoretical predictions.

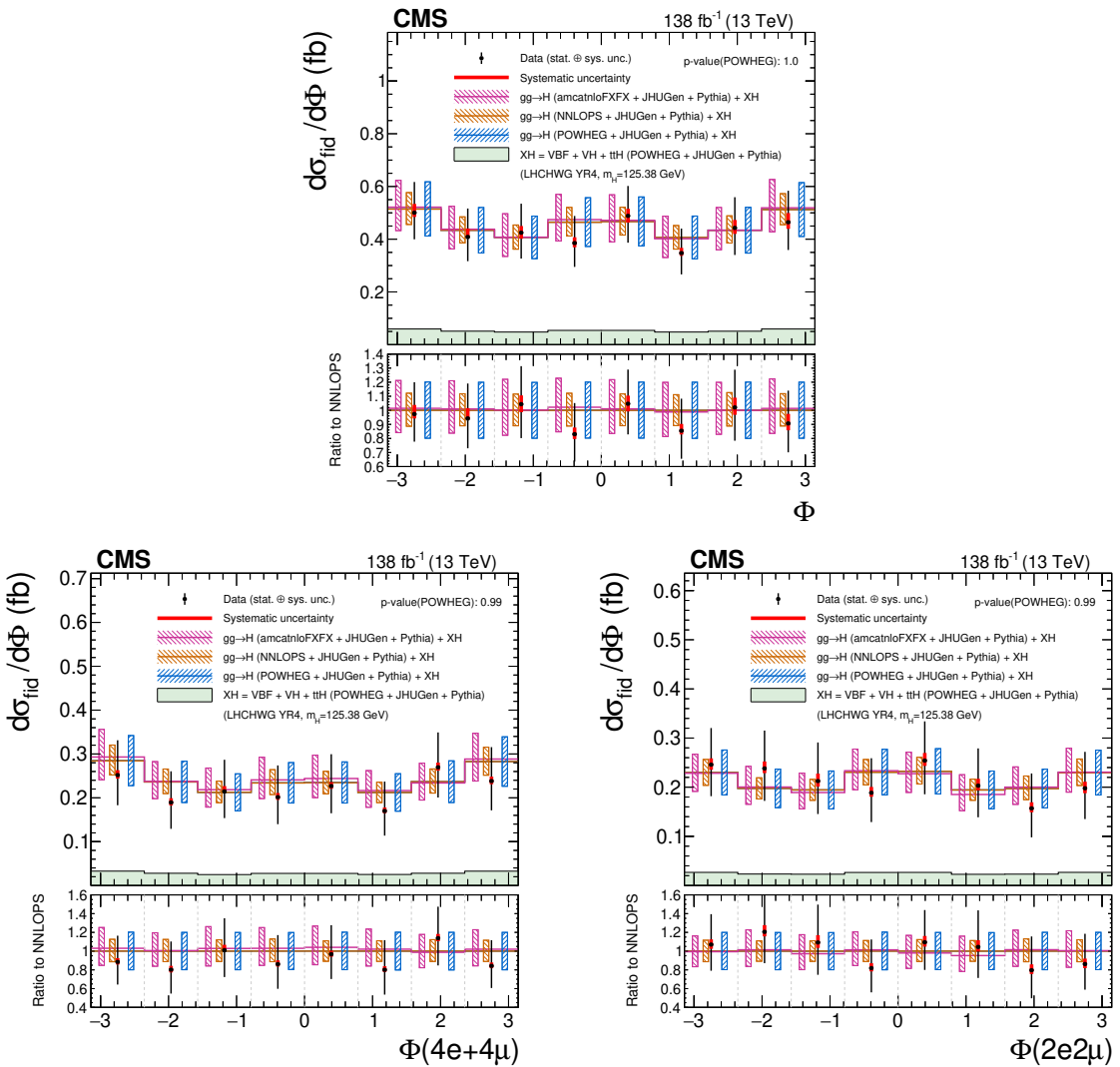


Figure 16. Differential cross sections as functions of the Φ angle in the 4ℓ (upper) and in the same-flavor (lower left) and different-flavor (lower right) final states. The acceptance and theoretical uncertainties in the differential bins are calculated using the ggH predictions from three different generators normalized to next-to-next-to-next-to-leading order ($N^3\text{LO}$) [34]. The subdominant component of the signal ($VBF + VH + t\bar{t}H$) is denoted as XH and is fixed to the SM prediction. The measured cross sections are compared with the ggH predictions from POWHEG (blue), NNLOPS (orange), and MADGRAPH5_aMC@NLO (pink). The hatched areas correspond to the systematic uncertainties in the theoretical predictions. Black points represent the measured fiducial cross sections in each bin, black error bars the total uncertainty in each measurement, red boxes the systematic uncertainties. The lower panels display the ratios of the measured cross sections and of the predictions from POWHEG and MADGRAPH5_aMC@NLO to the NNLOPS theoretical predictions.

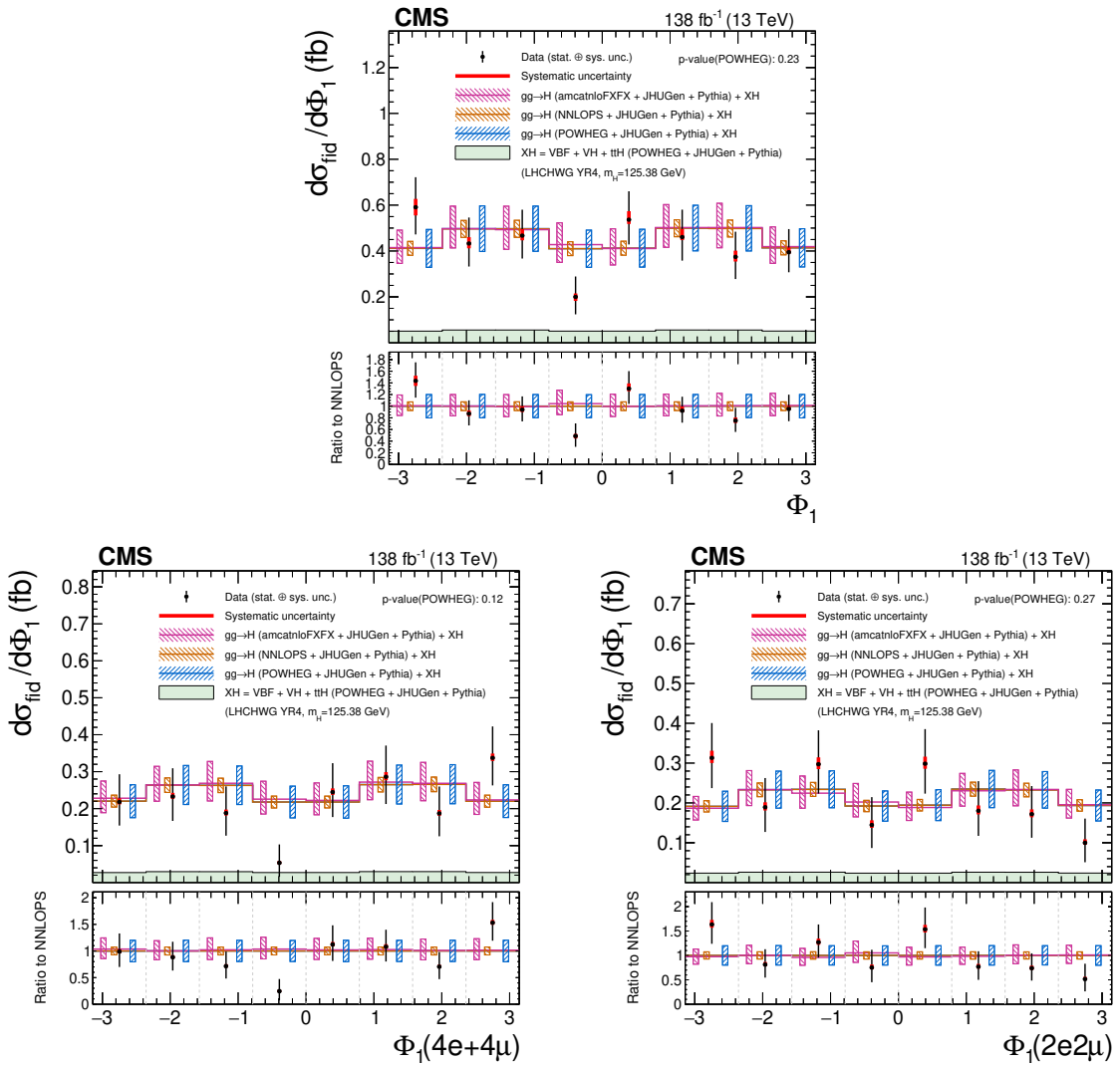


Figure 17. Differential cross sections as functions of the Φ_1 angle in the 4ℓ (upper) and in the same-flavor (lower left) and different-flavor (lower right) final states. The acceptance and theoretical uncertainties in the differential bins are calculated using the ggH predictions from three different generators normalized to next-to-next-to-next-to-leading order ($N^3\text{LO}$) [34]. The subdominant component of the signal ($\text{VBF} + \text{VH} + \text{t}\bar{\text{t}}\text{H}$) is denoted as XH and is fixed to the SM prediction. The measured cross sections are compared with the ggH predictions from POWHEG (blue), NNLOPS (orange), and MADGRAPH5_aMC@NLO (pink). The hatched areas correspond to the systematic uncertainties in the theoretical predictions. Black points represent the measured fiducial cross sections in each bin, black error bars the total uncertainty in each measurement, red boxes the systematic uncertainties. The lower panels display the ratios of the measured cross sections and of the predictions from POWHEG and MADGRAPH5_aMC@NLO to the NNLOPS theoretical predictions.

These observables can be used to compute matrix element discriminants sensitive to the presence of possible BSM physics effects as described in section 6.1 and ref. [31].

Cross sections are measured in differential bins of six kinematic discriminants sensitive to various HVV anomalous couplings and the interference between two model contributions (SM and a BSM scenario): $\mathcal{D}_{0^-}^{\text{dec}}$, $\mathcal{D}_{0h+}^{\text{dec}}$, $\mathcal{D}_{\text{CP}}^{\text{dec}}$, $\mathcal{D}_{\text{int}}^{\text{dec}}$, $\mathcal{D}_{\Lambda 1}^{\text{dec}}$, and $\mathcal{D}_{\Lambda 1}^{Z\gamma,\text{dec}}$. The results of these measurements, shown in figures 18–23, are compared to distributions for the matrix element discriminants corresponding to various anomalous coupling hypotheses. Following the conventions adopted in ref. [31], rather than using the value of the coupling to identify the type of the anomalous coupling sample, the cross sections fractions f_{ai} are used:

$$f_{ai} = \frac{|a_i|^2 \sigma_i}{\sum_j |a_j|^2 \sigma_j} \text{sign}\left(\frac{a_i}{a_1}\right), \quad (10.2)$$

where σ_i is the cross section for the process corresponding to $a_i = 1, a_{j \neq i} = 0$ in eq. (6.5). The term for Λ_1 is $\tilde{\sigma}_{\Lambda 1}/(\Lambda_1)^4$ instead of $|a_i|^2 \sigma_i$, where $\tilde{\sigma}_{\Lambda 1}$ is the effective cross section for the process corresponding to $\Lambda_1 = 1 \text{ TeV}$, given in units of $\text{fb} \cdot \text{TeV}^4$. To study the a_2 and a_3 couplings, discriminants of the form \mathcal{D}_{alt} and \mathcal{D}_{int} are built. The former are compared to the distributions obtained for pure anomalous coupling scenarios corresponding to $f_{a3} = 1$ and $f_{a2} = 1$, while the latter are compared to the interference scenario where $f_{a3} = 0.5$ and $f_{a2} = 0.5$. A value of $f_{ai} = 0.5$ corresponds to a maximal mixing between the SM and the BSM scenarios. To inspect the couplings κ_1 and $\kappa_2^{Z\gamma}$, the interference discriminant is not built since it does not provide additional information and the corresponding \mathcal{D}_{alt} can also be used to study the interference. For this reason, the measurements of $\mathcal{D}_{\Lambda 1}^{\text{dec}}$ and $\mathcal{D}_{\Lambda 1}^{Z\gamma,\text{dec}}$ are compared to the pure anomalous couplings scenario $f_{\Lambda 1} = 1$ and $f_{\Lambda 1}^{Z\gamma} = 1$, as well as to the interference hypotheses $f_{\Lambda 1} = 0.5$ and $f_{\Lambda 1}^{Z\gamma} = 0.5$. These values of f_{ai} , $f_{\Lambda 1}^{Z\gamma}$, and $f_{\Lambda 1}$ correspond to illustrative extreme scenarios chosen for a qualitative representation of the corresponding kinematic discriminants. The best constraints on these parameters are much stricter, as reported in ref. [31]

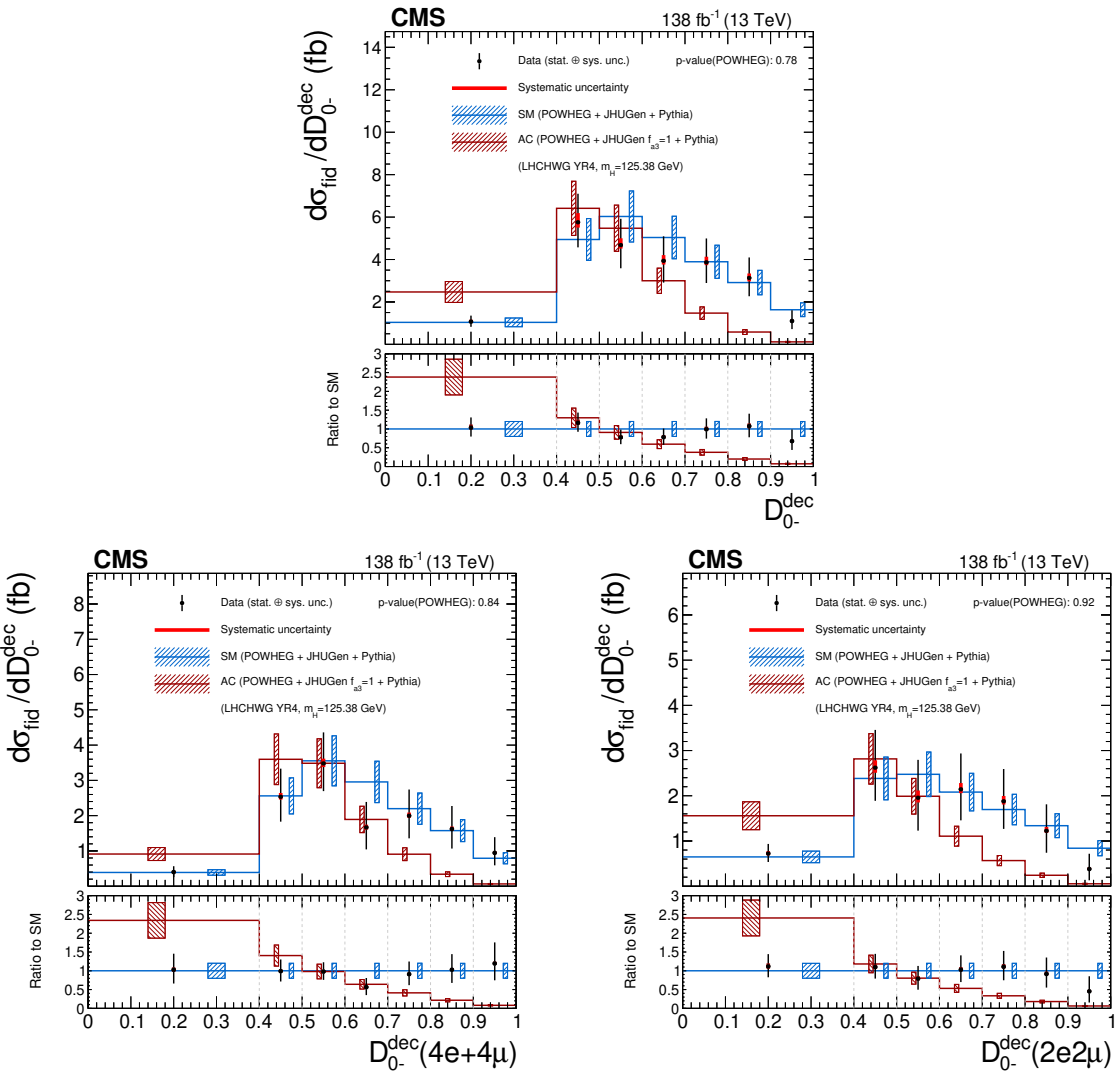


Figure 18. Differential cross sections as functions of the matrix element kinematic discriminant $D_{0^-}^{dec}$ in the 4ℓ (upper) and in the same-flavor (lower left) and different-flavor (lower right) final states. The brown histograms show the distribution of the matrix element discriminant for the HVV anomalous coupling scenario corresponding to $f_{a3} = 1$. The subdominant component of the signal (VBF+VH+ $t\bar{t}H$) is fixed to the SM prediction. The hatched areas correspond to the systematic uncertainties in the theoretical predictions. Black points represent the measured fiducial cross sections in each bin, black error bars the total uncertainty in each measurement, red boxes the systematic uncertainties. The lower panels display the ratios of the measured cross sections and of the predictions from POWHEG and MADGRAPH5_amc@NLO to the NNLOPS theoretical predictions.

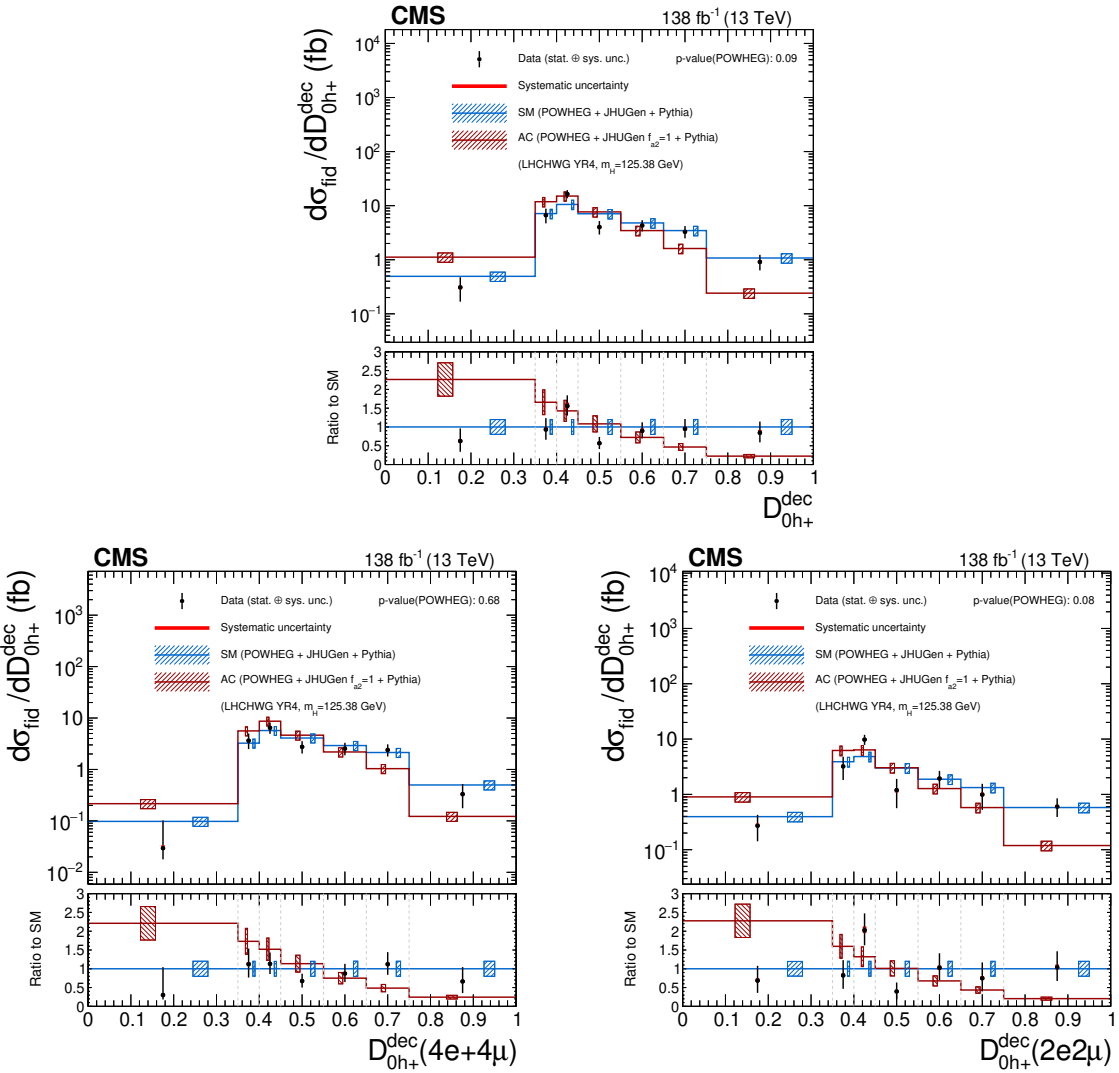


Figure 19. Differential cross sections as functions of the matrix element kinematic discriminant D_{0h+}^{dec} in the 4ℓ (upper) and in the same-flavor (lower left) and different-flavor (lower right) final states. The brown histograms show the distribution of the matrix element discriminant for the HVV anomalous coupling scenario corresponding to $f_{a2} = 1$. The subdominant component of the signal (VBF + VH + $t\bar{t}H$) is fixed to the SM prediction. The hatched areas correspond to the systematic uncertainties in the theoretical predictions. Black points represent the measured fiducial cross sections in each bin, black error bars the total uncertainty in each measurement, red boxes the systematic uncertainties. The lower panels display the ratios of the measured cross sections and of the predictions from POWHEG and MADGRAPH5_amc@NLO to the NNLOPS theoretical predictions.

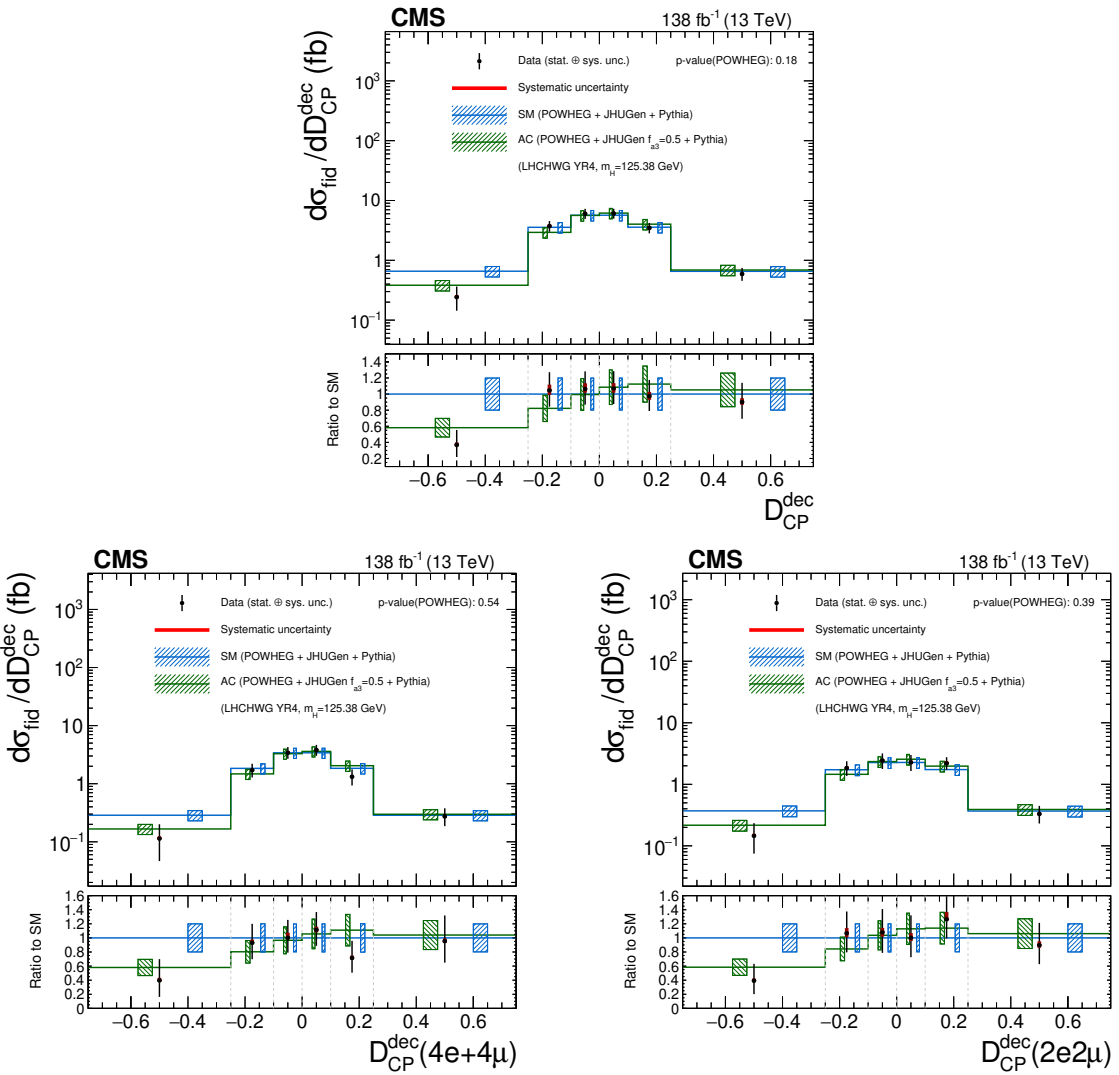


Figure 20. Differential cross sections as functions of the matrix element kinematic discriminant D_{CP}^{dec} in the 4ℓ (upper) and in the same-flavor (lower left) and different-flavor (lower right) final states. The green histogram shows the distribution of the discriminant for the HVV anomalous coupling scenario corresponding to $f_{a3} = 0.5$. The subdominant component of the signal (VBF + VH + $t\bar{t}H$) is fixed to the SM prediction. The hatched areas correspond to the systematic uncertainties in the theoretical predictions. Black points represent the measured fiducial cross sections in each bin, black error bars the total uncertainty in each measurement, red boxes the systematic uncertainties. The lower panels display the ratios of the measured cross sections and of the predictions from POWHEG and MADGRAPH5_amc@NLO to the NNLOPS theoretical predictions.

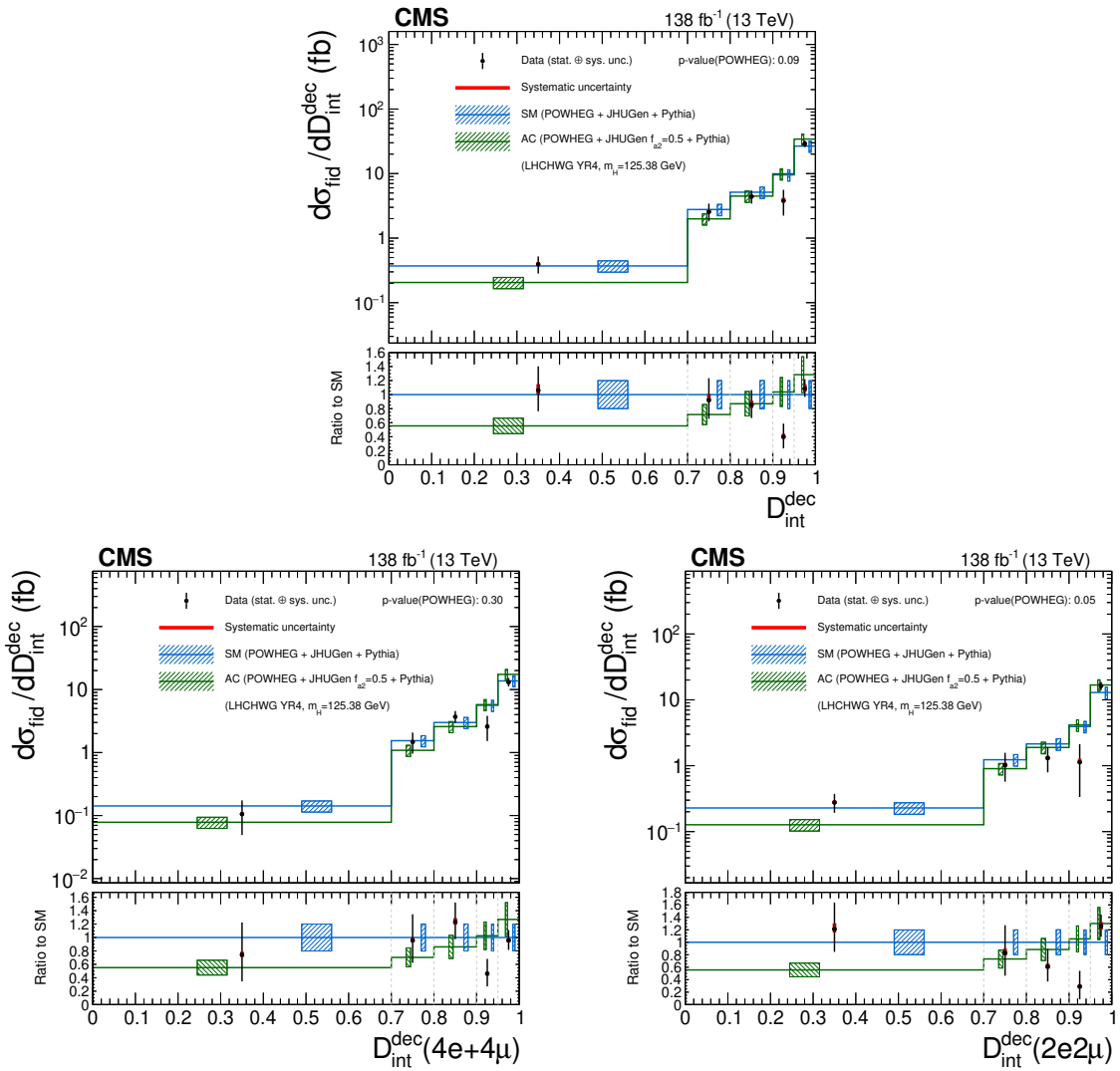


Figure 21. Differential cross sections as functions of the matrix element kinematic discriminant $D_{\text{int}}^{\text{dec}}$ in the 4ℓ (upper) and in the same-flavor (lower left) and different-flavor (lower right) final states. The green histogram shows the distribution of the discriminant for the HVV anomalous coupling scenario corresponding to $f_{a2} = 0.5$. The subdominant component of the signal ($\text{VBF} + \text{VH} + t\bar{t}\text{H}$) is fixed to the SM prediction. The hatched areas correspond to the systematic uncertainties in the theoretical predictions. Black points represent the measured fiducial cross sections in each bin, black error bars the total uncertainty in each measurement, red boxes the systematic uncertainties. The lower panels display the ratios of the measured cross sections and of the predictions from POWHEG and MADGRAPH5_amc@NLO to the NNLOPS theoretical predictions.

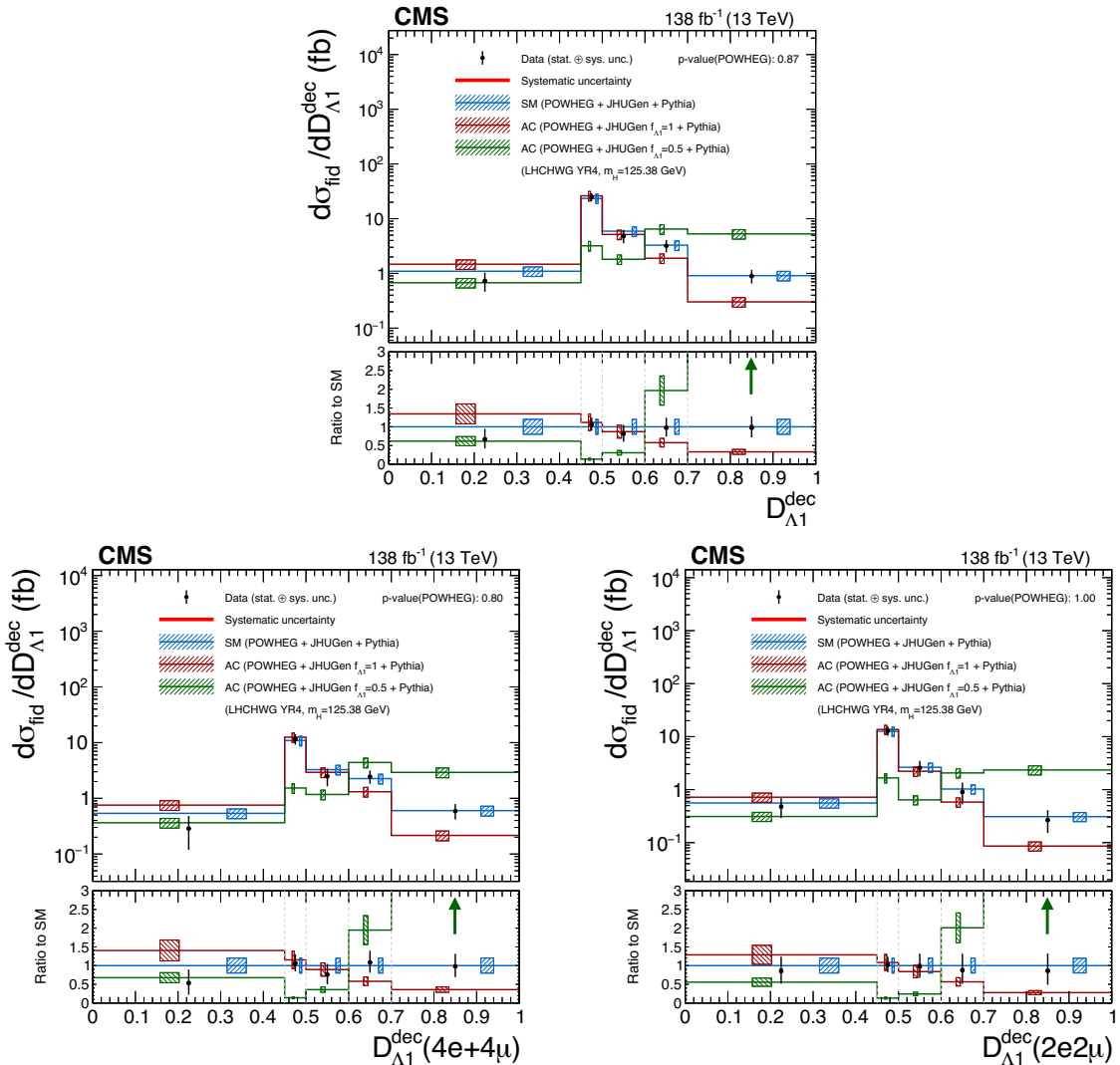


Figure 22. Differential cross sections as functions of the matrix element kinematic discriminant $D_{\Lambda 1}^{\text{dec}}$ in the 4ℓ (upper) and in the same-flavor (lower left) and different-flavor (lower right) final states. The brown and green histograms show the distributions of the discriminant for the HVV anomalous coupling scenarios corresponding to $f_{\Lambda 1} = 1$ and $f_{\Lambda 1} = 0.5$. The subdominant component of the signal ($\text{VBF} + \text{VH} + t\bar{t}\text{H}$) is fixed to the SM prediction. The hatched areas correspond to the systematic uncertainties in the theoretical predictions. Black points represent the measured fiducial cross sections in each bin, black error bars the total uncertainty in each measurement, red boxes the systematic uncertainties. The lower panels display the ratio of the measured cross section and of the predictions from POWHEG and MADGRAPH5_aMC@NLO to the NNLOPS theoretical expectation.

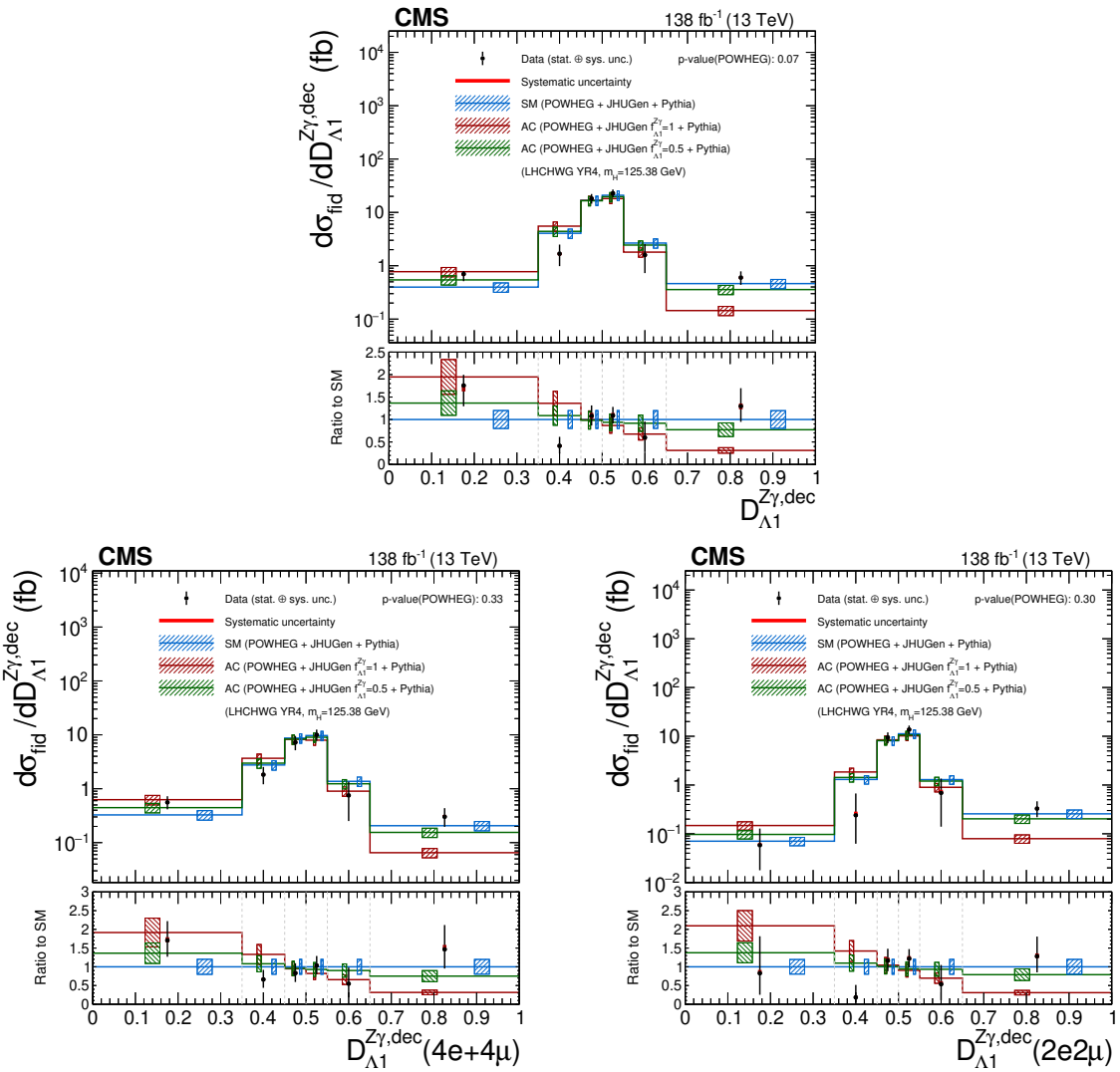


Figure 23. Differential cross sections as functions of the matrix element kinematic discriminant $D_{\Lambda1}^{Z\gamma,dec}$ in the 4ℓ (upper) and in the same-flavor (lower left) and different-flavor (lower right) final states. The brown and green histograms show the distributions of the discriminant for the HVV anomalous coupling scenarios corresponding to $f_{\Lambda1}^{Z\gamma} = 1$ and $f_{\Lambda1}^{Z\gamma} = 0.5$. The subdominant component of the signal (VBF + VH + t \bar{t} H) is fixed to the SM prediction. The hatched areas correspond to the systematic uncertainties in the theoretical predictions. Black points represent the measured fiducial cross sections in each bin, black error bars the total uncertainty in each measurement, red boxes the systematic uncertainties. The lower panels display the ratios of the measured cross sections and of the predictions from POWHEG and MADGRAPH5_aMC@NLO to the NNLOPS theoretical predictions.

10.4 Double-differential cross sections

The differential cross section measurements presented so far ensure a good coverage of the production and decay phase spaces in the $H \rightarrow ZZ \rightarrow 4\ell$ channel, together with a separation of possible interference effects present in the same- and different-flavor final states. To

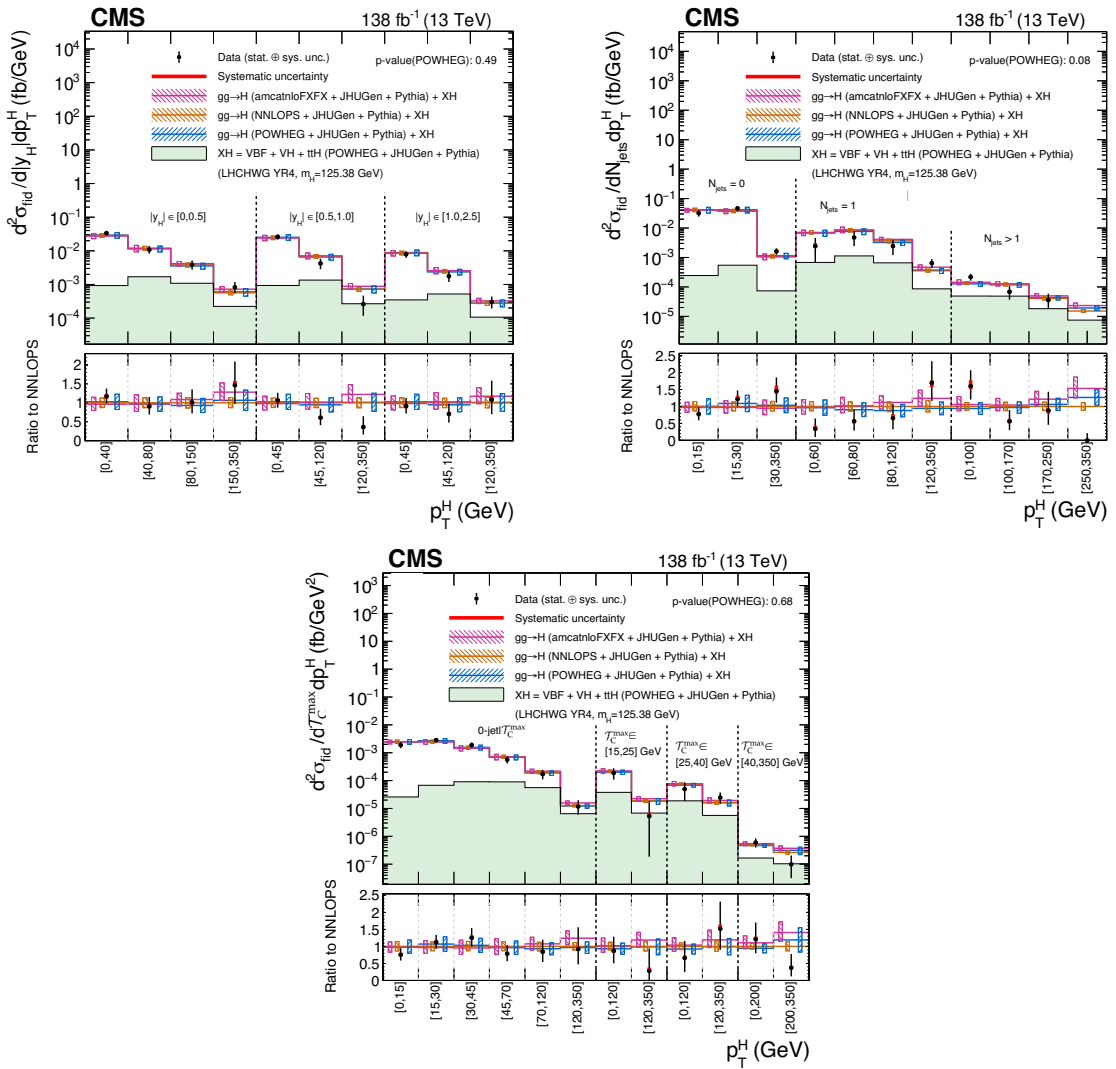


Figure 24. Double differential cross sections in bins of $|y_H|$ vs. p_T^H (upper left), number of associated jets vs. p_T^H (upper right), and T_C^{\max} vs. p_T^H (lower). The binnings of the various measurements are reported in table 6. The content of each plot is described in the caption of figure 6.

improve the characterization of this decay channel and to maximize the coverage and separation of the different phase space regions, a set of double-differential measurements is also performed. The results are shown in figure 24 for $|y_H|$ vs. p_T^H (upper left), the number of associated jets vs. p_T^H (upper right), and T_C^{\max} vs. p_T^H (lower) and in figure 25 for p_T^{Hj} vs. p_T^H (upper left), m_{Z_1} vs. m_{Z_2} (upper right), and p_T of the leading vs. subleading jet (lower). The results are consistent with the SM expectations, with the largest difference observed in the p_T^H bins in the $N_{\text{jets}} = 1$ phase space region. The deficit in the low- p_T^H bins for $N_{\text{jets}} = 1$ is explained by large correlations with the high- p_T^H bin of $N_{\text{jets}} = 1$ and the first p_T^H bin in the $N_{\text{jets}} > 1$ phase space regions, where the fit to the data shows an excess with respect to the SM prediction.

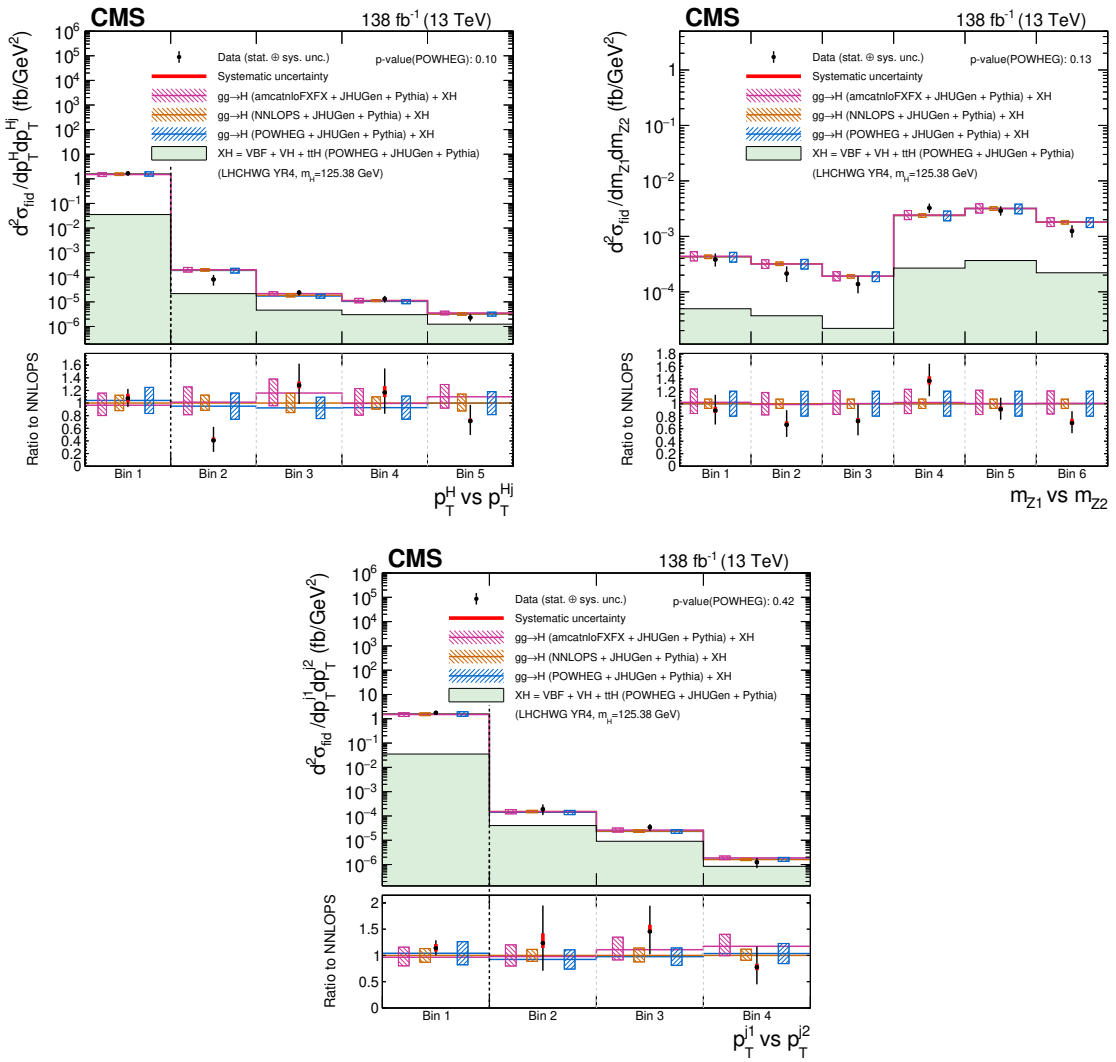


Figure 25. Double differential cross sections in bins of p_T^H vs. p_T^{Hj} (upper left), m_{Z_1} vs. m_{Z_2} (upper right), and p_T of the leading vs. subleading jet (lower). The binnings of the various measurements are reported in table 6. The content of each plot is described in the caption of figure 6.

11 Interpretations

11.1 Constraints on the H boson self-coupling

The differential cross section for the H boson production as a function of p_T^H can be used to extract limits on the H boson self-coupling, following the approach described in refs. [137–139]. At NLO in pQCD the H boson production includes processes sensitive to the trilinear self-coupling (λ_3). The production modes $t\bar{t}H$ and VH introduce sizeable contributions to the H boson self-coupling due to the large vector boson and the top quark masses, whereas ggH and VBF production lead to much smaller contributions to the loop correction and are therefore less sensitive to possible modifications of λ_3 .

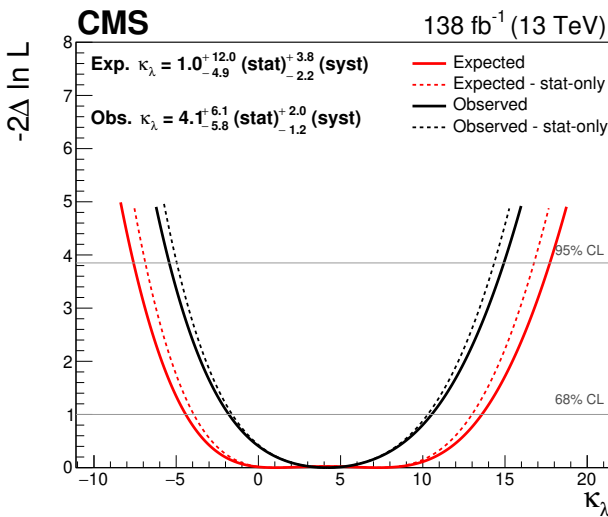


Figure 26. Likelihood scan as a function of κ_λ . The scan is shown with (solid line) and without (dashed line) systematic uncertainties profiled in the fit.

The cross sections for the various production mechanisms of the H boson are parametrized as functions of a coupling modifier $\kappa_\lambda = \lambda_3/\lambda_3^{\text{SM}}$ in order to account for NLO terms arising from the H boson trilinear self-coupling. The signal model defined in section 8 is modified by fixing the cross sections and branching fractions to their SM expectation values and by introducing scaling functions $\mu_{i,j}(\kappa_\lambda)$ in each bin i of p_T^H , for each production mechanism j . The dominant production mechanism is ggH, for which a differential parametrization of the cross section as a function of κ_λ is not available yet, as discussed in refs. [137–139]. The inclusive value is used for the parametrization of the H boson cross section for this production mechanism, taking into account an inclusive $\mathcal{O}(\lambda_3)$ correction factor.

In order to compute the scaling functions $\mu_{i,j}(\kappa_\lambda)$ for the other production modes, LO parton-level events are generated using MADGRAPH5_aMC@NLO 2.5.5 and are reweighted on an event-by-event basis using a dedicated EW reweighting tool, which computes the corresponding NLO λ_3 -corrections ($\mathcal{O}(\lambda_3)$). The ratio of the $\mathcal{O}(\lambda_3)$ to the LO distributions in bins of p_T^H is used to derive the scaling functions $\mu_{i,j}(\kappa_\lambda)$ as detailed in ref. [138].

Constraints on κ_λ are extracted from the maximum likelihood scan in the range $-10 < \kappa_\lambda < 20$, outside which the model is no longer valid as NLO effects start to dominate, while the other H couplings are fixed to their SM value. The likelihood scan as a function of κ_λ is shown in figure 26.

The minimum of the negative log-likelihood ratio corresponds to a measured value of:

$$\kappa_\lambda = 4.1^{+6.4}_{-5.9} = 4.1^{+6.1}_{-5.8} (\text{stat})^{+2.0}_{-1.2} (\text{syst}) \quad (11.1)$$

for an expected value of:

$$\kappa_\lambda = 1.0^{+12.6}_{-5.4} = 1.0^{+12.0}_{-4.9} (\text{stat})^{+3.8}_{-2.2} (\text{syst}). \quad (11.2)$$

The corresponding observed (expected) excluded κ_λ range at the 95% confidence level (CL) is:

$$-5.4(-7.6) < \kappa_\lambda < 14.9(17.7).$$

The current best available constraints on κ_λ are obtained from the combination of measurements of H boson pair production performed with the Run 2 data-set. The limits set by the ATLAS and CMS Collaborations correspond to observed limits at the 95 % CL of $-0.6 < \kappa_\lambda < 6.6$ [140] and $-1.24 < \kappa_\lambda < 6.49$ [44], respectively.

11.2 Constraints on the charm and bottom quark couplings

The p_T^H differential cross section of the ggH production mechanism is used to set constraints on the H boson coupling modifiers to b and c quarks in the context of the κ -framework [141]. In fact, because of the presence of b and c quarks in the ggH loop [142], anomalous values of these couplings can result in modifications of the ggH cross section. The other production mechanisms are set to their SM expectation and no dependence from these couplings is assumed. The H boson coupling to the top quark is fixed to the SM value. The effects of the associated production with b quarks, whose contribution increases with increasing values of the coupling of the H boson to the b quark, are taken into account in the theoretical inputs to compute the parametrization.

The results are extracted from a maximum likelihood fit where the approach described in section 8 is modified by separating the ggH production from the other mechanisms, which are considered as background and constrained to the SM predictions with their respective uncertainties. The combined effect of the H boson couplings to b (κ_b) and c quarks (κ_c) is modeled independently in each bin of the p_T^H spectrum by means of a quadratic polynomial, following the strategy of ref. [52].

Figure 27 (left) shows the 2D likelihood scan of κ_b and κ_c under the assumption that the $H \rightarrow ZZ$ branching fraction is dependent on the H boson couplings $\mathcal{B} = \mathcal{B}(\kappa_b, \kappa_c)$, with all the other couplings fixed to their SM value, and assuming no beyond-the-SM contributions. As expected, the result is constrained by the saturation of the total width.

A simultaneous constraint on κ_b and κ_c is also derived by treating the $H \rightarrow ZZ$ branching fraction as an unconstrained parameter in the fit. The constraint from the total width and the overall normalization is removed in this way, and what remains is purely the constraint obtained from the shape of the p_T^H spectrum. The result is shown in figure 27 (right).

Confidence intervals on κ_b and κ_c are obtained from a maximum likelihood fit leaving one of the two parameters unconstrained in the fit and scanning the other. The observed (expected) exclusion limits at the 95% CL are:

$$\begin{aligned} -1.1(-1.3) &< \kappa_b < 1.1(1.2) \\ -5.3(-5.7) &< \kappa_c < 5.2(5.7), \end{aligned} \tag{11.3}$$

assuming a dependence of the branching fraction on κ_b and κ_c , and:

$$\begin{aligned} -5.6(-5.5) &< \kappa_b < 8.9(7.4) \\ -20(-19) &< \kappa_c < 23(20), \end{aligned} \tag{11.4}$$

treating the branching fraction as an unconstrained parameter in the fit.

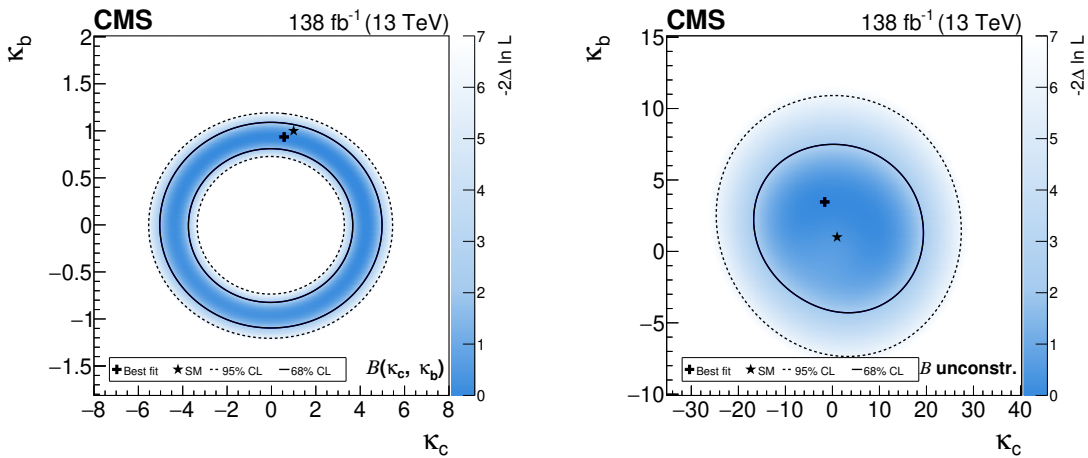


Figure 27. Simultaneous fit of κ_b and κ_c , assuming a coupling dependence of the branching fraction (left) and treating it as an unconstrained parameter in the fit (right).

12 Summary

This paper presents a comprehensive characterization of the $H \rightarrow ZZ \rightarrow 4\ell$ decay channel via the measurement of fiducial differential cross sections as functions of several kinematic observables. The H boson production is characterized via measurements of differential cross sections in bins of p_T^H and $|y_H|$, the p_T of the leading and subleading jets and observables of the dijet system, when associated with jets. Fiducial cross sections are measured in bins of the seven kinematic observables that completely define the four-lepton decay: the invariant mass of the two Z bosons and the five angles that describe the fermions kinematical properties and the production and decay planes. Differential cross sections are also measured in bins of six matrix element kinematic discriminants sensitive to various anomalous couplings of the H boson to vector bosons. The dynamical evolution of the renormalization and factorization scales, and resummation effects are probed by measuring cross sections in bins of rapidity-weighted jet vetoes, and in bins of observables of the H plus jets system. An extensive set of double-differential measurements is presented, providing a complete coverage of the phase space under study. The $H \rightarrow ZZ \rightarrow 4\ell$ inclusive fiducial cross section is $\sigma_{fid} = 2.73 \pm 0.26 \text{ fb} = 2.73 \pm 0.22 \text{ (stat)} \pm 0.15 \text{ (syst)} \text{ fb}$, in agreement with the SM expectation of $2.86 \pm 0.15 \text{ fb}$. The measurement of the fiducial cross section in differential bins of p_T^H is used to set constraints on the trilinear self-coupling of the H boson, with an observed (expected) limit of $-5.4 (-7.6) < \kappa_\lambda < 14.9 (17.7)$ at the 95% CL. Finally, constraints on the modifiers of H boson couplings to b and c quarks (κ_b and κ_c) are also determined with an observed (expected) limit of $-1.1 (-1.3) < \kappa_b < 1.1 (1.2)$ and $-5.3 (-5.7) < \kappa_c < 5.2 (5.7)$ at the 95% CL, obtained assuming a dependence of the branching fraction on κ_b and κ_c . All results are consistent with the SM predictions for the $H \rightarrow ZZ \rightarrow 4\ell$ decay channel in the considered fiducial phase space.

Acknowledgments

We congratulate our colleagues in the CERN accelerator departments for the excellent performance of the LHC and thank the technical and administrative staffs at CERN and at other CMS institutes for their contributions to the success of the CMS effort. In addition, we gratefully acknowledge the computing centres and personnel of the Worldwide LHC Computing Grid and other centres for delivering so effectively the computing infrastructure essential to our analyses. Finally, we acknowledge the enduring support for the construction and operation of the LHC, the CMS detector, and the supporting computing infrastructure provided by the following funding agencies: BMBWF and FWF (Austria); FNRS and FWO (Belgium); CNPq, CAPES, FAPERJ, FAPERGS, and FAPESP (Brazil); MES and BNSF (Bulgaria); CERN; CAS, MoST, and NSFC (China); MINCIENCIAS (Colombia); MSES and CSF (Croatia); RIF (Cyprus); SENESCYT (Ecuador); MoER, ERC PUT and ERDF (Estonia); Academy of Finland, MEC, and HIP (Finland); CEA and CNRS/IN2P3 (France); BMBF, DFG, and HGF (Germany); GSRI (Greece); NKFIH (Hungary); DAE and DST (India); IPM (Iran); SFI (Ireland); INFN (Italy); MSIP and NRF (Republic of Korea); MES (Latvia); LAS (Lithuania); MOE and UM (Malaysia); BUAP, CINVESTAV, CONACYT, LNS, SEP, and UASLP-FAI (Mexico); MOS (Montenegro); MBIE (New Zealand); PAEC (Pakistan); MES and NSC (Poland); FCT (Portugal); MESTD (Serbia); MCIN/AEI and PCTI (Spain); MOSTR (Sri Lanka); Swiss Funding Agencies (Switzerland); MST (Taipei); MHESI and NSTDA (Thailand); TUBITAK and TENMAK (Turkey); NASU (Ukraine); STFC (United Kingdom); DOE and NSF (U.S.A.).

Individuals have received support from the Marie-Curie programme and the European Research Council and Horizon 2020 Grant, contract Nos. 675440, 724704, 752730, 758316, 765710, 824093, 884104, and COST Action CA16108 (European Union); the Levantis Foundation; the Alfred P. Sloan Foundation; the Alexander von Humboldt Foundation; the Belgian Federal Science Policy Office; the Fonds pour la Formation à la Recherche dans l’Industrie et dans l’Agriculture (FRIA-Belgium); the Agentschap voor Innovatie door Wetenschap en Technologie (IWT-Belgium); the F.R.S.-FNRS and FWO (Belgium) under the “Excellence of Science — EOS” — be.h project n. 30820817; the Beijing Municipal Science & Technology Commission, No. Z191100007219010 and Fundamental Research Funds for the Central Universities (China); the Ministry of Education, Youth and Sports (MEYS) of the Czech Republic; the Hellenic Foundation for Research and Innovation (HFRI), Project Number 2288 (Greece); the Deutsche Forschungsgemeinschaft (DFG), under Germany’s Excellence Strategy — EXC 2121 “Quantum Universe” — 390833306, and under project number 400140256 — GRK2497; the Hungarian Academy of Sciences, the New National Excellence Program — ÚNKP, the NKFIH research grants K 124845, K 124850, K 128713, K 128786, K 129058, K 131991, K 133046, K 138136, K 143460, K 143477, 2020-2.2.1-ED-2021-00181, and TKP2021-NKTA-64 (Hungary); the Council of Science and Industrial Research, India; the Latvian Council of Science; the Ministry of Education and Science, project no. 2022/WK/14, and the National Science Center, contracts Opus 2021/41/B/ST2/01369 and 2021/43/B/ST2/01552 (Poland); the Fundação para a Ciência e a Tecnologia, grant CEECIND/01334/2018 (Portugal); the National Priorities

Research Program by Qatar National Research Fund; MCIN/AEI/10.13039/501100011033, ERDF “a way of making Europe”, and the Programa Estatal de Fomento de la Investigación Científica y Técnica de Excelencia María de Maeztu, grant MDM-2017-0765 and Programa Severo Ochoa del Principado de Asturias (Spain); the Chulalongkorn Academic into Its 2nd Century Project Advancement Project, and the National Science, Research and Innovation Fund via the Program Management Unit for Human Resources & Institutional Development, Research and Innovation, grant B05F650021 (Thailand); the Kavli Foundation; the Nvidia Corporation; the SuperMicro Corporation; the Welch Foundation, contract C-1845; and the Weston Havens Foundation (U.S.A.).

Open Access. This article is distributed under the terms of the Creative Commons Attribution License ([CC-BY 4.0](#)), which permits any use, distribution and reproduction in any medium, provided the original author(s) and source are credited.

References

- [1] ATLAS collaboration, *Observation of a new particle in the search for the Standard Model Higgs boson with the ATLAS detector at the LHC*, *Phys. Lett. B* **716** (2012) 1 [[arXiv:1207.7214](#)] [[INSPIRE](#)].
- [2] CMS collaboration, *Observation of a new boson at a mass of 125 GeV with the CMS experiment at the LHC*, *Phys. Lett. B* **716** (2012) 30 [[arXiv:1207.7235](#)] [[INSPIRE](#)].
- [3] CMS collaboration, *Observation of a new boson with mass near 125 GeV in pp collisions at $\sqrt{s} = 7$ and 8 TeV*, *JHEP* **06** (2013) 081 [[arXiv:1303.4571](#)] [[INSPIRE](#)].
- [4] F. Englert and R. Brout, *Broken symmetry and the mass of gauge vector mesons*, *Phys. Rev. Lett.* **13** (1964) 321 [[INSPIRE](#)].
- [5] P.W. Higgs, *Broken symmetries, massless particles and gauge fields*, *Phys. Lett.* **12** (1964) 132 [[INSPIRE](#)].
- [6] P.W. Higgs, *Broken symmetries and the masses of gauge bosons*, *Phys. Rev. Lett.* **13** (1964) 508 [[INSPIRE](#)].
- [7] G.S. Guralnik, C.R. Hagen and T.W.B. Kibble, *Global conservation laws and massless particles*, *Phys. Rev. Lett.* **13** (1964) 585 [[INSPIRE](#)].
- [8] P.W. Higgs, *Spontaneous symmetry breakdown without massless bosons*, *Phys. Rev.* **145** (1966) 1156 [[INSPIRE](#)].
- [9] T.W.B. Kibble, *Symmetry breaking in non-Abelian gauge theories*, *Phys. Rev.* **155** (1967) 1554 [[INSPIRE](#)].
- [10] ATLAS collaboration, *Measurements of the Higgs boson production and decay rates and coupling strengths using pp collision data at $\sqrt{s} = 7$ and 8 TeV in the ATLAS experiment*, *Eur. Phys. J. C* **76** (2016) 6 [[arXiv:1507.04548](#)] [[INSPIRE](#)].
- [11] CMS collaboration, *Precise determination of the mass of the Higgs boson and tests of compatibility of its couplings with the Standard Model predictions using proton collisions at 7 and 8 TeV*, *Eur. Phys. J. C* **75** (2015) 212 [[arXiv:1412.8662](#)] [[INSPIRE](#)].

- [12] ATLAS and CMS collaborations, *Combined measurement of the Higgs boson mass in pp collisions at $\sqrt{s} = 7$ and 8 TeV with the ATLAS and CMS experiments*, *Phys. Rev. Lett.* **114** (2015) 191803 [[arXiv:1503.07589](#)] [[INSPIRE](#)].
- [13] ATLAS and CMS collaborations, *Measurements of the Higgs boson production and decay rates and constraints on its couplings from a combined ATLAS and CMS analysis of the LHC pp collision data at $\sqrt{s} = 7$ and 8 TeV*, *JHEP* **08** (2016) 045 [[arXiv:1606.02266](#)] [[INSPIRE](#)].
- [14] ATLAS collaboration, *Measurements of Higgs boson production and couplings in the four-lepton channel in pp collisions at center-of-mass energies of 7 and 8 TeV with the ATLAS detector*, *Phys. Rev. D* **91** (2015) 012006 [[arXiv:1408.5191](#)] [[INSPIRE](#)].
- [15] CMS collaboration, *Measurement of the properties of a Higgs boson in the four-lepton final state*, *Phys. Rev. D* **89** (2014) 092007 [[arXiv:1312.5353](#)] [[INSPIRE](#)].
- [16] CMS collaboration, *Study of the mass and spin-parity of the Higgs boson candidate via its decays to Z boson pairs*, *Phys. Rev. Lett.* **110** (2013) 081803 [[arXiv:1212.6639](#)] [[INSPIRE](#)].
- [17] CMS collaboration, *Constraints on the spin-parity and anomalous HVV couplings of the Higgs boson in proton collisions at 7 and 8 TeV*, *Phys. Rev. D* **92** (2015) 012004 [[arXiv:1411.3441](#)] [[INSPIRE](#)].
- [18] CMS collaboration, *Measurements of properties of the Higgs boson decaying into the four-lepton final state in pp collisions at $\sqrt{s} = 13$ TeV*, *JHEP* **11** (2017) 047 [[arXiv:1706.09936](#)] [[INSPIRE](#)].
- [19] ATLAS collaboration, *Measurement of the Higgs boson coupling properties in the $H \rightarrow ZZ^* \rightarrow 4\ell$ decay channel at $\sqrt{s} = 13$ TeV with the ATLAS detector*, *JHEP* **03** (2018) 095 [[arXiv:1712.02304](#)] [[INSPIRE](#)].
- [20] CMS collaboration, *Constraints on the Higgs boson width from off-shell production and decay to Z-boson pairs*, *Phys. Lett. B* **736** (2014) 64 [[arXiv:1405.3455](#)] [[INSPIRE](#)].
- [21] CMS collaboration, *Limits on the Higgs boson lifetime and width from its decay to four charged leptons*, *Phys. Rev. D* **92** (2015) 072010 [[arXiv:1507.06656](#)] [[INSPIRE](#)].
- [22] ATLAS collaboration, *Constraints on the off-shell Higgs boson signal strength in the high-mass ZZ and WW final states with the ATLAS detector*, *Eur. Phys. J. C* **75** (2015) 335 [[arXiv:1503.01060](#)] [[INSPIRE](#)].
- [23] ATLAS collaboration, *Constraints on off-shell Higgs boson production and the Higgs boson total width in $ZZ \rightarrow 4\ell$ and $ZZ \rightarrow 2\ell 2\nu$ final states with the ATLAS detector*, *Phys. Lett. B* **786** (2018) 223 [[arXiv:1808.01191](#)] [[INSPIRE](#)].
- [24] ATLAS collaboration, *Fiducial and differential cross sections of Higgs boson production measured in the four-lepton decay channel in pp collisions at $\sqrt{s} = 8$ TeV with the ATLAS detector*, *Phys. Lett. B* **738** (2014) 234 [[arXiv:1408.3226](#)] [[INSPIRE](#)].
- [25] CMS collaboration, *Measurement of differential and integrated fiducial cross sections for Higgs boson production in the four-lepton decay channel in pp collisions at $\sqrt{s} = 7$ and 8 TeV*, *JHEP* **04** (2016) 005 [[arXiv:1512.08377](#)] [[INSPIRE](#)].
- [26] ATLAS collaboration, *Measurement of inclusive and differential cross sections in the $H \rightarrow ZZ^* \rightarrow 4\ell$ decay channel in pp collisions at $\sqrt{s} = 13$ TeV with the ATLAS detector*, *JHEP* **10** (2017) 132 [[arXiv:1708.02810](#)] [[INSPIRE](#)].

- [27] ATLAS collaboration, *Higgs boson production cross-section measurements and their EFT interpretation in the 4ℓ decay channel at $\sqrt{s} = 13$ TeV with the ATLAS detector*, *Eur. Phys. J. C* **80** (2020) 957 [Erratum *ibid.* **81** (2021) 29] [[arXiv:2004.03447](#)] [[INSPIRE](#)].
- [28] ATLAS collaboration, *Measurements of the Higgs boson inclusive and differential fiducial cross sections in the 4ℓ decay channel at $\sqrt{s} = 13$ TeV*, *Eur. Phys. J. C* **80** (2020) 942 [[arXiv:2004.03969](#)] [[INSPIRE](#)].
- [29] CMS collaboration, *Constraints on anomalous Higgs boson couplings using production and decay information in the four-lepton final state*, *Phys. Lett. B* **775** (2017) 1 [[arXiv:1707.00541](#)] [[INSPIRE](#)].
- [30] CMS collaboration, *Measurements of the Higgs boson width and anomalous HVV couplings from on-shell and off-shell production in the four-lepton final state*, *Phys. Rev. D* **99** (2019) 112003 [[arXiv:1901.00174](#)] [[INSPIRE](#)].
- [31] CMS collaboration, *Constraints on anomalous Higgs boson couplings to vector bosons and fermions in its production and decay using the four-lepton final state*, *Phys. Rev. D* **104** (2021) 052004 [[arXiv:2104.12152](#)] [[INSPIRE](#)].
- [32] CMS collaboration, *A measurement of the Higgs boson mass in the diphoton decay channel*, *Phys. Lett. B* **805** (2020) 135425 [[arXiv:2002.06398](#)] [[INSPIRE](#)].
- [33] CMS collaboration, *Measurement of the Higgs boson width and evidence of its off-shell contributions to ZZ production*, *Nature Phys.* **18** (2022) 1329 [[arXiv:2202.06923](#)] [[INSPIRE](#)].
- [34] LHC HIGGS CROSS SECTION WORKING GROUP collaboration, *Handbook of LHC Higgs cross sections: 4. Deciphering the nature of the Higgs sector*, [arXiv:1610.07922](#) [[DOI:10.23731/CYRM-2017-002](#)] [[INSPIRE](#)].
- [35] CMS collaboration, *Measurements of production cross sections of the Higgs boson in the four-lepton final state in proton-proton collisions at $\sqrt{s} = 13$ TeV*, *Eur. Phys. J. C* **81** (2021) 488 [[arXiv:2103.04956](#)] [[INSPIRE](#)].
- [36] ATLAS collaboration, *Measurement of the properties of Higgs boson production at $\sqrt{s} = 13$ TeV in the $H \rightarrow \gamma\gamma$ channel using 139 fb^{-1} of pp collision data with the ATLAS experiment*, [ATLAS-CONF-2020-026](#), CERN, Geneva, Switzerland (2020).
- [37] CMS collaboration, *Measurements of Higgs boson production cross sections and couplings in the diphoton decay channel at $\sqrt{s} = 13$ TeV*, *JHEP* **07** (2021) 027 [[arXiv:2103.06956](#)] [[INSPIRE](#)].
- [38] ATLAS collaboration, *Measurements of Higgs boson production by gluon-gluon fusion and vector-boson fusion using $H \rightarrow WW^* \rightarrow e\nu\mu\nu$ decays in pp collisions at $\sqrt{s} = 13$ TeV with the ATLAS detector*, [arXiv:2207.00338](#) [[INSPIRE](#)].
- [39] A. Tumasyan et al., *Measurements of the Higgs boson production cross section and couplings in the W boson pair decay channel in proton-proton collisions at $\sqrt{s} = 13$ TeV*, *Eur. Phys. J. C* **83** (2023) 667 [[arXiv:2206.09466](#)].
- [40] ATLAS collaboration, *Measurements of WH and ZH production in the $H \rightarrow b\bar{b}$ decay channel in pp collisions at 13 TeV with the ATLAS detector*, *Eur. Phys. J. C* **81** (2021) 178 [[arXiv:2007.02873](#)] [[INSPIRE](#)].

- [41] ATLAS collaboration, *Measurements of Higgs boson production cross-sections in the $H \rightarrow \tau^+ \tau^-$ decay channel in pp collisions at $\sqrt{s} = 13$ TeV with the ATLAS detector*, *JHEP* **08** (2022) 175 [[arXiv:2201.08269](#)] [[INSPIRE](#)].
- [42] CMS collaboration, *Measurements of Higgs boson production in the decay channel with a pair of τ leptons in proton-proton collisions at $\sqrt{s} = 13$ TeV*, *Eur. Phys. J. C* **83** (2023) 562 [[arXiv:2204.12957](#)] [[INSPIRE](#)].
- [43] ATLAS collaboration, *A detailed map of Higgs boson interactions by the ATLAS experiment ten years after the discovery*, *Nature* **607** (2022) 52 [Erratum *ibid.* **612** (2022) E24] [[arXiv:2207.00092](#)] [[INSPIRE](#)].
- [44] CMS collaboration, *A portrait of the Higgs boson by the CMS experiment ten years after the discovery*, *Nature* **607** (2022) 60 [[arXiv:2207.00043](#)] [[INSPIRE](#)].
- [45] ATLAS collaboration, *Measurements of the Higgs boson inclusive and differential fiducial cross-sections in the diphoton decay channel with pp collisions at $\sqrt{s} = 13$ TeV with the ATLAS detector*, *JHEP* **08** (2022) 027 [[arXiv:2202.00487](#)] [[INSPIRE](#)].
- [46] CMS collaboration, *Measurement of the Higgs boson inclusive and differential fiducial production cross sections in the diphoton decay channel with pp collisions at $\sqrt{s} = 13$ TeV*, *JHEP* **07** (2023) 091 [[arXiv:2208.12279](#)] [[INSPIRE](#)].
- [47] ATLAS collaboration, *Measurements of differential cross sections of Higgs boson production through gluon fusion in the $H \rightarrow WW^* \rightarrow e\nu\mu\nu$ final state at $\sqrt{s} = 13$ TeV with the ATLAS detector*, [arXiv:2301.06822](#) [[INSPIRE](#)].
- [48] ATLAS collaboration, *Fiducial and differential cross-section measurements for the vector-boson-fusion production of the Higgs boson in the $H \rightarrow WW^* \rightarrow e\nu\mu\nu$ decay channel at 13 TeV with the ATLAS detector*, [arXiv:2304.03053](#) [[INSPIRE](#)].
- [49] CMS collaboration, *Measurement of the inclusive and differential Higgs boson production cross sections in the leptonic WW decay mode at $\sqrt{s} = 13$ TeV*, *JHEP* **03** (2021) 003 [[arXiv:2007.01984](#)] [[INSPIRE](#)].
- [50] CMS collaboration, *Measurement of the inclusive and differential Higgs boson production cross sections in the decay mode to a pair of τ leptons in pp collisions at $\sqrt{s} = 13$ TeV*, *Phys. Rev. Lett.* **128** (2022) 081805 [[arXiv:2107.11486](#)] [[INSPIRE](#)].
- [51] ATLAS collaboration, *Measurement of the total and differential Higgs boson production cross-sections at $\sqrt{s} = 13$ TeV with the ATLAS detector by combining the $H \rightarrow ZZ^* \rightarrow 4l$ and $H \rightarrow \gamma\gamma$ decay channels*, *JHEP* **05** (2023) 028 [[arXiv:2207.08615](#)] [[INSPIRE](#)].
- [52] CMS collaboration, *Measurement and interpretation of differential cross sections for Higgs boson production at $\sqrt{s} = 13$ TeV*, *Phys. Lett. B* **792** (2019) 369 [[arXiv:1812.06504](#)] [[INSPIRE](#)].
- [53] CMS collaboration, *Performance of the CMS level-1 trigger in proton-proton collisions at $\sqrt{s} = 13$ TeV*, **2020 JINST** **15** P10017 [[arXiv:2006.10165](#)] [[INSPIRE](#)].
- [54] CMS collaboration, *The CMS trigger system*, **2017 JINST** **12** P01020 [[arXiv:1609.02366](#)] [[INSPIRE](#)].
- [55] D. Contardo et al., *Technical proposal for the phase-II upgrade of the CMS detector*, **CERN-LHCC-2015-010**, CERN, Geneva, Switzerland (2015) [[DOI:10.17181/CERN.VU8I.D59J](#)].
- [56] CMS collaboration, *Electron and photon reconstruction and identification with the CMS experiment at the CERN LHC*, **2021 JINST** **16** P05014 [[arXiv:2012.06888](#)] [[INSPIRE](#)].

- [57] CMS collaboration, *ECAL 2016 refined calibration and Run2 summary plots*, [CMS-DP-2020-021](#), CERN, Geneva, Switzerland (2020).
- [58] CMS collaboration, *Performance of the CMS muon detector and muon reconstruction with proton-proton collisions at $\sqrt{s} = 13$ TeV*, [2018 JINST **13** P06015](#) [[arXiv:1804.04528](#)] [[INSPIRE](#)].
- [59] CMS collaboration, *The CMS experiment at the CERN LHC*, [2008 JINST **3** S08004](#) [[INSPIRE](#)].
- [60] CMS collaboration, *Precision luminosity measurement in proton-proton collisions at $\sqrt{s} = 13$ TeV in 2015 and 2016 at CMS*, [Eur. Phys. J. C **81** \(2021\) 800](#) [[arXiv:2104.01927](#)] [[INSPIRE](#)].
- [61] CMS collaboration, *CMS luminosity measurement for the 2017 data-taking period at $\sqrt{s} = 13$ TeV*, [CMS-PAS-LUM-17-004](#), CERN, Geneva, Switzerland (2018).
- [62] CMS collaboration, *CMS luminosity measurement for the 2018 data-taking period at $\sqrt{s} = 13$ TeV*, [CMS-PAS-LUM-18-002](#), CERN, Geneva, Switzerland (2019).
- [63] CMS collaboration, *Measurement of the inclusive W and Z production cross sections in pp collisions at $\sqrt{s} = 7$ TeV*, [JHEP **10** \(2011\) 132](#) [[arXiv:1107.4789](#)] [[INSPIRE](#)].
- [64] P. Nason, *A new method for combining NLO QCD with shower Monte Carlo algorithms*, [JHEP **11** \(2004\) 040](#) [[hep-ph/0409146](#)] [[INSPIRE](#)].
- [65] S. Frixione, P. Nason and C. Oleari, *Matching NLO QCD computations with parton shower simulations: the POWHEG method*, [JHEP **11** \(2007\) 070](#) [[arXiv:0709.2092](#)] [[INSPIRE](#)].
- [66] S. Alioli, P. Nason, C. Oleari and E. Re, *A general framework for implementing NLO calculations in shower Monte Carlo programs: the POWHEG BOX*, [JHEP **06** \(2010\) 043](#) [[arXiv:1002.2581](#)] [[INSPIRE](#)].
- [67] S. Alioli, P. Nason, C. Oleari and E. Re, *NLO Higgs boson production via gluon fusion matched with shower in POWHEG*, [JHEP **04** \(2009\) 002](#) [[arXiv:0812.0578](#)] [[INSPIRE](#)].
- [68] P. Nason and C. Oleari, *NLO Higgs boson production via vector-boson fusion matched with shower in POWHEG*, [JHEP **02** \(2010\) 037](#) [[arXiv:0911.5299](#)] [[INSPIRE](#)].
- [69] G. Luisoni, P. Nason, C. Oleari and F. Tramontano, *$HW^\pm/HZ + 0$ and 1 jet at NLO with the POWHEG BOX interfaced to GoSam and their merging within MiNLO*, [JHEP **10** \(2013\) 083](#) [[arXiv:1306.2542](#)] [[INSPIRE](#)].
- [70] H.B. Hartanto, B. Jager, L. Reina and D. Wackerlo, *Higgs boson production in association with top quarks in the POWHEG BOX*, [Phys. Rev. D **91** \(2015\) 094003](#) [[arXiv:1501.04498](#)] [[INSPIRE](#)].
- [71] K. Hamilton, P. Nason, E. Re and G. Zanderighi, *NNLOPS simulation of Higgs boson production*, [JHEP **10** \(2013\) 222](#) [[arXiv:1309.0017](#)] [[INSPIRE](#)].
- [72] Y. Gao et al., *Spin determination of single-produced resonances at hadron colliders*, [Phys. Rev. D **81** \(2010\) 075022](#) [[arXiv:1001.3396](#)] [[INSPIRE](#)].
- [73] S. Bolognesi et al., *On the spin and parity of a single-produced resonance at the LHC*, [Phys. Rev. D **86** \(2012\) 095031](#) [[arXiv:1208.4018](#)] [[INSPIRE](#)].
- [74] I. Anderson et al., *Constraining anomalous HVV interactions at proton and lepton colliders*, [Phys. Rev. D **89** \(2014\) 035007](#) [[arXiv:1309.4819](#)] [[INSPIRE](#)].

- [75] A.V. Gritsan, R. Röntsch, M. Schulze and M. Xiao, *Constraining anomalous Higgs boson couplings to the heavy flavor fermions using matrix element techniques*, *Phys. Rev. D* **94** (2016) 055023 [[arXiv:1606.03107](#)] [[INSPIRE](#)].
- [76] A.V. Gritsan et al., *New features in the JHU generator framework: constraining Higgs boson properties from on-shell and off-shell production*, *Phys. Rev. D* **102** (2020) 056022 [[arXiv:2002.09888](#)] [[INSPIRE](#)].
- [77] M. Wiesemann et al., *Higgs production in association with bottom quarks*, *JHEP* **02** (2015) 132 [[arXiv:1409.5301](#)] [[INSPIRE](#)].
- [78] C. Anastasiou et al., *Higgs boson gluon-fusion production in QCD at three loops*, *Phys. Rev. Lett.* **114** (2015) 212001 [[arXiv:1503.06056](#)] [[INSPIRE](#)].
- [79] C. Anastasiou et al., *High precision determination of the gluon fusion Higgs boson cross-section at the LHC*, *JHEP* **05** (2016) 058 [[arXiv:1602.00695](#)] [[INSPIRE](#)].
- [80] M. Ciccolini, A. Denner and S. Dittmaier, *Strong and electroweak corrections to the production of Higgs + 2 jets via weak interactions at the LHC*, *Phys. Rev. Lett.* **99** (2007) 161803 [[arXiv:0707.0381](#)] [[INSPIRE](#)].
- [81] M. Ciccolini, A. Denner and S. Dittmaier, *Electroweak and QCD corrections to Higgs production via vector-boson fusion at the LHC*, *Phys. Rev. D* **77** (2008) 013002 [[arXiv:0710.4749](#)] [[INSPIRE](#)].
- [82] P. Bolzoni, F. Maltoni, S.-O. Moch and M. Zaro, *Higgs production via vector-boson fusion at NNLO in QCD*, *Phys. Rev. Lett.* **105** (2010) 011801 [[arXiv:1003.4451](#)] [[INSPIRE](#)].
- [83] P. Bolzoni, F. Maltoni, S.-O. Moch and M. Zaro, *Vector boson fusion at NNLO in QCD: SM Higgs and beyond*, *Phys. Rev. D* **85** (2012) 035002 [[arXiv:1109.3717](#)] [[INSPIRE](#)].
- [84] O. Brein, A. Djouadi and R. Harlander, *NNLO QCD corrections to the Higgs-strahlung processes at hadron colliders*, *Phys. Lett. B* **579** (2004) 149 [[hep-ph/0307206](#)] [[INSPIRE](#)].
- [85] M.L. Ciccolini, S. Dittmaier and M. Krämer, *Electroweak radiative corrections to associated WH and ZH production at hadron colliders*, *Phys. Rev. D* **68** (2003) 073003 [[hep-ph/0306234](#)] [[INSPIRE](#)].
- [86] W. Beenakker et al., *Higgs radiation off top quarks at the Tevatron and the LHC*, *Phys. Rev. Lett.* **87** (2001) 201805 [[hep-ph/0107081](#)] [[INSPIRE](#)].
- [87] W. Beenakker et al., *NLO QCD corrections to $t\bar{t}H$ production in hadron collisions*, *Nucl. Phys. B* **653** (2003) 151 [[hep-ph/0211352](#)] [[INSPIRE](#)].
- [88] S. Dawson, L.H. Orr, L. Reina and D. Wackerlo, *Associated top quark Higgs boson production at the LHC*, *Phys. Rev. D* **67** (2003) 071503 [[hep-ph/0211438](#)] [[INSPIRE](#)].
- [89] S. Dawson et al., *Associated Higgs production with top quarks at the Large Hadron Collider: NLO QCD corrections*, *Phys. Rev. D* **68** (2003) 034022 [[hep-ph/0305087](#)] [[INSPIRE](#)].
- [90] Y. Zhang et al., *QCD NLO and EW NLO corrections to $t\bar{t}H$ production with top quark decays at hadron collider*, *Phys. Lett. B* **738** (2014) 1 [[arXiv:1407.1110](#)] [[INSPIRE](#)].
- [91] S. Frixione et al., *Weak corrections to Higgs hadroproduction in association with a top-quark pair*, *JHEP* **09** (2014) 065 [[arXiv:1407.0823](#)] [[INSPIRE](#)].
- [92] F. Demartin, F. Maltoni, K. Mawatari and M. Zaro, *Higgs production in association with a single top quark at the LHC*, *Eur. Phys. J. C* **75** (2015) 267 [[arXiv:1504.00611](#)] [[INSPIRE](#)].

- [93] F. Demartin et al., *tWH associated production at the LHC*, *Eur. Phys. J. C* **77** (2017) 34 [[arXiv:1607.05862](#)] [[INSPIRE](#)].
- [94] A. Denner et al., *Standard Model Higgs-boson branching ratios with uncertainties*, *Eur. Phys. J. C* **71** (2011) 1753 [[arXiv:1107.5909](#)] [[INSPIRE](#)].
- [95] A. Djouadi, J. Kalinowski and M. Spira, *HDECAY: a program for Higgs boson decays in the Standard Model and its supersymmetric extension*, *Comput. Phys. Commun.* **108** (1998) 56 [[hep-ph/9704448](#)] [[INSPIRE](#)].
- [96] J.M. Butterworth et al., *The tools and Monte Carlo working group summary report from the Les Houches 2009 workshop on TeV colliders*, in the proceedings of the 6th *Les Houches workshop on physics at TeV colliders*, (2010) [[arXiv:1003.1643](#)] [[INSPIRE](#)].
- [97] A. Bredenstein, A. Denner, S. Dittmaier and M.M. Weber, *Precise predictions for the Higgs-boson decay $H \rightarrow WW/ZZ \rightarrow 4$ leptons*, *Phys. Rev. D* **74** (2006) 013004 [[hep-ph/0604011](#)] [[INSPIRE](#)].
- [98] A. Bredenstein, A. Denner, S. Dittmaier and M.M. Weber, *Radiative corrections to the semileptonic and hadronic Higgs-boson decays $H \rightarrow WW/ZZ \rightarrow 4$ fermions*, *JHEP* **02** (2007) 080 [[hep-ph/0611234](#)] [[INSPIRE](#)].
- [99] S. Boselli et al., *Higgs boson decay into four leptons at NLOPS electroweak accuracy*, *JHEP* **06** (2015) 023 [[arXiv:1503.07394](#)] [[INSPIRE](#)].
- [100] S. Actis, G. Passarino, C. Sturm and S. Uccirati, *NNLO computational techniques: the cases $H \rightarrow \gamma\gamma$ and $H \rightarrow gg$* , *Nucl. Phys. B* **811** (2009) 182 [[arXiv:0809.3667](#)] [[INSPIRE](#)].
- [101] T. Melia, P. Nason, R. Rontsch and G. Zanderighi, *W^+W^- , WZ and ZZ production in the POWHEG BOX*, *JHEP* **11** (2011) 078 [[arXiv:1107.5051](#)] [[INSPIRE](#)].
- [102] J.M. Campbell and R.K. Ellis, *MCFM for the Tevatron and the LHC*, *Nucl. Phys. B Proc. Suppl.* **205-206** (2010) 10 [[arXiv:1007.3492](#)] [[INSPIRE](#)].
- [103] J.M. Campbell, R.K. Ellis and C. Williams, *Vector boson pair production at the LHC*, *JHEP* **07** (2011) 018 [[arXiv:1105.0020](#)] [[INSPIRE](#)].
- [104] J.M. Campbell, R.K. Ellis and C. Williams, *Bounding the Higgs width at the LHC using full analytic results for $gg \rightarrow e^-e^+\mu^-\mu^+$* , *JHEP* **04** (2014) 060 [[arXiv:1311.3589](#)] [[INSPIRE](#)].
- [105] J.M. Campbell and R.K. Ellis, *Higgs constraints from vector boson fusion and scattering*, *JHEP* **04** (2015) 030 [[arXiv:1502.02990](#)] [[INSPIRE](#)].
- [106] T. Sjöstrand et al., *An introduction to PYTHIA 8.2*, *Comput. Phys. Commun.* **191** (2015) 159 [[arXiv:1410.3012](#)] [[INSPIRE](#)].
- [107] CMS collaboration, *Event generator tunes obtained from underlying event and multiparton scattering measurements*, *Eur. Phys. J. C* **76** (2016) 155 [[arXiv:1512.00815](#)] [[INSPIRE](#)].
- [108] CMS collaboration, *Extraction and validation of a new set of CMS PYTHIA8 tunes from underlying-event measurements*, *Eur. Phys. J. C* **80** (2020) 4 [[arXiv:1903.12179](#)] [[INSPIRE](#)].
- [109] NNPDF collaboration, *Parton distributions for the LHC run II*, *JHEP* **04** (2015) 040 [[arXiv:1410.8849](#)] [[INSPIRE](#)].
- [110] GEANT4 collaboration, *GEANT4 — a simulation toolkit*, *Nucl. Instrum. Meth. A* **506** (2003) 250 [[INSPIRE](#)].

- [111] J. Allison et al., *GEANT4 developments and applications*, *IEEE Trans. Nucl. Sci.* **53** (2006) 270 [[INSPIRE](#)].
- [112] CMS collaboration, *Particle-flow reconstruction and global event description with the CMS detector*, *2017 JINST* **12** P10003 [[arXiv:1706.04965](#)] [[INSPIRE](#)].
- [113] T. Chen and C. Guestrin, *XGBoost: a scalable tree boosting system*, [arXiv:1603.02754](#) [[DOI:10.1145/2939672.2939785](#)] [[INSPIRE](#)].
- [114] CMS collaboration, *Pileup mitigation at CMS in 13 TeV data*, *2020 JINST* **15** P09018 [[arXiv:2003.00503](#)] [[INSPIRE](#)].
- [115] M. Cacciari, G.P. Salam and G. Soyez, *The anti- k_t jet clustering algorithm*, *JHEP* **04** (2008) 063 [[arXiv:0802.1189](#)] [[INSPIRE](#)].
- [116] M. Cacciari, G.P. Salam and G. Soyez, *FastJet user manual*, *Eur. Phys. J. C* **72** (2012) 1896 [[arXiv:1111.6097](#)] [[INSPIRE](#)].
- [117] CMS collaboration, *Jet energy scale and resolution in the CMS experiment in pp collisions at 8 TeV*, *2017 JINST* **12** P02014 [[arXiv:1607.03663](#)] [[INSPIRE](#)].
- [118] PARTICLE DATA GROUP collaboration, *Review of particle physics*, *PTEP* **2022** (2022) 083C01 [[INSPIRE](#)].
- [119] S. Gangal, M. Stahlhofen and F.J. Tackmann, *Rapidity-dependent jet vetoes*, *Phys. Rev. D* **91** (2015) 054023 [[arXiv:1412.4792](#)] [[INSPIRE](#)].
- [120] M. Grazzini, S. Kallweit and D. Rathlev, *ZZ production at the LHC: fiducial cross sections and distributions in NNLO QCD*, *Phys. Lett. B* **750** (2015) 407 [[arXiv:1507.06257](#)] [[INSPIRE](#)].
- [121] A. Bierweiler, T. Kasprzik and J.H. Kühn, *Vector-boson pair production at the LHC to $\mathcal{O}(\alpha^3)$ accuracy*, *JHEP* **12** (2013) 071 [[arXiv:1305.5402](#)] [[INSPIRE](#)].
- [122] M. Bonvini et al., *Signal-background interference effects for $gg \rightarrow H \rightarrow W^+W^-$ beyond leading order*, *Phys. Rev. D* **88** (2013) 034032 [[arXiv:1304.3053](#)] [[INSPIRE](#)].
- [123] K. Melnikov and M. Dowling, *Production of two Z-bosons in gluon fusion in the heavy top quark approximation*, *Phys. Lett. B* **744** (2015) 43 [[arXiv:1503.01274](#)] [[INSPIRE](#)].
- [124] C.S. Li, H.T. Li, D.Y. Shao and J. Wang, *Soft gluon resummation in the signal-background interference process of $gg(\rightarrow h^*) \rightarrow ZZ$* , *JHEP* **08** (2015) 065 [[arXiv:1504.02388](#)] [[INSPIRE](#)].
- [125] G. Passarino, *Higgs CAT*, *Eur. Phys. J. C* **74** (2014) 2866 [[arXiv:1312.2397](#)] [[INSPIRE](#)].
- [126] S. Catani and M. Grazzini, *An NNLO subtraction formalism in hadron collisions and its application to Higgs boson production at the LHC*, *Phys. Rev. Lett.* **98** (2007) 222002 [[hep-ph/0703012](#)] [[INSPIRE](#)].
- [127] M. Grazzini, *NNLO predictions for the Higgs boson signal in the $H \rightarrow WW \rightarrow \ell\nu\ell\nu$ and $H \rightarrow ZZ \rightarrow 4\ell$ decay channels*, *JHEP* **02** (2008) 043 [[arXiv:0801.3232](#)] [[INSPIRE](#)].
- [128] M. Grazzini and H. Sargsyan, *Heavy-quark mass effects in Higgs boson production at the LHC*, *JHEP* **09** (2013) 129 [[arXiv:1306.4581](#)] [[INSPIRE](#)].
- [129] T. Skwarnicki, *A study of the radiative CASCADE transitions between the Upsilon-prime and Upsilon resonances*, Ph.D. thesis, INP, Cracow, Poland (1986) [[INSPIRE](#)].

- [130] ATLAS et al. collaborations, *Procedure for the LHC Higgs boson search combination in Summer 2011*, CMS-NOTE-2011-005, CERN, Geneva, Switzerland (2011).
- [131] G. Cowan, K. Cranmer, E. Gross and O. Vitells, *Asymptotic formulae for likelihood-based tests of new physics*, *Eur. Phys. J. C* **71** (2011) 1554 [*Erratum ibid.* **73** (2013) 2501] [[arXiv:1007.1727](#)] [[INSPIRE](#)].
- [132] CMS collaboration, *Measurement of differential cross sections for Higgs boson production in the diphoton decay channel in pp collisions at $\sqrt{s} = 8$ TeV*, *Eur. Phys. J. C* **76** (2016) 13 [[arXiv:1508.07819](#)] [[INSPIRE](#)].
- [133] J. Butterworth et al., *PDF4LHC recommendations for LHC run II*, *J. Phys. G* **43** (2016) 023001 [[arXiv:1510.03865](#)] [[INSPIRE](#)].
- [134] ATLAS collaboration, *Electron reconstruction and identification in the ATLAS experiment using the 2015 and 2016 LHC proton-proton collision data at $\sqrt{s} = 13$ TeV*, *Eur. Phys. J. C* **79** (2019) 639 [[arXiv:1902.04655](#)] [[INSPIRE](#)].
- [135] *HEPData record for this analysis*, CMS-HIG-21-009 (2023).
- [136] D. de Florian, G. Ferrera, M. Grazzini and D. Tommasini, *Higgs boson production at the LHC: transverse momentum resummation effects in the $H \rightarrow \gamma\gamma$, $H \rightarrow WW \rightarrow \ell\nu\ell\nu$ and $H \rightarrow ZZ \rightarrow 4\ell$ decay modes*, *JHEP* **06** (2012) 132 [[arXiv:1203.6321](#)] [[INSPIRE](#)].
- [137] G. Degrassi, P.P. Giardino, F. Maltoni and D. Pagani, *Probing the Higgs self coupling via single Higgs production at the LHC*, *JHEP* **12** (2016) 080 [[arXiv:1607.04251](#)] [[INSPIRE](#)].
- [138] F. Maltoni, D. Pagani, A. Shivaji and X. Zhao, *Trilinear Higgs coupling determination via single-Higgs differential measurements at the LHC*, *Eur. Phys. J. C* **77** (2017) 887 [[arXiv:1709.08649](#)] [[INSPIRE](#)].
- [139] S. Di Vita et al., *A global view on the Higgs self-coupling*, *JHEP* **09** (2017) 069 [[arXiv:1704.01953](#)] [[INSPIRE](#)].
- [140] ATLAS collaboration, *Constraints on the Higgs boson self-coupling from single- and double-Higgs production with the ATLAS detector using pp collisions at $\sqrt{s} = 13$ TeV*, *Phys. Lett. B* **843** (2023) 137745 [[arXiv:2211.01216](#)] [[INSPIRE](#)].
- [141] LHC HIGGS CROSS SECTION WORKING GROUP collaboration, *Handbook of LHC Higgs cross sections: 3. Higgs properties*, [arXiv:1307.1347](#) [DOI:10.5170/CERN-2013-004] [[INSPIRE](#)].
- [142] F. Bishara, U. Haisch, P.F. Monni and E. Re, *Constraining light-quark Yukawa couplings from Higgs distributions*, *Phys. Rev. Lett.* **118** (2017) 121801 [[arXiv:1606.09253](#)] [[INSPIRE](#)].

The CMS collaboration

Yerevan Physics Institute, Yerevan, Armenia

A. Hayrapetyan, A. Tumasyan¹

Institut für Hochenergiephysik, Vienna, Austria

W. Adam¹, J.W. Andrejkovic, T. Bergauer¹, S. Chatterjee¹, K. Damanakis¹,
 M. Dragicevic¹, A. Escalante Del Valle¹, P.S. Hussain¹, M. Jeitler^{1,2}, N. Krammer¹,
 L. Lechner¹, D. Liko¹, I. Mikulec¹, J. Schieck^{1,2}, R. Schöfbeck¹, D. Schwarz¹,
 M. Sonawane¹, S. Templ¹, W. Waltenberger¹, C.-E. Wulz^{1,2}

Universiteit Antwerpen, Antwerpen, Belgium

M.R. Darwish³, T. Janssen¹, T. Kello⁴, P. Van Mechelen¹

Vrije Universiteit Brussel, Brussel, Belgium

E.S. Bols¹, J. D'Hondt¹, A. De Moor¹, M. Delcourt¹, H. El Faham¹, S. Lowette¹,
 I. Makarenko¹, A. Morton¹, D. Müller¹, A.R. Sahasransu¹, S. Tavernier¹, S. Van Putte¹,
 D. Vannerom¹

Université Libre de Bruxelles, Bruxelles, Belgium

B. Clerbaux¹, S. Dansana¹, G. De Lentdecker¹, L. Favart¹, D. Hohov¹, J. Jaramillo¹,
 K. Lee¹, M. Mahdavikhorrami¹, A. Malara¹, S. Paredes¹, L. Pétré¹, N. Postiau,
 L. Thomas¹, M. Vanden Bemden, C. Vander Velde¹, P. Vanlaer¹

Ghent University, Ghent, Belgium

M. De Coen¹, D. Dobur¹, J. Knolle¹, L. Lambrecht¹, G. Mestdach, C. Rendón, A. Samalan,
 K. Skovpen¹, M. Tytgat¹, N. Van Den Bossche¹, B. Vermassen, L. Wezenbeek¹

Université Catholique de Louvain, Louvain-la-Neuve, Belgium

A. Benecke¹, G. Bruno¹, F. Bury¹, C. Caputo¹, C. Delaere¹, I.S. Donertas¹,
 A. Giannmanco¹, K. Jaffel¹, Sa. Jain¹, V. Lemaitre, J. Lidrych¹, P. Mastrapasqua¹,
 K. Mondal¹, T.T. Tran¹, S. Wertz¹

Centro Brasileiro de Pesquisas Fisicas, Rio de Janeiro, Brazil

G.A. Alves¹, E. Coelho¹, C. Hensel¹, A. Moraes¹, P. Rebello Teles¹

Universidade do Estado do Rio de Janeiro, Rio de Janeiro, Brazil

W.L. Aldá Júnior¹, M. Alves Gallo Pereira¹, M. Barroso Ferreira Filho¹,
 H. Brandao Malbouisson¹, W. Carvalho¹, J. Chinellato⁵, E.M. Da Costa¹,
 G.G. Da Silveira^{1,6}, D. De Jesus Damiao¹, V. Dos Santos Sousa¹, S. Fonseca De Souza¹,
 J. Martins^{1,7}, C. Mora Herrera¹, K. Mota Amarilo¹, L. Mundim¹, H. Nogima¹,
 A. Santoro¹, S.M. Silva Do Amaral¹, A. Sznajder¹, M. Thiel¹, A. Vilela Pereira¹

**Universidade Estadual Paulista, Universidade Federal do ABC, São Paulo,
Brazil**

C.A. Bernardes⁶, L. Calligaris^{ID}, T.R. Fernandez Perez Tomei^{ID}, E.M. Gregores^{ID},
P.G. Mercadante^{ID}, S.F. Novaes^{ID}, B. Orzari^{ID}, Sandra S. Padula^{ID}

**Institute for Nuclear Research and Nuclear Energy, Bulgarian Academy of
Sciences, Sofia, Bulgaria**

A. Aleksandrov^{ID}, G. Antchev^{ID}, R. Hadjiiska^{ID}, P. Iaydjiev^{ID}, M. Misheva^{ID}, M. Shopova^{ID},
G. Sultanov^{ID}

University of Sofia, Sofia, Bulgaria

A. Dimitrov^{ID}, T. Ivanov^{ID}, L. Litov^{ID}, B. Pavlov^{ID}, P. Petkov^{ID}, A. Petrov, E. Shumka^{ID}

**Instituto De Alta Investigación, Universidad de Tarapacá, Casilla 7 D, Arica,
Chile**

S. Keshri^{ID}, S.Thakur^{ID}

Beihang University, Beijing, China

T. Cheng^{ID}, Q. Guo, T. Javaid^{ID}, M. Mittal^{ID}, L. Yuan^{ID}

Department of Physics, Tsinghua University, Beijing, China

G. Bauer⁸, Z. Hu^{ID}, K. Yi^{ID}^{8,9}

Institute of High Energy Physics, Beijing, China

G.M. Chen^{ID}¹⁰, H.S. Chen^{ID}¹⁰, M. Chen^{ID}¹⁰, F. Iemmi^{ID}, C.H. Jiang, A. Kapoor^{ID}, H. Liao^{ID},
Z.-A. Liu^{ID}¹¹, F. Monti^{ID}, R. Sharma^{ID}, J.N. Song¹¹, J. Tao^{ID}, J. Wang^{ID}, C. Zhang¹⁰,
H. Zhang^{ID}

**State Key Laboratory of Nuclear Physics and Technology, Peking University,
Beijing, China**

A. Agapitos^{ID}, Y. Ban^{ID}, A. Levin^{ID}, C. Li^{ID}, Q. Li^{ID}, X. Lyu, Y. Mao, S.J. Qian^{ID}, X. Sun^{ID},
D. Wang^{ID}, H. Yang

Sun Yat-Sen University, Guangzhou, China

M. Lu^{ID}, Z. You^{ID}

University of Science and Technology of China, Hefei, China

N. Lu^{ID}

**Institute of Modern Physics and Key Laboratory of Nuclear Physics and
Ion-beam Application (MOE) — Fudan University, Shanghai, China**

X. Gao^{ID}⁴, D. Leggat, H. Okawa^{ID}, Y. Zhang^{ID}

Zhejiang University, Hangzhou, Zhejiang, China

Z. Lin^{ID}, C. Lu^{ID}, M. Xiao^{ID}

Universidad de Los Andes, Bogota, ColombiaC. Avila , D.A. Barbosa Trujillo, A. Cabrera , C. Florez , J. Fraga , J.A. Reyes Vega**Universidad de Antioquia, Medellin, Colombia**J. Mejia Guisao , F. Ramirez , M. Rodriguez , J.D. Ruiz Alvarez **University of Split, Faculty of Electrical Engineering, Mechanical Engineering and Naval Architecture, Split, Croatia**D. Giljanovic , N. Godinovic , D. Lelas , A. Sculac **University of Split, Faculty of Science, Split, Croatia**M. Kovac , T. Sculac **Institute Rudjer Boskovic, Zagreb, Croatia**P. Bargassa , V. Brigljevic , B.K. Chitroda , D. Ferencek , S. Mishra , A. Starodumov ¹², T. Susa **University of Cyprus, Nicosia, Cyprus**A. Attikis , K. Christoforou , S. Konstantinou , J. Mousa , C. Nicolaou, F. Ptochos , P.A. Razis , H. Rykaczewski, H. Saka , A. Stepennov **Charles University, Prague, Czech Republic**M. Finger , M. Finger Jr. , A. Kveton **Escuela Politecnica Nacional, Quito, Ecuador**E. Ayala **Universidad San Francisco de Quito, Quito, Ecuador**E. Carrera Jarrin **Academy of Scientific Research and Technology of the Arab Republic of Egypt, Egyptian Network of High Energy Physics, Cairo, Egypt**Y. Assran^{13,14}, S. Elgammal¹⁴**Center for High Energy Physics (CHEP-FU), Fayoum University, El-Fayoum, Egypt**M. Abdullah Al-Mashad , M.A. Mahmoud **National Institute of Chemical Physics and Biophysics, Tallinn, Estonia**K. Ehataht , M. Kadastik, T. Lange , S. Nandan , C. Nielsen , J. Pata , M. Raidal , L. Tani , C. Veelken **Department of Physics, University of Helsinki, Helsinki, Finland**H. Kirschenmann , K. Osterberg , M. Voutilainen 

Helsinki Institute of Physics, Helsinki, Finland

S. Bharthuar , E. Brücken , F. Garcia , J. Havukainen , K.T.S. Kallonen , M.S. Kim , R. Kinnunen, T. Lampén , K. Lassila-Perini , S. Lehti , T. Lindén , M. Lotti, L. Martikainen , M. Myllymäki , M.m. Rantanen , H. Siikonen , E. Tuominen , J. Tuominiemi

Lappeenranta-Lahti University of Technology, Lappeenranta, Finland

P. Luukka , H. Petrow , T. Tuuva[†]

IRFU, CEA, Université Paris-Saclay, Gif-sur-Yvette, France

C. Amendola , M. Besancon , F. Couderc , M. Dejardin , D. Denegri, J.L. Faure, F. Ferri , S. Ganjour , P. Gras , G. Hamel de Monchenault , V. Lohezic , J. Malcles , J. Rander, A. Rosowsky , M.Ö. Sahin , A. Savoy-Navarro ¹⁵, P. Simkina , M. Titov

Laboratoire Leprince-Ringuet, CNRS/IN2P3, Ecole Polytechnique, Institut Polytechnique de Paris, Palaiseau, France

C. Baldenegro Barrera , F. Beaudette , A. Buchot Perraguin , P. Busson , A. Cappati , C. Charlot , F. Damas , O. Davignon , B. Diab , G. Falmagne , B.A. Fontana Santos Alves , S. Ghosh , R. Granier de Cassagnac , A. Hakimi , B. Harikrishnan , G. Liu , J. Motta , M. Nguyen , C. Ochando , L. Portales , R. Salerno , U. Sarkar , J.B. Sauvan , Y. Sirois , A. Tarabini , E. Vernazza , A. Zabi , A. Zghiche

Université de Strasbourg, CNRS, IPHC UMR 7178, Strasbourg, France

J.-L. Agram ¹⁶, J. Andrea , D. Apparu , D. Bloch , J.-M. Brom , E.C. Chabert , C. Collard , U. Goerlach , C. Grimault, A.-C. Le Bihan , P. Van Hove

Institut de Physique des 2 Infinis de Lyon (IP2I), Villeurbanne, France

S. Beauceron , B. Blancon , G. Boudoul , N. Chanon , J. Choi , D. Contardo , P. Depasse , C. Dozen ¹⁷, H. El Mamouni, J. Fay , S. Gascon , M. Gouzevitch , C. Greenberg, G. Grenier , B. Ille , I.B. Laktineh, M. Lethuillier , L. Mirabito, S. Perries, M. Vander Donckt , P. Verdier , J. Xiao

Georgian Technical University, Tbilisi, Georgia

A. Khvedelidze ¹², I. Lomidze , Z. Tsamalaidze ¹²

RWTH Aachen University, I. Physikalisches Institut, Aachen, Germany

V. Botta , L. Feld , K. Klein , M. Lipinski , D. Meuser , A. Pauls , N. Röwert , M. Teroerde

RWTH Aachen University, III. Physikalisches Institut A, Aachen, Germany

S. Diekmann , A. Dodonova , N. Eich , D. Eliseev , M. Erdmann , P. Fackeldey , B. Fischer , T. Hebbeker , K. Hoepfner , F. Ivone , M.y. Lee , L. Mastrolorenzo, M. Merschmeyer , A. Meyer , S. Mondal , S. Mukherjee , D. Noll , A. Novak , F. Nowotny, A. Pozdnyakov , Y. Rath, W. Redjeb , F. Rehm, H. Reithler , A. Schmidt

S.C. Schuler, A. Sharma^{ID}, A. Stein^{ID}, F. Torres Da Silva De Araujo^{ID}¹⁸, L. Vigilante,
S. Wiedenbeck^{ID}, S. Zaleski

RWTH Aachen University, III. Physikalisches Institut B, Aachen, Germany

C. Dziwok^{ID}, G. Flügge^{ID}, W. Haj Ahmad^{ID}¹⁹, T. Kress^{ID}, A. Nowack^{ID}, O. Pooth^{ID},
A. Stahl^{ID}, T. Ziemons^{ID}, A. Zotz^{ID}

Deutsches Elektronen-Synchrotron, Hamburg, Germany

H. Aarup Petersen^{ID}, M. Aldaya Martin^{ID}, J. Alimena^{ID}, S. Amoroso, Y. An^{ID}, S. Baxter^{ID},
M. Bayatmakou^{ID}, H. Becerril Gonzalez^{ID}, O. Behnke^{ID}, S. Bhattacharya^{ID}, F. Blekman^{ID}²⁰,
K. Borras^{ID}²¹, D. Brunner^{ID}, A. Campbell^{ID}, A. Cardini^{ID}, C. Cheng, F. Colombina,
S. Consuegra Rodríguez^{ID}, G. Correia Silva^{ID}, M. De Silva^{ID}, G. Eckerlin, D. Eckstein^{ID},
L.I. Estevez Banos^{ID}, O. Filatov^{ID}, E. Gallo^{ID}²⁰, A. Geiser^{ID}, A. Giraldi^{ID}, G. Greau,
V. Guglielmi^{ID}, M. Guthoff^{ID}, A. Jafari^{ID}²², N.Z. Jomhari^{ID}, B. Kaech^{ID}, M. Kasemann^{ID},
H. Kaveh^{ID}, C. Kleinwort^{ID}, R. Kogler^{ID}, M. Komm^{ID}, D. Krücker^{ID}, W. Lange,
D. Leyva Pernia^{ID}, K. Lipka^{ID}²³, W. Lohmann^{ID}²⁴, R. Mankel^{ID}, I.-A. Melzer-Pellmann^{ID},
M. Mendizabal Morentin^{ID}, J. Metwally, A.B. Meyer^{ID}, G. Milella^{ID}, M. Mormile^{ID},
A. Mussgiller^{ID}, A. Nürnberg^{ID}, Y. Otarid, D. Pérez Adán^{ID}, E. Ranken^{ID}, A. Raspereza^{ID},
B. Ribeiro Lopes^{ID}, J. Rübenach, A. Saggio^{ID}, M. Scham^{ID}^{25,21}, V. Scheurer, S. Schnake^{ID}²¹,
P. Schütze^{ID}, C. Schwanenberger^{ID}²⁰, M. Shchedrolosiev^{ID}, R.E. Sosa Ricardo^{ID},
L.P. Sreelatha Pramod^{ID}, D. Stafford, F. Vazzoler^{ID}, A. Ventura Barroso^{ID}, R. Walsh^{ID},
Q. Wang^{ID}, Y. Wen^{ID}, K. Wichmann, L. Wiens^{ID}²¹, C. Wissing^{ID}, S. Wuchterl^{ID}, Y. Yang^{ID},
A. Zimermanne Castro Santos^{ID}

University of Hamburg, Hamburg, Germany

A. Albrecht^{ID}, S. Albrecht^{ID}, M. Antonello^{ID}, S. Bein^{ID}, L. Benato^{ID}, M. Bonanomi^{ID},
P. Connor^{ID}, K. De Leo^{ID}, M. Eich, K. El Morabit^{ID}, Y. Fischer^{ID}, A. Fröhlich, C. Garbers^{ID},
E. Garutti^{ID}, A. Grohsjean^{ID}, M. Hajheidari, J. Haller^{ID}, A. Hinzmann^{ID}, H.R. Jabusch^{ID},
G. Kasieczka^{ID}, P. Keicher, R. Klanner^{ID}, W. Korcari^{ID}, T. Kramer^{ID}, V. Kutzner^{ID}, F. Labe^{ID},
J. Lange^{ID}, A. Lobanov^{ID}, C. Matthies^{ID}, A. Mehta^{ID}, L. Moureaux^{ID}, M. Mrowietz,
A. Nigamova^{ID}, Y. Nissan, A. Paasch^{ID}, K.J. Pena Rodriguez^{ID}, T. Quadfasel^{ID}, M. Rieger^{ID},
D. Savoiu^{ID}, J. Schindler^{ID}, P. Schleper^{ID}, M. Schröder^{ID}, J. Schwandt^{ID}, M. Sommerhalder^{ID},
H. Stadie^{ID}, G. Steinbrück^{ID}, A. Tews, M. Wolf^{ID}

Karlsruher Institut fuer Technologie, Karlsruhe, Germany

S. Brommer^{ID}, M. Burkart, E. Butz^{ID}, T. Chwalek^{ID}, A. Dierlamm^{ID}, A. Droll,
N. Faltermann^{ID}, M. Giffels^{ID}, A. Gottmann^{ID}, F. Hartmann^{ID}²⁶, M. Horzela^{ID}, U. Husemann^{ID},
M. Klute^{ID}, R. Koppenhöfer^{ID}, M. Link, A. Lintuluoto^{ID}, S. Maier^{ID}, S. Mitra^{ID}, Th. Müller^{ID},
M. Neukum, M. Oh^{ID}, G. Quast^{ID}, K. Rabbertz^{ID}, I. Shvetsov^{ID}, H.J. Simonis^{ID}, N. Trevisani^{ID},
R. Ulrich^{ID}, J. van der Linden^{ID}, R.F. Von Cube^{ID}, M. Wassmer^{ID}, S. Wieland^{ID}, R. Wolf^{ID},
S. Wunsch, X. Zuo^{ID}

Institute of Nuclear and Particle Physics (INPP), NCSR Demokritos, Aghia Paraskevi, Greece

G. Anagnostou, P. Assiouras^{ID}, G. Daskalakis^{ID}, A. Kyriakis, A. Stakia^{ID}

National and Kapodistrian University of Athens, Athens, Greece

D. Karasavvas, P. Kontaxakis , G. Melachroinos, A. Panagiotou, I. Papavergou ,
I. Paraskevas , N. Saoulidou , K. Theofilatos , E. Tziaferi , K. Vellidis , I. Zisopoulos

National Technical University of Athens, Athens, Greece

G. Bakas , T. Chatzistavrou, G. Karapostoli , K. Kousouris , I. Papakrivopoulos ,
E. Siamarkou, G. Tsipolitis, A. Zacharopoulou

University of Ioánnina, Ioánnina, Greece

K. Adamidis, I. Bestintzanos, I. Evangelou , C. Foudas, P. Gianneios , C. Kamtsikis,
P. Katsoulis, P. Kokkas , P.G. Kosmoglou Kioseoglou , N. Manthos , I. Papadopoulos ,
J. Strologas

MTA-ELTE Lendület CMS Particle and Nuclear Physics Group, Eötvös Loránd University, Budapest, Hungary

M. Csand , K. Farkas , M.M.A. Gadallah ²⁷, P. Major , K. Mandal , G. Pasztor ,
A.J. Radl ²⁸, O. Suranyi , G.I. Veres

Wigner Research Centre for Physics, Budapest, Hungary

M. Bartok ²⁹, C. Hajdu , D. Horvath ^{30,31}, F. Sikler , V. Veszpremi

Institute of Nuclear Research ATOMKI, Debrecen, Hungary

G. Bencze, S. Czellar, J. Karancsi ²⁹, J. Molnar, Z. Szillasi

Institute of Physics, University of Debrecen, Debrecen, Hungary

P. Raics, B. Ujvari ³², G. Zilizi

Karoly Robert Campus, MATE Institute of Technology, Gyongyos, Hungary

T. Csorgo ²⁸, F. Nemes ²⁸, T. Novak

Punjab University, Chandigarh, India

J. Babbar , S. Bansal , S.B. Beri, V. Bhatnagar , G. Chaudhary , S. Chauhan ,
N. Dhingra ³³, R. Gupta, A. Kaur , A. Kaur , H. Kaur , M. Kaur , S. Kumar ,
P. Kumari , M. Meena , K. Sandeep , T. Sheokand, J.B. Singh ³⁴, A. Singla

University of Delhi, Delhi, India

A. Ahmed , A. Bhardwaj , A. Chhetri , B.C. Choudhary , A. Kumar , M. Naimuddin ,
K. Ranjan , S. Saumya

Saha Institute of Nuclear Physics, HBNI, Kolkata, India

S. Baradia , S. Barman ³⁵, S. Bhattacharya , D. Bhowmik, S. Dutta , S. Dutta,
B. Gomber ³⁶, P. Palit , G. Saha , B. Sahu ³⁶, S. Sarkar

Indian Institute of Technology Madras, Madras, India

P.K. Behera , S.C. Behera , S. Chatterjee , P. Jana , P. Kalbhor , J.R. Komaragiri ³⁷,
D. Kumar ³⁷, M. Mohammad Mobassir Ameen , A. Muhammad , L. Panwar ³⁷,
R. Pradhan , P.R. Pujahari , N.R. Saha , A. Sharma , A.K. Sikdar , S. Verma

Tata Institute of Fundamental Research-A, Mumbai, IndiaT. Aziz, I. Das^{1D}, S. Dugad, M. Kumar^{1D}, G.B. Mohanty^{1D}, P. Suryadevara**Tata Institute of Fundamental Research-B, Mumbai, India**A. Bala^{1D}, S. Banerjee^{1D}, M. Guchait^{1D}, S. Karmakar^{1D}, S. Kumar^{1D}, G. Majumder^{1D}, K. Mazumdar^{1D}, S. Mukherjee^{1D}, A. Thachayath^{1D}**National Institute of Science Education and Research, An OCC of Homi Bhabha National Institute, Bhubaneswar, Odisha, India**S. Bahinipati^{1D}³⁸, A.K. Das, C. Kar^{1D}, D. Maity^{1D}³⁹, P. Mal^{1D}, T. Mishra^{1D}, V.K. Muraleedharan Nair Bindhu^{1D}³⁹, K. Naskar^{1D}³⁹, A. Nayak^{1D}³⁹, P. Sadangi, P. Saha^{1D}, S.K. Swain, S. Varghese^{1D}³⁹, D. Vats^{1D}³⁹**Indian Institute of Science Education and Research (IISER), Pune, India**A. Alpana^{1D}, S. Dube^{1D}, B. Kansal^{1D}, A. Laha^{1D}, S. Pandey^{1D}, A. Rastogi^{1D}, S. Sharma^{1D}**Isfahan University of Technology, Isfahan, Iran**H. Bakhshiansohi^{1D}^{40,41}, E. Khazaie^{1D}⁴¹, M. Zeinali^{1D}⁴²**Institute for Research in Fundamental Sciences (IPM), Tehran, Iran**S. Chenarani^{1D}⁴³, S.M. Etesami^{1D}, M. Khakzad^{1D}, M. Mohammadi Najafabadi^{1D}**University College Dublin, Dublin, Ireland**M. Grunewald^{1D}**INFN Sezione di Bari^a, Università di Bari^b, Politecnico di Bari^c, Bari, Italy**M. Abbrescia^{1D}^{a,b}, R. Aly^{1D}^{a,b,44}, C. Aruta^{1D}^{a,b}, A. Colaleo^{1D}^a, D. Creanza^{1D}^{a,c}, B. D' Anzi^{1D}^{a,b}, N. De Filippis^{1D}^{a,c}, M. De Palma^{1D}^{a,b}, A. Di Florio^{1D}^{a,b}, W. Elmetenawee^{1D}^{a,b}, L. Fiore^{1D}^a, G. Iaselli^{1D}^{a,c}, G. Maggi^{1D}^{a,c}, M. Maggi^{1D}^a, I. Margjeka^{1D}^{a,b}, V. Mastrapasqua^{1D}^{a,b}, S. My^{1D}^{a,b}, S. Nuzzo^{1D}^{a,b}, A. Pellecchia^{1D}^{a,b}, A. Pompili^{1D}^{a,b}, G. Pugliese^{1D}^{a,c}, R. Radogna^{1D}^a, D. Ramos^{1D}^a, A. Ranieri^{1D}^a, L. Silvestris^{1D}^a, F.M. Simone^{1D}^{a,b}, Ü. Sözbilir^{1D}^a, A. Stamerra^{1D}^a, R. Venditti^{1D}^a, P. Verwilligen^{1D}^a, A. Zaza^{1D}^{a,b}**INFN Sezione di Bologna^a, Università di Bologna^b, Bologna, Italy**G. Abbiendi^{1D}^a, C. Battilana^{1D}^{a,b}, D. Bonacorsi^{1D}^{a,b}, L. Borgonovi^{1D}^a, P. Capiluppi^{1D}^{a,b}, A. Castro^{1D}^{a,b}, F.R. Cavallo^{1D}^a, M. Cuffiani^{1D}^{a,b}, G.M. Dallavalle^{1D}^a, T. Diotalevi^{1D}^{a,b}, F. Fabbri^{1D}^a, A. Fanfani^{1D}^{a,b}, D. Fasanella^{1D}^{a,b}, P. Giacomelli^{1D}^a, L. Giommi^{1D}^{a,b}, C. Grandi^{1D}^a, L. Guiducci^{1D}^{a,b}, S. Lo Meo^{1D}^{a,45}, L. Lunerti^{1D}^{a,b}, S. Marcellini^{1D}^a, G. Masetti^{1D}^a, F.L. Navarria^{1D}^{a,b}, A. Perrotta^{1D}^a, F. Primavera^{1D}^{a,b}, A.M. Rossi^{1D}^{a,b}, T. Rovelli^{1D}^{a,b}, G.P. Siroli^{1D}^{a,b}**INFN Sezione di Catania^a, Università di Catania^b, Catania, Italy**S. Costa^{1D}^{a,b,46}, A. Di Mattia^{1D}^a, R. Potenza^{a,b}, A. Tricomi^{1D}^{a,b,46}, C. Tuve^{1D}^{a,b}

INFN Sezione di Firenze^a, Università di Firenze^b, Firenze, Italy

G. Barbagli ^a, G. Bardelli ^{a,b}, B. Camaiani ^{a,b}, A. Cassese ^a, R. Ceccarelli ^{a,b}, V. Ciulli ^{a,b}, C. Civinini ^a, R. D'Alessandro ^{a,b}, E. Focardi ^{a,b}, G. Latino ^{a,b}, P. Lenzi ^{a,b}, M. Lizzo ^{a,b}, M. Meschini ^a, S. Paoletti ^a, G. Sguazzoni ^a, L. Viliani ^a

INFN Laboratori Nazionali di Frascati, Frascati, Italy

L. Benussi , S. Bianco , S. Meola 47, D. Piccolo 

INFN Sezione di Genova^a, Università di Genova^b, Genova, Italy

P. Chatagnon ^a, F. Ferro ^a, E. Robutti ^a, S. Tosi ^{a,b}

INFN Sezione di Milano-Bicocca^a, Università di Milano-Bicocca^b, Milano, Italy

A. Benaglia ^a, G. Boldrini ^a, F. Brivio ^{a,b}, F. Cetorelli ^{a,b}, F. De Guio ^{a,b}, M.E. Dinardo ^{a,b}, P. Dini ^a, S. Gennai ^a, A. Ghezzi ^{a,b}, P. Govoni ^{a,b}, L. Guzzi ^{a,b}, M.T. Lucchini ^{a,b}, M. Malberti ^a, S. Malvezzi ^a, A. Massironi ^a, D. Menasce ^a, L. Moroni ^a, M. Paganoni ^{a,b}, D. Pedrini ^a, B.S. Pinolini^a, S. Ragazzi ^{a,b}, N. Redaelli ^a, T. Tabarelli de Fatis ^{a,b}, D. Zuolo ^{a,b}

INFN Sezione di Napoli^a, Università di Napoli ‘Federico II’^b, Napoli, Italy; Università della Basilicata^c, Potenza, Italy; Università G. Marconi^d, Roma, Italy

S. Buontempo ^a, A. Cagnotta ^{a,b}, F. Carnevali^{a,b}, N. Cavallo ^{a,c}, A. De Iorio ^{a,b}, F. Fabozzi ^{a,c}, A.O.M. Iorio ^{a,b}, L. Lista ^{a,b,48}, P. Paolucci ^{a,26}, B. Rossi ^a, C. Sciacca ^{a,b}

INFN Sezione di Padova^a, Università di Padova^b, Padova, Italy; Università di Trento^c, Trento, Italy

R. Ardino^a, P. Azzi ^a, N. Bacchetta ^{a,49}, D. Bisello ^{a,b}, P. Bortignon ^a, A. Bragagnolo ^{a,b}, R. Carlin ^{a,b}, P. Checchia ^a, T. Dorigo ^a, U. Gasparini ^{a,b}, G. Grossi ^a, L. Layer^{a,50}, E. Lusiani ^a, M. Margoni ^{a,b}, A.T. Meneguzzo ^{a,b}, M. Migliorini ^{a,b}, F. Montecassiano ^a, J. Pazzini ^{a,b}, P. Ronchese ^{a,b}, R. Rossin ^{a,b}, F. Simonetto ^{a,b}, G. Strong ^a, M. Tosi ^{a,b}, A. Triassi ^{a,b}, S. Ventura ^a, H. Yarai^{a,b}, M. Zanetti ^{a,b}, P. Zotto ^{a,b}, A. Zucchetta ^{a,b}, G. Zumerle ^{a,b}

INFN Sezione di Pavia^a, Università di Pavia^b, Pavia, Italy

S. Abu Zeid ^{a,51}, C. Aimè ^{a,b}, A. Braghieri ^a, S. Calzaferri ^{a,b}, D. Fiorina ^{a,b}, P. Montagna ^{a,b}, V. Re ^a, C. Riccardi ^{a,b}, P. Salvini ^a, I. Vai ^{a,b}, P. Vitulo ^{a,b}

INFN Sezione di Perugia^a, Università di Perugia^b, Perugia, Italy

P. Asenov ^{a,52}, G.M. Bilei ^a, D. Ciangottini ^{a,b}, L. Fanò ^{a,b}, M. Magherini ^{a,b}, G. Mantovani^{a,b}, V. Mariani ^{a,b}, M. Menichelli ^a, F. Moscatelli ^{a,52}, A. Piccinelli ^{a,b}, M. Presilla ^{a,b}, A. Rossi ^{a,b}, A. Santocchia ^{a,b}, D. Spiga ^a, T. Tedeschi ^{a,b}

INFN Sezione di Pisa^a, Università di Pisa^b, Scuola Normale Superiore di Pisa^c, Pisa, Italy; Università di Siena^d, Siena, Italy

P. Azzurri , G. Bagliesi , R. Bhattacharya , L. Bianchini , T. Boccali , E. Bossini , D. Bruschini , R. Castaldi , M.A. Ciocci , V. D'Amante , R. Dell'Orso , S. Donato , A. Giassi , F. Ligabue , D. Matos Figueiredo , A. Messineo , M. Musich , F. Palla , S. Parolia , G. Ramirez-Sanchez , A. Rizzi , G. Rolandi , S. Roy Chowdhury , T. Sarkar , A. Scribano , P. Spagnolo , R. Tenchini , G. Tonelli , N. Turini , A. Venturi , P.G. Verdini 

INFN Sezione di Roma^a, Sapienza Università di Roma^b, Roma, Italy

P. Barria , M. Campana , F. Cavallari , L. Cunqueiro Mendez , D. Del Re , E. Di Marco , M. Diemoz , F. Errico , E. Longo , P. Meridiani , J. Mijuskovic , G. Organtini , F. Pandolfi , R. Paramatti , C. Quaranta , S. Rahatlou , C. Rovelli , F. Santanastasio , L. Soffi , R. Tramontano 

INFN Sezione di Torino^a, Università di Torino^b, Torino, Italy; Università del Piemonte Orientale^c, Novara, Italy

N. Amapane , R. Arcidiacono , S. Argiro , M. Arneodo , N. Bartosik , R. Bellan , A. Bellora , C. Biino , N. Cartiglia , M. Costa , R. Covarelli , N. Demaria , L. Finco , M. Grippo , B. Kiani , F. Legger , F. Luongo , C. Mariotti , S. Maselli , A. Mecca , E. Migliore , M. Monteno , R. Mulargia , M.M. Obertino , G. Ortona , L. Pacher , N. Pastrone , M. Pelliccioni , M. Ruspa , K. Shchelina , F. Siviero , V. Sola , A. Solano , D. Soldi , A. Staiano , C. Tarricone , M. Tornago , D. Trocino , G. Umoret , A. Vagnerini , E. Vlasov

INFN Sezione di Trieste^a, Università di Trieste^b, Trieste, Italy

S. Belforte , V. Candelise , M. Casarsa , F. Cossutti , G. Della Ricca , G. Sorrentino 

Kyungpook National University, Daegu, Korea

S. Dogra , C. Huh , B. Kim , D.H. Kim , J. Kim , J. Lee , S.W. Lee , C.S. Moon , Y.D. Oh , S.I. Pak , M.S. Ryu , S. Sekmen , Y.C. Yang 

Chonnam National University, Institute for Universe and Elementary Particles, Kwangju, Korea

G. Bak , P. Gwak , H. Kim , D.H. Moon 

Hanyang University, Seoul, Korea

E. Asilar , T.J. Kim , J. Park 

Korea University, Seoul, Korea

S. Choi , S. Han, B. Hong , K. Lee, K.S. Lee , J. Lim, J. Park, S.K. Park, J. Yoo 

Kyung Hee University, Department of Physics, Seoul, Korea

J. Goh 

Sejong University, Seoul, KoreaH. S. Kim[✉], Y. Kim, S. Lee**Seoul National University, Seoul, Korea**J. Almond, J.H. Bhyun, J. Choi[✉], S. Jeon[✉], W. Jun[✉], J. Kim[✉], J.S. Kim, S. Ko[✉], H. Kwon[✉], H. Lee[✉], S. Lee, B.H. Oh[✉], S.B. Oh[✉], H. Seo[✉], U.K. Yang, I. Yoon[✉]**University of Seoul, Seoul, Korea**W. Jang[✉], D.Y. Kang, Y. Kang[✉], D. Kim[✉], S. Kim[✉], B. Ko, J.S.H. Lee[✉], Y. Lee[✉], J.A. Merlin, I.C. Park[✉], Y. Roh, Watson, I.J.[✉], S. Yang[✉]**Yonsei University, Department of Physics, Seoul, Korea**S. Ha[✉], H.D. Yoo[✉]**Sungkyunkwan University, Suwon, Korea**M. Choi[✉], M.R. Kim[✉], H. Lee, Y. Lee[✉], I. Yu[✉]**College of Engineering and Technology, American University of the Middle East (AUM), Dasman, Kuwait**T. Beyrouthy, Y. Maghrbi[✉]**Riga Technical University, Riga, Latvia**K. Dreimanis[✉], A. Gaile[✉], G. Pikurs, A. Potrebko[✉], M. Seidel[✉], V. Veckalns[✉]⁵⁴**University of Latvia (LU), Riga, Latvia**N.R. Strautnieks[✉]**Vilnius University, Vilnius, Lithuania**M. Ambrozas[✉], A. Juodagalvis[✉], A. Rinkevicius[✉], G. Tamulaitis[✉]**National Centre for Particle Physics, Universiti Malaya, Kuala Lumpur, Malaysia**N. Bin Norjoharuddeen[✉], I. Yusuff[✉]⁵⁵, Z. Zolkapli**Universidad de Sonora (UNISON), Hermosillo, Mexico**J.F. Benitez[✉], A. Castaneda Hernandez[✉], H.A. Encinas Acosta, L.G. Gallegos Maríñez, M. León Coello[✉], J.A. Murillo Quijada[✉], A. Sehrawat[✉], L. Valencia Palomo[✉]**Centro de Investigacion y de Estudios Avanzados del IPN, Mexico City, Mexico**G. Ayala[✉], H. Castilla-Valdez[✉], E. De La Cruz-Burelo[✉], I. Heredia-De La Cruz[✉]⁵⁶, R. Lopez-Fernandez[✉], C.A. Mondragon Herrera, D.A. Perez Navarro[✉], A. Sánchez Hernández[✉]**Universidad Iberoamericana, Mexico City, Mexico**C. Oropeza Barrera[✉], M. Ramírez García[✉]

Benemerita Universidad Autonoma de Puebla, Puebla, MexicoI. Pedraza , H.A. Salazar Ibarguen , C. Uribe Estrada **University of Montenegro, Podgorica, Montenegro**I. Bubanja, N. Raicevic **University of Canterbury, Christchurch, New Zealand**P.H. Butler **National Centre for Physics, Quaid-I-Azam University, Islamabad, Pakistan**A. Ahmad , M.I. Asghar, A. Awais , M.I.M. Awan, H.R. Hoorani , W.A. Khan **AGH University of Science and Technology Faculty of Computer Science,
Electronics and Telecommunications, Krakow, Poland**V. Avati, L. Grzanka , M. Malawski **National Centre for Nuclear Research, Swierk, Poland**H. Bialkowska , M. Bluj , B. Boimska , M. Górski , M. Kazana , M. Szleper ,
P. Zalewski **Institute of Experimental Physics, Faculty of Physics, University of Warsaw,
Warsaw, Poland**K. Bunkowski , K. Doroba , A. Kalinowski , M. Konecki , J. Krolikowski **Laboratório de Instrumentação e Física Experimental de Partículas, Lisboa,
Portugal**M. Araujo , D. Bastos , C. Beirão Da Cruz E Silva , A. Boletti , M. Bozzo , P. Faccioli ,
M. Gallinaro , J. Hollar , N. Leonardo , T. Niknejad , M. Pisano , J. Seixas , J. Varela **Faculty of Physics, University of Belgrade, Belgrade, Serbia**P. Adzic , P. Milenovic **VINCA Institute of Nuclear Sciences, University of Belgrade, Belgrade,
Serbia**M. Dordevic , J. Milosevic , V. Rekovic**Centro de Investigaciones Energéticas Medioambientales y Tecnológicas
(CIEMAT), Madrid, Spain**M. Aguilar-Benitez, J. Alcaraz Maestre , M. Barrio Luna, Cristina F. Bedoya , M. Cepeda ,
M. Cerrada , N. Colino , B. De La Cruz , A. Delgado Peris , D. Fernández Del Val ,
J.P. Fernández Ramos , J. Flix , M.C. Fouz , O. Gonzalez Lopez , S. Goy Lopez ,
J.M. Hernandez , M.I. Josa , J. León Holgado , D. Moran , Á. Navarro Tobar ,
C. Perez Dengra , A. Pérez-Calero Yzquierdo , J. Puerta Pelayo , I. Redondo ,
D.D. Redondo Ferrero , L. Romero, S. Sánchez Navas , L. Urda Gómez ,
J. Vazquez Escobar , C. Willmott

Universidad Autónoma de Madrid, Madrid, SpainJ.F. de Trocóniz **Universidad de Oviedo, Instituto Universitario de Ciencias y Tecnologías Espaciales de Asturias (ICTEA), Oviedo, Spain**

B. Alvarez Gonzalez , J. Cuevas , J. Fernandez Menendez , S. Folgueras ,
 I. Gonzalez Caballero , J.R. González Fernández , E. Palencia Cortezon ,
 C. Ramón Álvarez , V. Rodríguez Bouza , A. Soto Rodríguez , A. Trapote ,
 C. Vico Villalba , P. Vischia 

Instituto de Física de Cantabria (IFCA), CSIC-Universidad de Cantabria, Santander, Spain

S. Blanco Fernández , J.A. Brochero Cifuentes , I.J. Cabrillo , A. Calderon ,
 J. Duarte Campderros , M. Fernandez , C. Fernandez Madrazo , G. Gomez ,
 C. Lasaosa García , C. Martinez Rivero , P. Martinez Ruiz del Arbol , F. Matorras ,
 P. Matorras Cuevas , E. Navarrete Ramos, J. Piedra Gomez , C. Prieels, L. Scodellaro ,
 I. Vila , J.M. Vizan Garcia 

University of Colombo, Colombo, Sri LankaM.K. Jayananda , B. Kailasapathy ⁵⁷, D.U.J. Sonnadara , D.D.C. Wickramarathna **University of Ruhuna, Department of Physics, Matara, Sri Lanka**W.G.D. Dharmaratna , K. Liyanage , N. Perera , N. Wickramage **CERN, European Organization for Nuclear Research, Geneva, Switzerland**

D. Abbaneo , E. Auffray , G. Auzinger , J. Baechler, D. Barney , A. Bermúdez Martínez ,
 M. Bianco , B. Bilin , A.A. Bin Anuar , A. Bocci , E. Brondolin , C. Caillol ,
 T. Camporesi , G. Cerminara , N. Chernyavskaya , M. Cipriani , D. d'Enterria ,
 A. Dabrowski , A. David , A. De Roeck , M.M. Defranchis , M. Deile , M. Dobson ,
 F. Fallavollita ⁵⁸, L. Forthomme , G. Franzoni , W. Funk , S. Giani, D. Gigi, K. Gill ,
 F. Glege , L. Gouskos , M. Haranko , J. Hegeman , T. James , J. Kieseler ,
 N. Kratochwil , S. Laurila , P. Lecoq , E. Leutgeb , C. Lourenço , B. Maier ,
 L. Malgeri , M. Mannelli , A.C. Marini , F. Meijers , S. Mersi , E. Meschi ,
 V. Milosevic , F. Moortgat , M. Mulders , S. Orfanelli, F. Pantaleo , M. Peruzzi ,
 A. Petrilli , G. Petrucciani , A. Pfeiffer , M. Pierini , D. Piparo , H. Qu , D. Rabady ,
 G. Reales Gutiérrez, M. Rovere , H. Sakulin , S. Scarfi , M. Selvaggi , A. Sharma ,
 P. Silva , P. Sphicas ⁵⁹, A.G. Stahl Leiton , A. Steen , S. Summers , D. Treille ,
 P. Tropea , A. Tsirou, D. Walter , J. Wanczyk ⁶⁰, K.A. Wozniak , P. Zehetner, P. Zejdl ,
 W.D. Zeuner

Paul Scherrer Institut, Villigen, Switzerland

T. Bevilacqua ⁶¹, L. Caminada ⁶¹, A. Ebrahimi , W. Erdmann , R. Horisberger ,
 Q. Ingram , H.C. Kaestli , D. Kotlinski , C. Lange , M. Missiroli  ⁶¹, L. Noehte  ⁶¹,
 T. Rohe 

ETH Zurich — Institute for Particle Physics and Astrophysics (IPA), Zurich, Switzerland

T.K. Aarrestad , K. Androsov ⁶⁰, M. Backhaus , A. Calandri , K. Datta , A. De Cosa , G. Dissertori , M. Dittmar, M. Donegà , F. Eble , M. Galli , K. Gedia , F. Glessgen , C. Grab , D. Hits , W. Lustermann , A.-M. Lyon , R.A. Manzoni , L. Marchese , C. Martin Perez , A. Mascellani ⁶⁰, F. Nessi-Tedaldi , F. Pauss , V. Perovic , S. Pigazzini , M.G. Ratti , M. Reichmann , C. Reissel , T. Reitenspiess , B. Ristic , F. Riti , D. Ruini, D.A. Sanz Becerra , R. Seidita , J. Steggemann ⁶⁰, D. Valsecchi , R. Wallny

Universität Zürich, Zurich, Switzerland

C. Amsler ⁶², P. Bärtschi , C. Botta , D. Brzhechko, M.F. Canelli , K. Cormier , A. De Wit , R. Del Burgo, J.K. Heikkilä , M. Huwiler , W. Jin , A. Jofrehei , B. Kilminster , S. Leontsinis , S.P. Liechti , A. Macchiolo , P. Meiring , V.M. Mikuni , U. Molinatti , I. Neutelings , A. Reimers , P. Robmann, S. Sanchez Cruz , K. Schweiger , M. Senger , Y. Takahashi

National Central University, Chung-Li, Taiwan

C. Adloff ⁶³, C.M. Kuo, W. Lin, P.K. Rout , P.C. Tiwari ³⁷, S.S. Yu

National Taiwan University (NTU), Taipei, Taiwan

L. Ceard, Y. Chao , K.F. Chen , P.s. Chen, W.-S. Hou , Y.w. Kao, R. Khurana, G. Kole , Y.y. Li , R.-S. Lu , E. Paganis , A. Psallidas, J. Thomas-Wilsker , H.y. Wu, E. Yazgan

Chulalongkorn University, Faculty of Science, Department of Physics, Bangkok, Thailand

C. Asawatangtrakuldee , N. Srimanobhas , V. Wachirapusanand

Çukurova University, Physics Department, Science and Art Faculty, Adana, Turkey

D. Agyel , F. Boran , Z.S. Demiroglu , F. Dolek , I. Dumanoglu ⁶⁴, E. Eskut , Y. Guler ⁶⁵, E. Gurpinar Guler ⁶⁵, C. Isik , O. Kara, A. Kayis Topaksu , U. Kiminsu , G. Onengut , K. Ozdemir ⁶⁶, A. Polatoz , B. Tali ⁶⁷, U.G. Tok , S. Turkcapar , E. Uslan , I.S. Zorbakir

Middle East Technical University, Physics Department, Ankara, Turkey

K. Ocalan ⁶⁸, M. Yalvac ⁶⁹

Bogazici University, Istanbul, Turkey

B. Akgun , I.O. Atakisi , E. Gülmез , M. Kaya ⁷⁰, O. Kaya ⁷¹, S. Tekten ⁷²

Istanbul Technical University, Istanbul, Turkey

A. Cakir , K. Cankocak ⁶⁴, Y. Komurcu , S. Sen ⁷³

Istanbul University, Istanbul, Turkey

O. Aydilek , S. Cerci ⁶⁷, V. Epshteyn , B. Hacisahinoglu , I. Hos ⁷⁴, B. Isildak ⁷⁵,
B. Kaynak , S. Ozkorucuklu , H. Sert , C. Simsek , D. Sunar Cerci ⁶⁷, C. Zorbilmez 

Institute for Scintillation Materials of National Academy of Science of Ukraine, Kharkiv, Ukraine

A. Boyaryntsev, B. Grynyov 

National Science Centre, Kharkiv Institute of Physics and Technology, Kharkiv, Ukraine

L. Levchuk 

University of Bristol, Bristol, United Kingdom

D. Anthony , J.J. Brooke , A. Bundock , E. Clement , D. Cussans , H. Flacher ,
M. Glowacki, J. Goldstein , H.F. Heath , L. Kreczko , B. Krikler , S. Paramesvaran ,
S. Seif El Nasr-Storey, V.J. Smith , N. Stylianou ⁷⁶, K. Walkingshaw Pass, R. White 

Rutherford Appleton Laboratory, Didcot, United Kingdom

A.H. Ball, K.W. Bell , A. Belyaev ⁷⁷, C. Brew , R.M. Brown , D.J.A. Cockerill ,
C. Cooke , K.V. Ellis, K. Harder , S. Harper , M.-L. Holmberg ⁷⁸, Sh. Jain , J. Linacre ,
K. Manolopoulos, D.M. Newbold , E. Olaiya, D. Petyt , T. Reis , G. Salvi , T. Schuh,
C.H. Shepherd-Themistocleous , I.R. Tomalin, T. Williams 

Imperial College, London, United Kingdom

R. Bainbridge , P. Bloch , C.E. Brown , O. Buchmuller, V. Cacchio,
C.A. Carrillo Montoya , V. Cepaitis , G.S. Chahal ⁷⁹, D. Colling , J.S. Dancu,
P. Dauncey , G. Davies , J. Davies, M. Della Negra , S. Fayer, G. Fedi , G. Hall ,
M.H. Hassanshahi , A. Howard, G. Iles , J. Langford , L. Lyons , A.-M. Magnan ,
S. Malik, A. Martelli , M. Mieskolainen , J. Nash ⁸⁰, M. Pesaresi, B.C. Radburn-Smith ,
A. Richards, A. Rose , C. Seez , R. Shukla , A. Tapper , K. Uchida , G.P. Uttley ,
L.H. Vage, T. Virdee , M. Vojinovic , N. Wardle , D. Winterbottom

Brunel University, Uxbridge, United Kingdom

K. Coldham, J.E. Cole , A. Khan, P. Kyberd , I.D. Reid 

Baylor University, Waco, Texas, U.S.A.

S. Abdullin , A. Brinkerhoff , B. Caraway , J. Dittmann , K. Hatakeyama ,
J. Hiltbrand , A.R. Kanuganti , B. McMaster , M. Saunders , S. Sawant ,
C. Sutantawibul , M. Toms , J. Wilson 

Catholic University of America, Washington, DC, U.S.A.

R. Bartek , A. Dominguez , C. Huerta Escamilla, A.E. Simsek , R. Uniyal ,
A.M. Vargas Hernandez 

The University of Alabama, Tuscaloosa, Alabama, U.S.A.

R. Chudasama^{1D}, S.I. Cooper^{1D}, S.V. Gleyzer^{1D}, C.U. Perez^{1D}, P. Rumerio^{1D}⁸¹, E. Usai^{1D},
C. West^{1D}

Boston University, Boston, Massachusetts, U.S.A.

A. Akpinar^{1D}, A. Albert^{1D}, D. Arcaro^{1D}, C. Cosby^{1D}, Z. Demiragli^{1D}, C. Erice^{1D}, E. Fontanesi^{1D},
D. Gastler^{1D}, J. Rohlf^{1D}, K. Salyer^{1D}, D. Sperka^{1D}, D. Spitzbart^{1D}, I. Suarez^{1D}, A. Tsatsos^{1D},
S. Yuan^{1D}

Brown University, Providence, Rhode Island, U.S.A.

G. Benelli^{1D}, X. Coubez²¹, D. Cutts^{1D}, M. Hadley^{1D}, U. Heintz^{1D}, J.M. Hogan^{1D}⁸², T. Kwon^{1D},
G. Landsberg^{1D}, K.T. Lau^{1D}, D. Li^{1D}, J. Luo^{1D}, M. Narain^{1D}, N. Pervan^{1D}, S. Sagir^{1D}⁸³,
F. Simpson^{1D}, W.Y. Wong, X. Yan^{1D}, D. Yu^{1D}, W. Zhang

University of California, Davis, Davis, California, U.S.A.

S. Abbott^{1D}, J. Bonilla^{1D}, C. Brainerd^{1D}, R. Breedon^{1D}, M. Calderon De La Barca Sanchez^{1D},
M. Chertok^{1D}, M. Citron^{1D}, J. Conway^{1D}, P.T. Cox^{1D}, R. Erbacher^{1D}, G. Haza^{1D}, F. Jensen^{1D},
O. Kukral^{1D}, G. Mocellin^{1D}, M. Mulhearn^{1D}, D. Pellett^{1D}, B. Regnery^{1D}, W. Wei, Y. Yao^{1D},
F. Zhang^{1D}

University of California, Los Angeles, California, U.S.A.

M. Bachtis^{1D}, R. Cousins^{1D}, A. Datta^{1D}, J. Hauser^{1D}, M. Ignatenko^{1D}, M.A. Iqbal^{1D}, T. Lam^{1D},
E. Manca^{1D}, W.A. Nash^{1D}, D. Saltzberg^{1D}, B. Stone^{1D}, V. Valuev^{1D}

University of California, Riverside, Riverside, California, U.S.A.

R. Clare^{1D}, M. Gordon, G. Hanson^{1D}, W. Si^{1D}, S. Wimpenny^{1D}[†]

University of California, San Diego, La Jolla, California, U.S.A.

J.G. Branson, S. Cittolin, S. Cooperstein^{1D}, D. Diaz^{1D}, J. Duarte^{1D}, R. Gerosa^{1D}, L. Giannini^{1D},
J. Guiang^{1D}, R. Kansal^{1D}, V. Krutelyov^{1D}, R. Lee^{1D}, J. Letts^{1D}, M. Masciovecchio^{1D},
F. Mokhtar^{1D}, M. Pieri^{1D}, M. Quinnan^{1D}, B.V. Sathia Narayanan^{1D}, V. Sharma^{1D}, M. Tadel^{1D},
E. Vourliotis^{1D}, F. Würthwein^{1D}, Y. Xiang^{1D}, A. Yagil^{1D}

University of California, Santa Barbara — Department of Physics, Santa Barbara, California, U.S.A.

L. Brennan, C. Campagnari^{1D}, G. Collura^{1D}, A. Dorsett^{1D}, J. Incandela^{1D}, M. Kilpatrick^{1D},
J. Kim^{1D}, A.J. Li^{1D}, P. Masterson^{1D}, H. Mei^{1D}, M. Oshiro^{1D}, J. Richman^{1D}, U. Sarica^{1D},
R. Schmitz^{1D}, F. Setti^{1D}, J. Sheplock^{1D}, D. Stuart^{1D}, S. Wang^{1D}

California Institute of Technology, Pasadena, California, U.S.A.

A. Bornheim^{1D}, O. Cerri, A. Latorre, J.M. Lawhorn^{1D}, J. Mao^{1D}, H.B. Newman^{1D},
T. Q. Nguyen^{1D}, M. Spiropulu^{1D}, J.R. Vlimant^{1D}, C. Wang^{1D}, S. Xie^{1D}, R.Y. Zhu^{1D}

Carnegie Mellon University, Pittsburgh, Pennsylvania, U.S.A.

J. Alison^{1D}, S. An^{1D}, M.B. Andrews^{1D}, P. Bryant^{1D}, V. Dutta^{1D}, T. Ferguson^{1D}, A. Harilal^{1D},
C. Liu^{1D}, T. Mudholkar^{1D}, S. Murthy^{1D}, M. Paulini^{1D}, A. Roberts^{1D}, A. Sanchez^{1D}, W. Terrill^{1D}

University of Colorado Boulder, Boulder, Colorado, U.S.A.

J.P. Cumalat , W.T. Ford , A. Hassani , G. Karathanasis , E. MacDonald, N. Manganelli , F. Marini , A. Perloff , C. Savard , N. Schonbeck , K. Stenson , K.A. Ulmer , S.R. Wagner , N. Zipper

Cornell University, Ithaca, New York, U.S.A.

J. Alexander , S. Bright-Thonney , X. Chen , D.J. Cranshaw , J. Fan , X. Fan , D. Gadkari , S. Hogan , J. Monroy , J.R. Patterson , J. Reichert , M. Reid , A. Ryd , J. Thom , P. Wittich , R. Zou

Fermi National Accelerator Laboratory, Batavia, Illinois, U.S.A.

M. Albrow , M. Alyari , O. Amram , G. Apollinari , A. Apresyan , L.A.T. Bauer , D. Berry , J. Berryhill , P.C. Bhat , K. Burkett , J.N. Butler , A. Canepa , G.B. Cerati , H.W.K. Cheung , F. Chlebana , G. Cummings , J. Dickinson , I. Dutta , V.D. Elvira , Y. Feng , J. Freeman , A. Gandrakota , Z. Gecse , L. Gray , D. Green, S. Grünendahl , D. Guerrero , O. Gutsche , R.M. Harris , R. Heller , T.C. Herwig , J. Hirschauer , L. Horyn , B. Jayatilaka , S. Jindariani , M. Johnson , U. Joshi , T. Klijnsma , B. Klima , K.H.M. Kwok , S. Lammel , D. Lincoln , R. Lipton , T. Liu , C. Madrid , K. Maeshima , C. Mantilla , D. Mason , P. McBride , P. Merkel , S. Mrenna , S. Nahm , J. Ngadiuba , D. Noonan , V. Papadimitriou , N. Pastika , K. Pedro , C. Pena ⁸⁴, F. Ravera , A. Reinsvold Hall ⁸⁵, L. Ristori , E. Sexton-Kennedy , N. Smith , A. Soha , L. Spiegel , L. Taylor , S. Tkaczyk , N.V. Tran , L. Uplegger , E.W. Vaandering , I. Zoi

University of Florida, Gainesville, Florida, U.S.A.

P. Avery , D. Bourilkov , L. Cadamuro , P. Chang , V. Cherepanov , R.D. Field, E. Koenig , M. Kolosova , J. Konigsberg , A. Korytov , K.H. Lo, K. Matchev , N. Menendez , G. Mitselmakher , A. Muthirakalayil Madhu , N. Rawal , D. Rosenzweig , S. Rosenzweig , K. Shi , J. Wang

Florida State University, Tallahassee, Florida, U.S.A.

T. Adams , A. Al Kadhim , A. Askew , N. Bower , R. Habibullah , V. Hagopian , R. Hashmi , R.S. Kim , S. Kim , T. Kolberg , G. Martinez, H. Prosper , P.R. Prova, O. Viazlo , M. Wulansatiti , R. Yohay , J. Zhang

Florida Institute of Technology, Melbourne, Florida, U.S.A.

B. Alsufyani, M.M. Baarmand , S. Butalla , T. Elkafrawy ⁵¹, M. Hohlmann , R. Kumar Verma , M. Rahmani, F. Yumiceva 

University of Illinois at Chicago (UIC), Chicago, Illinois, U.S.A.

M.R. Adams , C. Bennett, R. Cavanaugh , S. Dittmer , O. Evdokimov , C.E. Gerber , D.J. Hofman , J.h. Lee , D. S. Lemos , A.H. Merrit , C. Mills , S. Nanda , G. Oh , D. Pilipovic , T. Roy , S. Rudrabhatla , M.B. Tonjes , N. Varelas , X. Wang , Z. Ye , J. Yoo

The University of Iowa, Iowa City, Iowa, U.S.A.

M. Alhusseini , D. Blend, K. Dilsiz ⁸⁶, L. Emediato , G. Karaman , O.K. Köseyan , J.-P. Merlo, A. Mestvirishvili ⁸⁷, J. Nachtman , O. Neogi, H. Ogul ⁸⁸, Y. Onel , A. Penzo , C. Snyder, E. Tiras ⁸⁹

Johns Hopkins University, Baltimore, Maryland, U.S.A.

B. Blumenfeld , L. Corcodilos , J. Davis , A.V. Gritsan , L. Kang , S. Kyriacou , P. Maksimovic , M. Roguljic , J. Roskes , S. Sekhar , M. Swartz , T.Á. Vámi

The University of Kansas, Lawrence, Kansas, U.S.A.

A. Abreu , L.F. Alcerro Alcerro , J. Anguiano , P. Baringer , A. Bean , Z. Flowers , J. King , G. Krintiras , M. Lazarovits , C. Le Mahieu , C. Lindsey, J. Marquez , N. Minafra , M. Murray , M. Nickel , M. Pitt , S. Popescu ⁹⁰, C. Rogan , C. Royon , R. Salvatico , S. Sanders , C. Smith , Q. Wang , G. Wilson

Kansas State University, Manhattan, Kansas, U.S.A.

B. Allmond , S. Duric, A. Ivanov , K. Kaadze , A. Kalogeropoulos , D. Kim, Y. Maravin , T. Mitchell, K. Nam, J. Natoli , D. Roy

University of Maryland, College Park, Maryland, U.S.A.

E. Adams , A. Baden , O. Baron, A. Belloni , A. Bethani , Y.m. Chen , S.C. Eno , N.J. Hadley , S. Jabeen , R.G. Kellogg , T. Koeth , Y. Lai , S. Lascio , A.C. Mignerey , S. Nabili , C. Palmer , C. Papageorgakis , L. Wang , K. Wong

Massachusetts Institute of Technology, Cambridge, Massachusetts, U.S.A.

J. Bendavid , W. Busza , I.A. Cali , Y. Chen , M. D'Alfonso , J. Eysermans , C. Freer , G. Gomez-Ceballos , M. Goncharov, P. Harris, D. Hoang, D. Kovalskyi , J. Krupa , L. Lavezzi , Y.-J. Lee , K. Long , C. Mironov , C. Paus , D. Rankin , C. Roland , G. Roland , S. Rothman , Z. Shi , G.S.F. Stephans , J. Wang, Z. Wang , B. Wyslouch , T. J. Yang

University of Minnesota, Minneapolis, Minnesota, U.S.A.

R.M. Chatterjee, B. Crossman , B.M. Joshi , C. Kapsiak , M. Krohn , D. Mahon , J. Mans , M. Revering , R. Rusack , R. Saradhy , N. Schroeder , N. Strobbe , M.A. Wadud

University of Mississippi, Oxford, Mississippi, U.S.A.

L.M. Cremaldi

University of Nebraska-Lincoln, Lincoln, Nebraska, U.S.A.

K. Bloom , M. Bryson, D.R. Claes , C. Fangmeier , F. Golf , C. Joo , I. Kravchenko , I. Reed , J.E. Siado , G.R. Snow [†], W. Tabb , A. Wightman , F. Yan , A.G. Zecchinelli

State University of New York at Buffalo, Buffalo, New York, U.S.A.

G. Agarwal¹⁰, H. Bandyopadhyay¹⁰, L. Hay¹⁰, I. Iashvili¹⁰, A. Kharchilava¹⁰, C. McLean¹⁰, M. Morris¹⁰, D. Nguyen¹⁰, J. Pekkanen¹⁰, S. Rappoccio¹⁰, H. Rejeb Sfar, A. Williams¹⁰

Northeastern University, Boston, Massachusetts, U.S.A.

G. Alverson¹⁰, E. Barberis¹⁰, Y. Haddad¹⁰, Y. Han¹⁰, A. Krishna¹⁰, J. Li¹⁰, G. Madigan¹⁰, B. Marzocchi¹⁰, D.M. Morse¹⁰, V. Nguyen¹⁰, T. Orimoto¹⁰, A. Parker¹⁰, L. Skinnari¹⁰, A. Tishelman-Charny¹⁰, B. Wang¹⁰, D. Wood¹⁰

Northwestern University, Evanston, Illinois, U.S.A.

S. Bhattacharya¹⁰, J. Bueghly, Z. Chen¹⁰, A. Gilbert¹⁰, K.A. Hahn¹⁰, Y. Liu¹⁰, D.G. Monk¹⁰, M.H. Schmitt¹⁰, A. Taliercio¹⁰, M. Velasco

University of Notre Dame, Notre Dame, Indiana, U.S.A.

R. Band¹⁰, R. Bucci, M. Cremonesi, A. Das¹⁰, R. Goldouzian¹⁰, M. Hildreth¹⁰, K. Hurtado Anampa¹⁰, C. Jessop¹⁰, K. Lannon¹⁰, J. Lawrence¹⁰, N. Loukas¹⁰, L. Lutton¹⁰, J. Mariano, N. Marinelli, I. Mcalister, T. McCauley¹⁰, C. Mcgrady¹⁰, K. Mohrman¹⁰, C. Moore¹⁰, Y. Musienko¹⁰¹², H. Nelson¹⁰, R. Ruchti¹⁰, A. Townsend¹⁰, M. Wayne¹⁰, H. Yockey, M. Zarucki¹⁰, L. Zygal¹⁰

The Ohio State University, Columbus, Ohio, U.S.A.

B. Bylsma, M. Carrigan¹⁰, L.S. Durkin¹⁰, C. Hill¹⁰, M. Joyce¹⁰, A. Lesauvage¹⁰, M. Nunez Ornelas¹⁰, K. Wei, B.L. Winer¹⁰, B. R. Yates¹⁰

Princeton University, Princeton, New Jersey, U.S.A.

F.M. Addesa¹⁰, H. Bouchamaoui¹⁰, P. Das¹⁰, G. Dezoort¹⁰, P. Elmer¹⁰, A. Frankenthal¹⁰, B. Greenberg¹⁰, N. Haubrich¹⁰, S. Higginbotham¹⁰, G. Kopp¹⁰, S. Kwan¹⁰, D. Lange¹⁰, A. Loeliger¹⁰, D. Marlow¹⁰, I. Ojalvo¹⁰, J. Olsen¹⁰, D. Stickland¹⁰, C. Tully¹⁰

University of Puerto Rico, Mayaguez, Puerto Rico, U.S.A.

S. Malik¹⁰

Purdue University, West Lafayette, Indiana, U.S.A.

A.S. Bakshi¹⁰, V.E. Barnes¹⁰, S. Chandra¹⁰, R. Chawla¹⁰, S. Das¹⁰, A. Gu¹⁰, L. Gutay, M. Jones¹⁰, A.W. Jung¹⁰, D. Kondratyev¹⁰, A.M. Koshy, M. Liu¹⁰, G. Negro¹⁰, N. Neumeister¹⁰, G. Paspalaki¹⁰, S. Piperov¹⁰, A. Purohit¹⁰, J.F. Schulte¹⁰, M. Stojanovic¹⁰¹⁵, J. Thieman¹⁰, F. Wang¹⁰, W. Xie¹⁰

Purdue University Northwest, Hammond, Indiana, U.S.A.

J. Dolen¹⁰, N. Parashar¹⁰, A. Pathak¹⁰

Rice University, Houston, Texas, U.S.A.

D. Acosta¹⁰, A. Baty¹⁰, T. Carnahan¹⁰, S. Dildick¹⁰, K.M. Ecklund¹⁰, P.J. Fernández Manteca¹⁰, S. Freed, P. Gardner, F.J.M. Geurts¹⁰, A. Kumar¹⁰, W. Li¹⁰, O. Miguel Colin¹⁰, B.P. Padley¹⁰, R. Redjimi, J. Rotter¹⁰, S. Yang¹⁰, E. Yigitbasi¹⁰, Y. Zhang¹⁰

University of Rochester, Rochester, New York, U.S.A.

A. Bodek , P. de Barbaro , R. Demina , J.L. Dulemba , C. Fallon, A. Garcia-Bellido ,
O. Hindrichs , A. Khukhunaishvili , P. Parygin , E. Popova , R. Taus , G.P. Van Onsem 

The Rockefeller University, New York, New York, U.S.A.

K. Goulian 

Rutgers, The State University of New Jersey, Piscataway, New Jersey, U.S.A.

B. Chiarito, J.P. Chou , Y. Gershtein , E. Halkiadakis , A. Hart , M. Heindl ,
D. Jaroslawski , O. Karacheban ²⁴, I. Laflotte , A. Lath , R. Montalvo, K. Nash,
M. Osherson , H. Routray , S. Salur , S. Schnetzer, S. Somalwar , R. Stone ,
S.A. Thayil , S. Thomas, J. Vora , H. Wang 

University of Tennessee, Knoxville, Tennessee, U.S.A.

H. Acharya, A.G. Delannoy , S. Fiorendi , T. Holmes , N. Karunarathna , L. Lee ,
E. Nibigira , S. Spanier 

Texas A&M University, College Station, Texas, U.S.A.

M. Ahmad , O. Bouhali ⁹¹, M. Dalchenko , A. Delgado , R. Eusebi , J. Gilmore ,
T. Huang , T. Kamon ⁹², H. Kim , S. Luo , S. Malhotra, R. Mueller , D. Overton ,
D. Rathjens , A. Safonov 

Texas Tech University, Lubbock, Texas, U.S.A.

N. Akchurin , J. Damgov , V. Hegde , A. Hussain , Y. Kazhykarim, K. Lamichhane ,
S.W. Lee , A. Mankel , T. Mengke, S. Muthumuni , T. Peltola , I. Volobouev ,
A. Whitbeck 

Vanderbilt University, Nashville, Tennessee, U.S.A.

E. Appelt , S. Greene, A. Gurrola , W. Johns , R. Kunnavalkam Elayavalli , A. Melo ,
F. Romeo , P. Sheldon , S. Tuo , J. Velkovska , J. Viinikainen 

University of Virginia, Charlottesville, Virginia, U.S.A.

B. Cardwell , B. Cox , J. Hakala , R. Hirosky , A. Ledovskoy , A. Li , C. Neu ,
C.E. Perez Lara 

Wayne State University, Detroit, Michigan, U.S.A.

P.E. Karchin 

University of Wisconsin — Madison, Madison, Wisconsin, U.S.A.

A. Aravind, S. Banerjee , K. Black , T. Bose , S. Dasu , I. De Bruyn , P. Everaerts ,
C. Galloni, H. He , M. Herndon , A. Herve , C.K. Koraka , A. Lanaro, R. Loveless ,
J. Madhusudanan Sreekala , A. Mallampalli , A. Mohammadi , S. Mondal, G. Parida ,
D. Pinna, A. Savin, V. Shang , V. Sharma , W.H. Smith , D. Teague, H.F. Tsoi ,
W. Vetens , A. Warden 

Authors affiliated with an institute or an international laboratory covered by a cooperation agreement with CERN

S. Afanasiev^{ID}, V. Andreev^{ID}, Yu. Andreev^{ID}, T. Aushev^{ID}, M. Azarkin^{ID}, A. Babaev^{ID}, A. Belyaev^{ID}, V. Blinov⁹³, E. Boos^{ID}, V. Borshch^{ID}, D. Budkouski^{ID}, V. Bunichev^{ID}, V. Chekhovsky, R. Chistov^{ID}⁹³, M. Danilov^{ID}⁹³, A. Dermenev^{ID}, T. Dimova^{ID}⁹³, D. Druzhkin^{ID}⁹⁴, M. Dubinin^{ID}⁸⁴, L. Dudko^{ID}, G. Gavrilov^{ID}, V. Gavrilov^{ID}, S. Gnenenko^{ID}, V. Golovtcov^{ID}, N. Golubev^{ID}, I. Golutvin^{ID}, I. Gorbunov^{ID}, A. Gribushin^{ID}, Y. Ivanov^{ID}, V. Kachanov^{ID}, L. Kardapoltsev^{ID}⁹³, V. Karjavine^{ID}, A. Karneyeu^{ID}, V. Kim^{ID}⁹³, M. Kirakosyan, D. Kirpichnikov^{ID}, M. Kirsanov^{ID}, V. Klyukhin^{ID}, O. Kodolova^{ID}⁹⁵, D. Konstantinov^{ID}, V. Korenkov^{ID}, A. Kozyrev^{ID}⁹³, N. Krasnikov^{ID}, A. Lanev^{ID}, P. Levchenko^{ID}⁹⁶, N. Lychkovskaya^{ID}, V. Makarenko^{ID}, A. Malakhov^{ID}, V. Matveev^{ID}^{93,97}, V. Murzin^{ID}, A. Nikitenko^{ID}^{98,95}, S. Obraztsov^{ID}, V. Oreshkin^{ID}, A. Oskin, V. Palichik^{ID}, V. Perelygin^{ID}, M. Perfilov, S. Petrushanko^{ID}, S. Polikarpov^{ID}⁹³, V. Popov, O. Radchenko^{ID}⁹³, M. Savina^{ID}, V. Savrin^{ID}, D. Selivanova^{ID}, V. Shalaev^{ID}, S. Shmatov^{ID}, S. Shulha^{ID}, Y. Skovpen^{ID}⁹³, S. Slabospitskii^{ID}, V. Smirnov^{ID}, D. Sosnov^{ID}, V. Sulimov^{ID}, E. Tcherniaev^{ID}, A. Terkulov^{ID}, O. Teryaev^{ID}, I. Tlisova^{ID}, A. Toropin^{ID}, L. Uvarov^{ID}, A. Uzunian^{ID}, A. Vorobyev[†], N. Voytishin^{ID}, B.S. Yuldashev⁹⁹, A. Zarubin^{ID}, I. Zhizhin^{ID}, A. Zhokin^{ID}

[†] Deceased

¹ Also at Yerevan State University, Yerevan, Armenia

² Also at TU Wien, Vienna, Austria

³ Also at Institute of Basic and Applied Sciences, Faculty of Engineering, Arab Academy for Science, Technology and Maritime Transport, Alexandria, Egypt

⁴ Also at Université Libre de Bruxelles, Bruxelles, Belgium

⁵ Also at Universidade Estadual de Campinas, Campinas, Brazil

⁶ Also at Federal University of Rio Grande do Sul, Porto Alegre, Brazil

⁷ Also at UFMS, Nova Andradina, Brazil

⁸ Also at Nanjing Normal University Department of Physics, Nanjing, China

⁹ Now at The University of Iowa, Iowa City, Iowa, U.S.A.

¹⁰ Also at University of Chinese Academy of Sciences, Beijing, China

¹¹ Also at University of Chinese Academy of Sciences, Beijing, China

¹² Also at an institute or an international laboratory covered by a cooperation agreement with CERN

¹³ Also at Suez University, Suez, Egypt

¹⁴ Now at British University in Egypt, Cairo, Egypt

¹⁵ Also at Purdue University, West Lafayette, Indiana, U.S.A.

¹⁶ Also at Université de Haute Alsace, Mulhouse, France

¹⁷ Also at Department of Physics, Tsinghua University, Beijing, China

¹⁸ Also at The University of the State of Amazonas, Manaus, Brazil

¹⁹ Also at Erzincan Binali Yildirim University, Erzincan, Turkey

²⁰ Also at University of Hamburg, Hamburg, Germany

²¹ Also at RWTH Aachen University, III. Physikalisches Institut A, Aachen, Germany

²² Also at Isfahan University of Technology, Isfahan, Iran

²³ Also at Bergische University Wuppertal (BUW), Wuppertal, Germany

²⁴ Also at Brandenburg University of Technology, Cottbus, Germany

²⁵ Also at Forschungszentrum Jülich, Juelich, Germany

²⁶ Also at CERN, European Organization for Nuclear Research, Geneva, Switzerland

²⁷ Also at Physics Department, Faculty of Science, Assiut University, Assiut, Egypt

²⁸ Also at Wigner Research Centre for Physics, Budapest, Hungary

²⁹ Also at Institute of Physics, University of Debrecen, Debrecen, Hungary

- ³⁰ Also at Institute of Nuclear Research ATOMKI, Debrecen, Hungary
³¹ Now at Universitatea Babes-Bolyai — Facultatea de Fizica, Cluj-Napoca, Romania
³² Also at Faculty of Informatics, University of Debrecen, Debrecen, Hungary
³³ Also at Punjab Agricultural University, Ludhiana, India
³⁴ Also at UPES — University of Petroleum and Energy Studies, Dehradun, India
³⁵ Also at University of Visva-Bharati, Santiniketan, India
³⁶ Also at University of Hyderabad, Hyderabad, India
³⁷ Also at Indian Institute of Science (IISc), Bangalore, India
³⁸ Also at IIT Bhubaneswar, Bhubaneswar, India
³⁹ Also at Institute of Physics, Bhubaneswar, India
⁴⁰ Also at Deutsches Elektronen-Synchrotron, Hamburg, Germany
⁴¹ Now at Department of Physics, Isfahan University of Technology, Isfahan, Iran
⁴² Also at Sharif University of Technology, Tehran, Iran
⁴³ Also at Department of Physics, University of Science and Technology of Mazandaran, Behshahr, Iran
⁴⁴ Also at Helwan University, Cairo, Egypt
⁴⁵ Also at Italian National Agency for New Technologies, Energy and Sustainable Economic Development, Bologna, Italy
⁴⁶ Also at Centro Siciliano di Fisica Nucleare e di Struttura Della Materia, Catania, Italy
⁴⁷ Also at Università degli Studi Guglielmo Marconi, Roma, Italy
⁴⁸ Also at Scuola Superiore Meridionale, Università di Napoli ‘Federico II’, Napoli, Italy
⁴⁹ Also at Fermi National Accelerator Laboratory, Batavia, Illinois, U.S.A.
⁵⁰ Also at Università di Napoli ‘Federico II’, Napoli, Italy
⁵¹ Also at Ain Shams University, Cairo, Egypt
⁵² Also at Consiglio Nazionale delle Ricerche — Istituto Officina dei Materiali, Perugia, Italy
⁵³ Also at IRFU, CEA, Université Paris-Saclay, Gif-sur-Yvette, France
⁵⁴ Also at Riga Technical University, Riga, Latvia
⁵⁵ Also at Department of Applied Physics, Faculty of Science and Technology, Universiti Kebangsaan Malaysia, Bangi, Malaysia
⁵⁶ Also at Consejo Nacional de Ciencia y Tecnología, Mexico City, Mexico
⁵⁷ Also at Trincomalee Campus, Eastern University, Sri Lanka, Nilaveli, Sri Lanka
⁵⁸ Also at INFN Sezione di Pavia, Università di Pavia, Pavia, Italy
⁵⁹ Also at National and Kapodistrian University of Athens, Athens, Greece
⁶⁰ Also at Ecole Polytechnique Fédérale Lausanne, Lausanne, Switzerland
⁶¹ Also at Universität Zürich, Zurich, Switzerland
⁶² Also at Stefan Meyer Institute for Subatomic Physics, Vienna, Austria
⁶³ Also at Laboratoire d’Annecy-le-Vieux de Physique des Particules, IN2P3-CNRS, Annecy-le-Vieux, France
⁶⁴ Also at Near East University, Research Center of Experimental Health Science, Mersin, Turkey
⁶⁵ Also at Konya Technical University, Konya, Turkey
⁶⁶ Also at Izmir Bakircay University, Izmir, Turkey
⁶⁷ Also at Adiyaman University, Adiyaman, Turkey
⁶⁸ Also at Necmettin Erbakan University, Konya, Turkey
⁶⁹ Also at Bozok Universitetesi Rektörlüğü, Yozgat, Turkey
⁷⁰ Also at Marmara University, Istanbul, Turkey
⁷¹ Also at Milli Savunma University, Istanbul, Turkey
⁷² Also at Kafkas University, Kars, Turkey
⁷³ Also at Hacettepe University, Ankara, Turkey
⁷⁴ Also at Istanbul University — Cerrahpasa, Faculty of Engineering, Istanbul, Turkey
⁷⁵ Also at Ozyegin University, Istanbul, Turkey
⁷⁶ Also at Vrije Universiteit Brussel, Brussel, Belgium
⁷⁷ Also at School of Physics and Astronomy, University of Southampton, Southampton, United Kingdom
⁷⁸ Also at University of Bristol, Bristol, United Kingdom

- ⁷⁹ Also at IPPP Durham University, Durham, United Kingdom
⁸⁰ Also at Monash University, Faculty of Science, Clayton, Australia
⁸¹ Also at Università di Torino, Torino, Italy
⁸² Also at Bethel University, St. Paul, Minnesota, U.S.A.
⁸³ Also at Karamanoğlu Mehmetbey University, Karaman, Turkey
⁸⁴ Also at California Institute of Technology, Pasadena, California, U.S.A.
⁸⁵ Also at United States Naval Academy, Annapolis, Maryland, U.S.A.
⁸⁶ Also at Bingöl University, Bingöl, Turkey
⁸⁷ Also at Georgian Technical University, Tbilisi, Georgia
⁸⁸ Also at Sinop University, Sinop, Turkey
⁸⁹ Also at Erciyes University, Kayseri, Turkey
⁹⁰ Also at Horia Hulubei National Institute of Physics and Nuclear Engineering (IFIN-HH), Bucharest, Romania
⁹¹ Also at Texas A&M University at Qatar, Doha, Qatar
⁹² Also at Kyungpook National University, Daegu, Korea
⁹³ Also at another institute or international laboratory covered by a cooperation agreement with CERN
⁹⁴ Also at Universiteit Antwerpen, Antwerpen, Belgium
⁹⁵ Also at Yerevan Physics Institute, Yerevan, Armenia
⁹⁶ Also at Northeastern University, Boston, Massachusetts, U.S.A.
⁹⁷ Now at another institute or international laboratory covered by a cooperation agreement with CERN
⁹⁸ Also at Imperial College, London, United Kingdom
⁹⁹ Also at Institute of Nuclear Physics of the Uzbekistan Academy of Sciences, Tashkent, Uzbekistan